

TOWARD UNDERSTANDING PREDICTABILITY OF CLIMATE:  
A LINEAR STOCHASTIC MODELING APPROACH

A Dissertation

by

FAMING WANG

Submitted to the Office of Graduate Studies of  
Texas A&M University  
in partial fulfillment of the requirements for the degree of

DOCTOR OF PHILOSOPHY

August 2003

Major Subject: Oceanography

TOWARD UNDERSTANDING PREDICTABILITY OF CLIMATE:  
A LINEAR STOCHASTIC MODELING APPROACH

A Dissertation

by

FAMING WANG

Submitted to Texas A&M University  
in partial fulfillment of the requirements  
for the degree of

DOCTOR OF PHILOSOPHY

Approved as to style and content by:

---

Ping Chang  
(Chair of Committee)

---

Robert O. Reid  
(Member)

---

Achim Stössel  
(Member)

---

Richard L. Panetta  
(Member)

---

Wilford D. Gardner  
(Head of Department)

August 2003

Major Subject: Oceanography

## ABSTRACT

Toward Understanding Predictability of Climate:  
A Linear Stochastic Modeling Approach. (August 2003)  
Faming Wang, B.S., Shandong University;  
M.S., First Institute of Oceanography  
Chair of Advisory Committee: Dr. Ping Chang

This dissertation discusses the predictability of the atmosphere-ocean climate system on interannual and decadal timescales. We investigate the extent to which the atmospheric internal variability (weather noise) can cause climate prediction to lose skill; and we also look for the oceanic processes that contribute to the climate predictability via interaction with the atmosphere.

First, we develop a framework for assessing the predictability of a linear stochastic system. Based on the information of deterministic dynamics and noise forcing, various predictability measures are defined and new predictability-analysis tools are introduced. For the sake of computational efficiency, we also discuss the formulation of a low-order model within the context of four reduction methods: modal, EOF, most predictable pattern, and balanced truncation.

Subsequently, predictabilities of two specific physical systems are investigated within such a framework.

The first is a mixed layer model of SST with focus on the effect of oceanic advection. Analytical solution of a one-dimensional model shows that even though advection can give rise to a pair of low-frequency normal modes, no enhancement in the predictability is found in terms of domain averaged error variance. However,

a Predictable Component Analysis (PrCA) shows that advection can play a role in redistributing the predictable variance. This analytical result is further tested in a more realistic two-dimensional North Atlantic model with observed mean currents.

The second is a linear coupled model of tropical Atlantic atmosphere-ocean system. Eigen-analysis reveals that the system has two types of coupled modes: a decadal meridional mode and an interannual equatorial mode. The meridional mode, which manifests itself as a dipole pattern in SST, is controlled by thermodynamic feedback between wind, latent heat flux, and SST, and modified by ocean heat transport. The equatorial mode, which manifests itself as an SST anomaly in the eastern equatorial basin, is dominated by dynamic feedback between wind, thermocline, upwelling, and SST. The relative strength of thermodynamic vs dynamic feedbacks determines the behavior of the coupled system, and enables the tropical Atlantic variability to be more predictable than the passive-ocean scenario.

To My Grandma

## ACKNOWLEDGMENTS

First, I'm grateful to my advisor, Dr. Ping Chang, for his assistance and guidance in the work presented here, for his support and patience with me. Without his enthusiasm and curiosity about science, this dissertation would never come into shape. Since Chapter III is duplicated from one of our papers being submitted, some of the text was written by him.

Second, I would like to thank other members of my committee, Dr. Robert Reid, Dr. Achim Stössel, and Dr. Lee Panetta for their insightful questions, useful suggestions, and productive discussions during the course of this work. Their numerous comments and careful corrections improve the readability and succinctness of this dissertation. Thanks also go to my friends and fellow students for the wonderful time we spent together.

I also wish to express my gratitude to Lisa M. Graves, who carefully read the manuscript several times and edited almost every page of it, especially when none of these is her duty.

Last and foremost, my parents and sisters play the most important role in my journey of pursuing a PhD degree, though of course in a much broader sense. Their unfailing encouragements and absolute support keep me going through difficulties and seeing light in the dark tunnel. Love you guys.

## TABLE OF CONTENTS

CHAPTER		Page
I	INTRODUCTION . . . . .	1
II	A FRAMEWORK OF LINEAR STOCHASTIC MODEL ANALYSIS . . . . .	4
	A. Linear stochastic model . . . . .	5
	1. Properties of LTI system . . . . .	7
	2. EOF, singular vector, and stochastic optimal . . . . .	12
	a. EOF . . . . .	12
	b. Singular vector . . . . .	13
	c. Stochastic optimal . . . . .	14
	d. Effect of nonnormality . . . . .	14
	B. Predictability of LTI system . . . . .	15
	1. Predictability measures . . . . .	17
	a. Normalized error variance . . . . .	17
	b. Measures from information theory . . . . .	18
	c. Predictability of normal system under unitary forcing . . . . .	20
	2. Most predictable pattern and optimal forcing . . . . .	21
	a. Most predictable pattern . . . . .	21
	b. Optimal forcing with respect to predictability . . . . .	23
	3. Summary . . . . .	23
	C. A low-dimensional approximation . . . . .	24
	1. Objective . . . . .	27
	2. Approximation methods . . . . .	29
	a. Normal mode . . . . .	29
	b. EOF . . . . .	30
	c. Balanced truncation . . . . .	30
	d. Most predictable pattern . . . . .	32
	3. EOFs are normal modes . . . . .	33
	4. EOFs aren't normal modes . . . . .	36
	5. Some thoughts . . . . .	40
	D. Numerical recipes . . . . .	42

CHAPTER	Page	
III	EFFECT OF OCEANIC ADVECTION ON THE PREDICTABILITY OF MIDLATITUDE SST . . . . .	46
	A. Introduction . . . . .	46
	B. A stochastically forced ocean mixed layer model . . . . .	48
	C. Analytical solution to 1D advective model . . . . .	51
	1. Solving the 1D model . . . . .	53
	2. Variance analysis . . . . .	55
	3. Predictability analysis . . . . .	57
	4. An example with realistic parameters . . . . .	61
	5. A general white noise forcing . . . . .	63
	D. Predictability of North Atlantic SST . . . . .	65
	1. Parameter estimation . . . . .	65
	2. Normal modes and EOFs of SST . . . . .	68
	3. Predictability and predictable component . . . . .	71
	E. Summary . . . . .	73
IV	TROPICAL ATLANTIC VARIABILITY AND ITS PREDICTABILITY . . . . .	75
	A. Introduction . . . . .	75
	B. Model description . . . . .	79
	1. Nonlinear intermediate coupled model . . . . .	80
	2. Linear stochastic model of ICM . . . . .	83
	a. Statistical atmosphere . . . . .	84
	b. Numerics . . . . .	89
	C. Physical modes in the tropical Atlantic atmosphere-ocean system . . . . .	90
	1. Free modes . . . . .	90
	2. Coupled modes . . . . .	92
	a. Pure thermodynamical coupled mode . . . . .	93
	b. Pure dynamical coupled mode . . . . .	97
	3. Mixed modes . . . . .	101
	D. Comments on the debate of Atlantic dipole mode . . . . .	106
	E. An exploration of coupling parameter space . . . . .	111
	F. Predictability . . . . .	113
	1. Global measure . . . . .	113
	2. Local measure . . . . .	115
	G. Summary . . . . .	118



CHAPTER	Page
V CONCLUSION AND FUTURE PROJECTS . . . . .	123
A. What's been done . . . . .	123
B. What's ahead . . . . .	125
REFERENCES . . . . .	129
APPENDIX A . . . . .	144
APPENDIX B . . . . .	149
VITA . . . . .	150

## LIST OF TABLES

TABLE		Page
I	Description of mathematical notations and symbols . . . . .	8
II	Common optimals $\mathbf{v}$ of linear stochastic system: $d\mathbf{x}/dt = \mathbf{A}\mathbf{x} + \boldsymbol{\eta}$ . .	25

## LIST OF FIGURES

FIGURE	Page
1	Performance of different model reductions in Example 1 . . . . . 35
2	Reduced order model of tropical Atlantic variability (m=1) . . . . . 39
3	Reduced order model of tropical Atlantic variability (m=4) . . . . . 40
4	Flowchart of linear stochastic modeling . . . . . 45
5	Schematic sketch of oceanic gyre and atmospheric forcing . . . . . 52
6	Schematic drawing of SST EOFs in the 1D system . . . . . 57
7	Most and least predictable patterns of the simple 1D model . . . . . 59
8	Power spectrum of the 1D climate system with realistic parameters . . . . . 62
9	Predictability of 1D advective ocean . . . . . 62
10	Estimated damping rate of SST in North Atlantic . . . . . 67
11	First EOF of the estimated atmosphere white noise forcing . . . . . 68
12	The normal mode of advective ocean . . . . . 69
13	Predictability of North Atlantic Ocean SST . . . . . 72
14	Most predictable pattern at 5 month lead time . . . . . 73
15	Elements of tropical Atlantic variability . . . . . 76
16	Whiteness test of stochastic forcing in tropical Atlantic . . . . . 88
17	Basin mode of equatorial Atlantic Ocean at different phases . . . . . 92
18	Meridional mode for $\mu = 0, \nu = 1$ . . . . . 94
19	Eigenvalue of the meridional mode for $\mu = 0$ . . . . . 95

FIGURE	Page
20	A weak coupled SST mode for $\mu = 0, \nu = 0.3$ . . . . . 95
21	Thermodynamical mode given by SVD analysis of COADS data . . . 97
22	Equatorial mode in tropical Atlantic for $\mu = 1, \nu = 0$ . . . . . 99
23	Eigenvalue of the equatorial mode for $\nu = 0$ . . . . . 100
24	Mixed meridional mode for $\mu = 1, \nu = 1$ . . . . . 102
25	Mixed equatorial mode for $\mu = 1, \nu = 1$ . . . . . 104
26	Eigenvalue of mixed mode for $\mu = 1$ . . . . . 105
27	Eigenvalue of mixed mode for $\nu = 1$ . . . . . 106
28	EOFs and correlation of simulated tropical Atlantic variability . . . . 107
29	Thermodynamical coupled mode in CCM3 run with slab ocean . . . . 108
30	Cartoon of thermodynamical feedback in tropics . . . . . 110
31	Eigenvalue of first normal mode as a function of coupling strength . . 111
32	Predictability of tropical Atlantic SST as a function of $\mu$ and $\nu$ . . . 113
33	Skill of most predictable pattern as a function of coupling strength . . 116
34	Most predictable pattern for standard coupling . . . . . 119
35	Most predictable pattern for strong wind stress coupling . . . . . 120
36	Normalized error variance of different prediction schemes . . . . . 148

## CHAPTER I

## INTRODUCTION

Several climate phenomena have long been identified as important influences on the social and economic well-being of our societies on seasonal-to-interannual time scales: El Niño/Southern Oscillation (ENSO) is the strongest, even remote areas can feel its impact through teleconnection (Diaz et al., 2001); the rainfall patterns over sub-Saharan Africa and northeast Brazil are closely related to the tropical Atlantic variability (TAV), while the European winters are strongly affected by the phase of North Atlantic Oscillation (NAO) (Marshall et al., 2001b); and global Monsoon system determines the dry and wet seasons over many regions. One underlying feature of all these climate modes is the irregularity in their evolution which in turn limits their predictability.

Generally, the source of irregularity of climate system can be classified into two categories (Chang et al., 1996; Neelin et al., 1998; Goddard et al., 2001; Dijkstra and Burgers, 2002):

1. *Extrinsic Irregularity* – the “slowly” varying climate signals are disturbed by internal variability of the atmosphere and the ocean which themselves lack order on the climate scale (Frankignoul and Hasselmann, 1977; Penland and Sardeshmukh, 1995; Moore and Kleeman, 1999; Thompson and Battisti, 2000, 2001);
2. *Intrinsic Irregularity* – the coupling between various components of the climate system is highly nonlinear just like weather, its chaotic nature gives rise to the irregularity (Zebiak and Cane, 1987; Jin et al., 1994; Tziperman et al., 1994, 1995).

---

This dissertation follows the style and format of *Journal of Climate*.

In order to explore the limit of climate prediction, a thorough understanding of the origin of irregularity and its effect on predictability is critically needed and has both practical and theoretical significance.

In a series of papers, Lorenz (1963, 1965, 1984) examined the predictability of the atmosphere on the synoptic scale and showed that a weather forecast is limited to a two week period. As we now know, this is typical behavior of a chaotic system—small initial error renders the subsequent evolution unpredictable over time even though the governing equation is deterministic. Such sensitivity to initial condition is vividly called the “Butterfly Effect”, i.e. a butterfly flipping its wings in Brazil will cause a tornado in College Station, Texas (Lorenz, 1993). Since weather and climate are just two paradigms of one system (atmosphere-ocean), both contribute what we experience, observe, and measure. On the other hand, weather and climate have different time and space scales.<sup>1</sup> Therefore one can simulate one component with the other component providing the external forcing or boundary condition. If the interannual and decadal variability is of interest, then weather events can be represented by white noise forcing with randomness and unpredictability in common. This is the basic idea of Hasselmann’s (1976) stochastic climate model in which the natural climate variability is generated by weather forcing due to the integrating effect of the ocean. In such a system, predictability is defined by two competitors, order from the slowly responding atmosphere-ocean and disorder from rapidly varying weather.

The work presented here is inspired by the Hasselmann’s spirit, hence it belongs

---

<sup>1</sup>This is where difficulty lies and controversy begins. Although it seems like everyone knows what is weather and what is climate, no single definition fits all purpose. The core of stochastic climate model is the observation that the timescales of weather and climate are well separated, which remains an unsettled issue in theory (Imkeller and von Storch, 2001).

to category 1. And it is further assumed that the coupled dynamics may be approximated as linear processes. Since eventually the ocean affects the atmosphere through sea surface temperature (SST), predictability of SST is used as an index for the predictability of climate. With all these assumptions, we propose here to use a linear stochastic model to attack the fundamental questions: What are the roles of ocean in defining the climate variability? How does weather “noise” affect the predictability of climate? And what is the major source of predictable dynamics, passive ocean-integrator or positive air-sea feedback? Particularly, two case studies will be addressed in this dissertation. The first one is the effect of ocean advection on midlatitude sea surface temperature (Chapter III). The other is dealing with tropical Atlantic variability (Chapter IV). Before pursuing these two studies, a framework of linear stochastic modeling is first developed (Chapter II).

## CHAPTER II

## A FRAMEWORK OF LINEAR STOCHASTIC MODEL ANALYSIS

We usually regard classic physics as deterministic in a sense that given the past, the future evolution can be predicted with arbitrary precision according to the physical laws, or at least we were taught so. However, the probabilistic view of natural phenomena appeared long before the discovery of quantum mechanics. A classic example of stochastic process in physics is Brownian motion—random motion of pollen particles in water. Even the great Albert Einstein studied this phenomenon at the beginning of 20th century, although it was Paul Langevin who directly derived the formula about Brownian motion from Newton’s second law. Since then, stochastic models have been popularized in many fields, from physics, chemistry, biology to engineering, and even finance. In fact, the 1997 Nobel Prize in Economics was awarded to Robert C. Mertrou and Mayron S. Scholes for their stochastic model of the price of an asset. Although the causes of uncertainty or randomness in these disciplines are different, the underlying mathematics is the same—the stochastic differential equation. An excellent introductory textbook on this subject is the one written by Øksendal (2000). In this dissertation, I prefer the word “stochastic model” to emphasize the physics embodied in it.

For the climate system, as mentioned in Chapter I, the day-to-day weather changes can be viewed as external driving force which is essentially random in time and white in spectrum. The climate variability is an integral response to the white noise forcing. In 1976, Klaus Hasselmann proposed this idea to explain the observed red spectrum of natural climate variability. His pioneer work has far-reaching importance in climate studies. Even in light of today’s high resolution coupled general circulation model (CGCM) and much improved observation network, the stochas-



tic model regains its virtue as a simple conceptual model (Imkeller and von Storch, 2001). The abundance of raw data does not automatically transfer into an abundance of knowledge. Understanding comes from a comprehensive analysis of a dynamic system through simplification, and that is where the stochastic climate model fits in. The next two chapters will illuminate some aspects of this spirit.

The framework of linear stochastic model is introduced in this chapter. Following a brief overview of the stochastic model, its characteristics are explored in Section A. From the very beginning, we will see the interlacing relationship of deterministic dynamics and noise forcing in determining the system behavior. With that said, the predictability measures of the linear stochastic model are defined, and the detailed procedure of predictability analysis is given in Section B. The climate system usually has high dimensions (millions of grid points for a GCM), it is not practical to deal with such large dimension matrices . A low-order model can be constructed and analyzed as an approximation of the total system. Thus, different model reduction methods and their effects on predictability estimate are discussed in Section C. For the sake of completeness, a brief introduction to linear inverse modeling (LIM) is given in Section D.

## A. Linear stochastic model

In principle, the evolution of a general dynamic system can be described by a set of prognostic equations

$$\frac{d\mathbf{x}}{dt} = \mathcal{L}\mathbf{x} + \mathbf{f}, \quad (2.1)$$

where  $\mathbf{x}$  is the state variable,  $\mathcal{L}$  denotes a nonlinear operator, and  $\mathbf{f}$  represents the external forcing. For the climate system,  $\mathbf{x}$  could be air temperature, sea surface temperature, precipitation, wind stress, or their combination; operator  $\mathcal{L}$  represents

the dynamical, thermodynamical, and chemical laws which govern the motions and interactions within and between atmosphere and ocean;  $\mathbf{f}$  is the extraterrestrial influence (e.g. solar radiation, tidal forcing). Given the forcing  $\mathbf{f}$ , system (2.1) usually contains one or more equilibrium states  $\mathbf{x}_{\text{mean}}$  about which the system may hover for a long time. Then linearization of (2.1) for this steady background state can be nominally written as a governing equation for anomaly  $\mathbf{x}_a = \mathbf{x} - \mathbf{x}_{\text{mean}}$ :

$$\frac{d\mathbf{x}_a}{dt} = \mathbf{A}\mathbf{x}_a + \boldsymbol{\eta}, \quad (2.2)$$

where operator  $\mathbf{A}$  is the linearized  $\mathcal{L}$  with respect to  $\mathbf{x}_{\text{mean}}$ ; and the forcing term  $\boldsymbol{\eta}$  models the nonlinear effect. We have assumed that the only effect of external forcing is in defining the mean state, and it does not enter into anomaly equation (2.2). Many characteristics of the complex nonlinear system can often be inferred from analyzing the linear model, although its validity is limited as the degree of nonlinearity increases. For example, we can not use linear model to study turbulence. For the weak nonlinear climate system, (2.2) may be used to capture the large scale variability. The subscript is dropped from  $\mathbf{x}_a$  in the following discussion for the sake of simplicity.

The nonlinear term  $\boldsymbol{\eta}$  usually represents the source of irregularity and chaos within the dynamical system. As a first-order approximation,  $\boldsymbol{\eta}$  might be treated as random noise. Furthermore, if it lacks persistence, i.e. its autocorrelation drops sharply as time lapses, then white noise would be an acceptable approximation. Day-to-day weather perturbations are such example when seen from a climate timescale. White noise is totally unpredictable, and its autocorrelation is a Dirac-delta function. Although linear operator  $\mathbf{A}$  is deterministic in nature,  $\mathbf{x}$  describes a stochastic processes because of the inherent uncertainty in  $\boldsymbol{\eta}$ . Eq. (2.2) becomes a linear stochastic differential equation

$$\frac{d\mathbf{x}}{dt} = \mathbf{A}(t)\mathbf{x} + \boldsymbol{\eta}. \quad (2.3)$$

Usually, a normal distribution is assumed,  $\boldsymbol{\eta} \sim \mathcal{N}(0, \boldsymbol{\Sigma})$  and  $\mathbf{x} \sim \mathcal{N}(0, \mathbf{C})$ .

One immediate and profound consequence of the change from (2.2) to (2.3) is that we no longer know the precise state of the system at any given time. A probabilistic view has to be taken, i.e. any state (one point in state space) is assigned a probability density. High probable states mean that the system will stay there longer or visit them more frequently. Single perfect prediction scenarios must be abandoned and replaced by ensemble prediction with a statistical measure to gauge its skill.

In this dissertation, the investigation is restricted to a special but useful case—an  $n$ -dimensional, linear, time-invariant system (or autonomous system), i.e. operator  $\mathbf{A}_{n \times n}$  is a constant. It is simple enough to be solved analytically

$$\mathbf{x}(t_0 + \tau) = e^{\mathbf{A}\tau} \mathbf{x}(t_0) + \int_0^\tau e^{\mathbf{A}(\tau-s)} \boldsymbol{\eta}(s + t_0) ds; \quad (2.4)$$

yet it is realistic enough to capture the essential dynamics and find practical applications in many fields. The Markov model in statistics, the Langevin equation in physics, and the Ornstein-Uhlenbeck process in mathematics, all belong to this category. Before exploring the properties of the linear time invariant (LTI) system, some mathematical expressions and common usages are defined in Table I.

### 1. Properties of LTI system

If the real system starts from a static state  $\mathbf{x}|_{t_0=0} = 0$ , its total energy could be written as

$$\text{var}(\mathbf{x}(t)) = \langle \mathbf{x}^T \mathbf{x} \rangle = \text{tr}(\boldsymbol{\Sigma} \mathbf{B}_t), \quad (2.5)$$

where  $\mathbf{B}_t = \int_0^t e^{\mathbf{A}^T s} e^{\mathbf{A}s} ds$  is called stochastic operator (Farrell and Ioannou, 1996a). Next, we try to find the lower and upper bounds for the total variance because they measure the stability of (2.3) in the Lyapunov's sense.

Table I. Description of mathematical notations and symbols

notation	description
$a$	scalar
$a^*$	complex conjugate of $a$
$ a $	absolute value or modulus of $a$
$\mathbf{x}$	state vector
$\mathbf{R}^n$	$n$ -dimensional Euclidean space
$\mathbf{A}$	linear operator in matrix form
$\mathbf{A}^T$	transpose of $\mathbf{A}$
$\mathbf{A}^\dagger$	complex conjugate transpose of $\mathbf{A}$
$\mathbf{A}^{-1}$	inverse of $\mathbf{A}$
$\mathbf{A}^{-\dagger}$	$(\mathbf{A}^{-1})^\dagger$
$\text{tr}(\mathbf{A})$	trace of a matrix $\mathbf{A}$
$\det(\mathbf{A})$	determinant of $\mathbf{A}$
$\ \mathbf{A}\ $	norm of matrix $\mathbf{A}$
$\lambda(\mathbf{A})$	eigenvalues of $\mathbf{A}$ in descending order s.t. $\Re(\lambda_i) > \Re(\lambda_j)$ , if $i < j$
$\sigma(\mathbf{A})$	singular values of $\mathbf{A}$ in descending order s.t. $\sigma_i > \sigma_j$ , if $i < j$
$\langle \mathbf{x} \rangle$	expectation of random variable $\mathbf{x}$
$\langle \mathbf{y}   \mathbf{x} \rangle$	conditional expectation of $\mathbf{y}$ w.r.t. $\mathbf{x}$
$\bar{\mathbf{x}}$	conditional mean $\langle \mathbf{x}(t_0 + \tau)   \mathbf{x}(t_0) \rangle$ , or mean $\langle \mathbf{x} \rangle$
$\mathbf{x}'$	perturbation $\mathbf{x}' = \mathbf{x} - \bar{\mathbf{x}}$
$\text{var}(\mathbf{x})$	variance of $\mathbf{x}$ , $\langle (\mathbf{x}')^T (\mathbf{x}') \rangle$

*Note:* No attempt has been made to distinguish a random variable and its realization.

First, the inequality of trace product (Marcus and Minc, 1992) gives

$$\lambda_n(\Sigma)\text{tr}(\mathbf{B}_t) \leq \text{tr}(\Sigma\mathbf{B}_t) \leq \lambda_1(\Sigma)\text{tr}(\mathbf{B}_t). \quad (2.6)$$

As to  $\text{tr}(\mathbf{B}_t)$ , Ioannou (1995) proved that variance is lower bounded,

$$\begin{aligned} \text{tr}(\mathbf{B}_t) &= \int_0^t \text{tr}(e^{\mathbf{A}^T s} e^{\mathbf{A} s}) ds \\ &\geq \sum_{i=1}^n \int_0^t e^{(\lambda_i(\mathbf{A}) + \lambda_i^*(\mathbf{A}))s} ds \\ &= \sum_{i=1}^n \frac{e^{(\lambda_i(\mathbf{A}) + \lambda_i^*(\mathbf{A}))t} - 1}{\lambda_i(\mathbf{A}) + \lambda_i^*(\mathbf{A})} \end{aligned} \quad (2.7)$$

which is equivalent to a lower bound. A weak upper bound can also be found based on the simple observation

$$\begin{aligned} \text{tr}(\mathbf{B}_t) &= \int_0^t \sum_{i,j} c_{ij} e^{(\lambda_i(\mathbf{A}) + \lambda_j^*(\mathbf{A}))s} ds \\ &\leq n^2 \max(|c_{ij}|) \int_0^t e^{(\lambda_1(\mathbf{A}) + \lambda_1^*(\mathbf{A}))s} ds, \\ &= n^2 \max(|c_{ij}|) \frac{e^{(\lambda_1(\mathbf{A}) + \lambda_1^*(\mathbf{A}))t} - 1}{\lambda_1(\mathbf{A}) + \lambda_1^*(\mathbf{A})} \end{aligned} \quad (2.8)$$

where coefficients  $c_{ij}$  are complex numbers. Therefore, (2.6), (2.7), and (2.8) together show the dynamic importance of  $\mathbf{A}$ 's eigenstructure (normal modes). If the first eigenvalue has positive real part  $\Re(\lambda_1) > 0$ , the total response grows exponentially with time, which means the system is unstable; when  $\Re(\lambda_1) < 0$ , a stationary response is obtained and the system is asymptotically stable; and the third case is  $\Re(\lambda_1) = 0$ , in which a pure oscillation is observed if  $\Im(\lambda_1) \neq 0$ . From now on, we will not distinguish the stability of operator  $\mathbf{A}$ , normal modes, or the system. Further we assume  $\mathbf{A}$  is stable unless stated otherwise.

Stability analysis has become a standard procedure in examining a dynamical system. The origin and growth of small perturbations are often attributed to the

existence of unstable modes. In the limit of long times, the first normal mode (least damped mode) dominates the response. The above classical stability theory has been extended by Farrell and Ioannou (1996a,b) to explain the transient growth processes. They argued that mode-mode interaction or nonnormality could give rise to a larger growth than the one revealed by the first normal mode. Therefore, the behavior of a highly non-normal system may have little to do with its leading eigenmode. In studying non-normal operators or matrices, a more powerful tool is the pseudospectral analysis (Trefethen, 1992, 1997, 1999), which is used to explain ‘hydrodynamic stability without eigenvalues’ (Trefethen et al., 1993). For the nonlinear system, Hasselmann (1988) proposed principal interaction pattern (PIP) analysis, which is the counterpart of principal oscillation pattern (POP) or normal mode for the linear case. Recently, Neumaier and Schneider (2001) developed a procedure to estimate eigenmodes of high order autoregressive (AR) models, while (2.3) is basically an AR(1) model.

Traditionally, the least damped eigenmodes are considered to be the most important dynamical modes and responsible for the error growing or paradigm shift. This may be true for self-closed deterministic systems. In the linear stochastic system (2.3), white noise forcing is spatially coherent. It is often the case that other normal modes are excited, but not the least damped one. We’ll return to this topic in Chapter III.

The influence of stochastic forcing is better discussed in terms of the fluctuation-dissipation relation (Penland and Sardeshmukh, 1995), also known as continuous algebraic Lyapunov equation (Gajić and Qureshi, 1995). For a stable system (2.3), the covariance matrix of  $\mathbf{x}$ ,  $\mathbf{C} = \langle \mathbf{x}\mathbf{x}^T \rangle$ , satisfies the Lyapunov equation (see Farrell and Ioannou, 1996a)

$$\mathbf{A}\mathbf{C} + \mathbf{C}\mathbf{A}^T = -\mathbf{\Sigma}. \quad (2.9)$$

So does the stochastic dynamical operator  $\mathbf{B}$ ,

$$\mathbf{A}^T \mathbf{B} + \mathbf{B} \mathbf{A} = -\mathbf{I}, \quad (2.10)$$

where  $\mathbf{B}$  denotes  $\mathbf{B}_\infty$ , and  $\mathbf{I}$  is the identity matrix. Only for spatial-white (unitary) noise forcing  $\Sigma = \mathbf{I}$  and normal system  $\mathbf{A} \mathbf{A}^\dagger = \mathbf{A}^\dagger \mathbf{A}$ , does the stability analysis fully describe the system characteristics (Farrell and Ioannou, 1996a). For a nonnormal system or non-unitary forcing, the evolution of (2.3) results from competition (or combination) between least damped normal modes and the most energetic forcing modes. Tippett and Chang (2003) showed that a special arrangement of forcing may selectively excite only certain normal modes. Taking this into consideration, Neumaier and Schneider (2001) constructed an excitation parameter to measure the relative importance of normal modes to stochastic forcing. Furthermore, the predictability of the system (2.3) is also closely related to forcing patterns (see section B).

Another popular statistic technique in studying time series is the spectrum analysis. The Fourier transform of (2.3)

$$(i\omega \mathbf{I} - \mathbf{A}) \mathfrak{F}(\mathbf{x}) = \mathfrak{F}(\boldsymbol{\eta})$$

gives the cross-spectrum matrix

$$\langle \mathfrak{F}(\mathbf{x}) \mathfrak{F}(\mathbf{x})^\dagger \rangle = (i\omega \mathbf{I} - \mathbf{A})^{-1} \Sigma (i\omega \mathbf{I} - \mathbf{A})^{-\dagger}. \quad (2.11)$$

The power spectrum of a dynamical system would be a spatial average over all grid points  $S(\omega) = \langle \mathfrak{F}(\mathbf{x})^\dagger \mathfrak{F}(\mathbf{x}) \rangle$ , and has a simple interpretation for unitary  $\boldsymbol{\eta}$  and normal  $\mathbf{A}$ ,

$$S(\omega) = \sum_{j=1}^n \frac{1}{\Re(\lambda_j)^2 + (\omega - \Im(\lambda_j))^2}.$$

So, the  $S(\omega)$  just reflects the eigenspectrum distribution. When oscillatory modes

exist,  $\Im(\lambda) \neq 0$ , the spectrum may have peaks; when the system contains only pure damped modes, a red spectrum results (Hasselmann, 1976). Although a spectral peak is often used to indicate the existence of an oscillatory mode, its structure can be largely influenced by the stochastic forcing pattern.

## 2. EOF, singular vector, and stochastic optimal

In studying the dynamical system (2.3), many optimals have been defined to emphasize certain aspects of the response. Here, we briefly review the definitions and applications of three commonly used in meteorology and oceanography: empirical orthogonal function (EOF), singular vector (SV), and stochastic optimal (SO).

### a. EOF

When dealing with a high-dimensional complex system  $\mathbf{x}$ , for example, a coupled atmosphere-ocean general circulation model (GCM) with millions of grid points, one might ask Is there a low-dimensional approximation  $\tilde{\mathbf{x}}$  that still preserves most of the information in  $\mathbf{x}$ ? In terms of variance (energy), a confirmative answer is given by Eckart and Young (1936) and further extended by Mirsky (1960):

$$\min\{\text{var}(\mathbf{x} - \tilde{\mathbf{x}})\} \quad \text{for } \mathbf{x} \in \mathbf{R}^n, \tilde{\mathbf{x}} \in \mathbf{R}^m, m < n. \quad (2.12)$$

Minimization is achieved when  $\tilde{\mathbf{x}} = \sum_{i=1}^m a_i \mathbf{v}_i$ , where  $\mathbf{v}_i$  are the eigenvectors of  $\mathbf{C} = \langle \mathbf{x}\mathbf{x}^T \rangle$ . It is also known as the total least square problem (Huffel and Vandewalle, 1991). A simpler proof is given by Coope and Renaud (2000). In climatology, orthogonal vectors  $\mathbf{v}_i$  are called EOFs, and  $a_i$  are principal component (PC) time series. The variance captured by the first  $m$  EOFs is  $\sum_{i=1}^m a_i^2 = \sum_{i=1}^m \lambda_i(\mathbf{C})$ . As a powerful tool of data analysis, visualization, or compression, the first several EOFs usually explain a large portion of the total variance. See Preisendorfer (1988) for a



comprehensive discussion of this technique.

b. Singular vector

For any initial state  $\mathbf{x}(t_0)$ , deterministic dynamics in system (2.3) determines the unique final state  $\mathbf{x}(t_0 + \tau)$ . One can ask: Is there one  $\mathbf{x}(t_0)$  which grows or decays most rapidly? Mathematically, it is a maximization problem

$$\max \|\mathbf{x}(t_0 + \tau)\|_2 \quad s.t. \quad \mathbf{x}_{t_0+\tau} = e^{A\tau} \mathbf{x}(t_0), \quad \|\mathbf{x}(t_0)\|_2 = 1. \quad (2.13)$$

The answer is the singular vector of the propagator: if  $\mathbf{x}(t_0)$  takes the pattern of the right singular vector  $\mathbf{v}$ , then the final stage would be the left singular vector  $\mathbf{u}$  with growth rate (the singular value)  $s$ . While the singular value decomposition (SVD)  $\exp(A\tau) = \mathbf{U}\mathbf{S}\mathbf{V}^T$  is a standard procedure, it has at least three different uses in atmospheric science: 1) Finding nonmodal growth (Farrell and Ioannou, 1996a). For example, Penland and Sardeshmukh (1995) showed that the growing phase of ENSO can result from optimal perturbation, even though only three damped normal modes are involved. 2) Predicting uncertainty associated with weather and climate forecast (Palmer, 2000). Since dominant singular vectors are the most rapidly growing perturbations, by adding them into initial condition as error, one can estimate the spreading of probability distribution of  $\mathbf{x}$  with relatively fewer runs in comparison with the Monte Carlo method. 3) Providing guideline for adaptive observation strategy (Palmer et al., 1998), i.e. targeting the sensitive region identified by singular vector analysis.

c. Stochastic optimal

Stochastic optimals are a set of particular forcing patterns that give rise to the maximal energy of the system (2.3),

$$\max\{\text{var}(\mathbf{x}) : \boldsymbol{\eta} \text{ real}\} = \max\{\text{tr}(\boldsymbol{\Sigma}\mathbf{B}) : \boldsymbol{\Sigma} = \langle \boldsymbol{\eta}\boldsymbol{\eta}^T \rangle\}. \quad (2.14)$$

Optimization is attained when the forcing covariance matrix  $\boldsymbol{\Sigma}$  and the stochastic dynamical operator  $\mathbf{B}$  have a common set of orthogonal eigenvectors—stochastic optimal  $\mathbf{v}$ . For instance, if the forcing contains only one mode, then the magnitude of the response is largest when the system (2.3) is driven by its first stochastic optimal.

d. Effect of nonnormality

For a normal system, normal modes  $\mathbf{v}_i$ , which are eigenvectors of operator  $\mathbf{A}$ , are orthogonal. According to the Lyapunov equation (2.10) and the property of matrix exponential, singular vectors and stochastic optimals take the form of  $\mathbf{v}_i$  with growth rate

$$\sigma_i(e^{\mathbf{A}t}) = e^{\Re[\lambda_i(\mathbf{A})]t}$$

and response variance

$$\lambda_i(\mathbf{B}) = \frac{-1}{\lambda_i(\mathbf{A}) + \lambda_i^*(\mathbf{A})}.$$

Clearly, there is no (transient) growing mechanism in this system, all initial perturbations monotonically decay to zero. And resonance does occur when forcing takes the pattern of normal modes. As mentioned in Section A.1, however, the EOFs relate not only to normal modes but also to coherent forcing structure. If forcing is unitary, then EOF analysis correctly identifies the dynamical mode and  $\lambda_i(\mathbf{C}) = \lambda_i(\mathbf{B})$ .

For a nonnormal system, eigenvectors  $\mathbf{v}$  are no longer orthogonal, hence mode-to-mode interference may develop, which causes EOFs, SVs, and SOs to deviate

from normal modes. Several matrix inequalities help in estimating the underlying nonnormal effect (see Horn and Johnson, 1985, 1991; Gajić and Qureshi, 1995),

$$e^{\Re[\lambda_1(\mathbf{A})]t} \leq \sigma_1(e^{\mathbf{A}t}) \leq \min\{e^{\lambda_1(\frac{\mathbf{A}+\mathbf{A}^T}{2})t}, \kappa(\mathbf{E})e^{\Re[\lambda_1(\mathbf{A})]t}\}, \quad (2.15)$$

$$\lambda_n(\mathbf{B}), \lambda_n(\mathbf{C}) \leq \frac{1}{-2\Re[\lambda_n(\mathbf{A})]}, \quad (2.16)$$

$$\lambda_1(\mathbf{B}), \lambda_1(\mathbf{C}) \geq \frac{1}{-2\Re[\lambda_1(\mathbf{A})]}, \quad (2.17)$$

where  $\mathbf{C}$  is the covariance matrix under unitary forcing  $\Sigma = \mathbf{I}$ , and

$$\kappa(\mathbf{E}) = \|\mathbf{E}\| \|\mathbf{E}^{-1}\| \geq 1$$

is the condition number of column eigenvector matrix of  $\mathbf{A}$ . In (2.15), the lower bound tells us that nonnormality reduces the decay of the first singular vector. In fact, the initial perturbation may grow, at least temporally, even though all normal modes are damped. This is because  $\mathbf{A} + \mathbf{A}^T$  is not necessarily stable for stable  $\mathbf{A}$ , which means upper bound may be much larger than one for finite lead-time. Farrell and Ioannou (1996a) and reference herein discussed the importance of such nonmodal growth in various flows. For stochastic optimals, (2.16) and (2.17) basically show that nonnormal systems are more extreme. The first SO forcing excites more variance, while the last SO excites less. Meanwhile, the first EOF gains strength at the expense of the last EOF, i.e. the nonnormal system accumulates more energy at the low end of the eigenspectrum of  $\mathbf{C}$ .

## B. Predictability of LTI system

Let  $\mathbf{x}(t)$  be a multivariate stationary random process. Then the best projection of future (given past) is the conditional expectation  $\bar{\mathbf{x}}(t_0 + \tau) = \langle \mathbf{x}(t_0 + \tau) | \mathbf{x}(s), s \leq t_0 \rangle$ . In this dissertation, we call it optimal prediction in mean square sense, which means

that

$$\text{var}(\mathbf{x} - \bar{\mathbf{x}}) = \min[\text{var}(\mathbf{x} - \hat{\mathbf{x}})]$$

among all possible predictions  $\hat{\mathbf{x}}$ . Furthermore, the process described by (2.3) belongs to a special branch—Markov process, which has an important property

$$\langle \mathbf{x}(t_0 + \tau) | \mathbf{x}(s), s \leq t_0 \rangle = \langle \mathbf{x}(t_0 + \tau) | \mathbf{x}(t_0) \rangle. \quad (2.18)$$

Therefore, the optimal prediction of system (2.3) is

$$\bar{\mathbf{x}}(t_0 + \tau) = e^{A\tau} \mathbf{x}(t_0), \quad (2.19)$$

which is also the predictable component in (2.4), namely the signal. The unpredictable component is due to the white noise forcing

$$\mathbf{x}' = \mathbf{x} - \bar{\mathbf{x}} = \int_0^\tau e^{A(\tau-s)} \boldsymbol{\eta}(s + t_0) ds, \quad (2.20)$$

which is called the noise in  $\mathbf{x}$ .

Given the dynamics of (2.3),  $\bar{\mathbf{x}}$  is probably the most reasonable prediction. However other prediction schemes may be used, which is denoted by  $\hat{\mathbf{x}}$ . In order to compare the performance of various models, a metric must be defined. One simple skill measure is the normalized error variance (NEV)

$$\epsilon(\tau) = \frac{\text{var}[\mathbf{x}(t_0 + \tau) - \hat{\mathbf{x}}(t_0 + \tau)]}{\text{var}[\mathbf{x}(t_0)]}, \quad (2.21)$$

where  $\hat{\mathbf{x}}(t_0 + \tau) = f(\mathbf{x}_{t_0}, \dots, \mathbf{x}_{-\infty}; \tau)$  represents our forecasting strategy, such as persistence forecast  $\hat{\mathbf{x}}(t_0 + \tau) = \mathbf{x}(t_0)$ .

Using (2.21), (2.4), stationary condition, and the independence between  $\mathbf{x}(t_0)$  and  $\boldsymbol{\eta}(t_0 + s)$ , one can show

$$\epsilon = \frac{\text{var}(\bar{\mathbf{x}} - \hat{\mathbf{x}}) + \text{var}(\mathbf{x}')}{\text{var}(\mathbf{x})} \geq \frac{\text{var}(\mathbf{x}')}{\text{var}(\mathbf{x})}, \quad (2.22)$$

which confirms the above mentioned Markov property— $\bar{\mathbf{x}}$ , with smallest prediction error, is the best prediction. It should be pointed out that  $\bar{\mathbf{x}}$  also denotes the most probable state for normal distribution. The prediction error of a persistence forecast,

$$\epsilon_{\text{persist}} = \frac{\text{var}[\mathbf{x}(t_0 + \tau) - \mathbf{x}(t_0)]}{\text{var}(\mathbf{x})} = 2[1 - \rho(\tau)], \quad (2.23)$$

relates to another commonly used quantity in time series analysis, autocorrelation function

$$\rho(\tau) = \frac{\langle \mathbf{x}(t_0)^T \mathbf{x}(t_0 + \tau) \rangle}{\langle \mathbf{x}(t_0)^T \mathbf{x}(t_0) \rangle}.$$

And the Fourier transform of  $\rho(\tau)$  is the power spectrum  $S(\omega)$  defined by (2.11). Although  $\rho$  could serve as a rough estimate of predictability: longer (shorter) decorrelation time means system more (less) predictable. It is not a predictability measure in a strict sense, as it is not directly connected to a prediction scheme.

## 1. Predictability measures

According to inequality (2.22), it is natural to define the skill of optimal prediction  $\bar{\mathbf{x}}$  as the measure of predictability and view it as an inherent property of a dynamical system (2.3). A well predictable system is the one with slower error growth compared to signal decaying. However, we are still free to choose a specific metric to quantify this.

### a. Normalized error variance

Using (2.19) and (2.20), we define a measure of the predictability of system (2.3) as

$$\epsilon(\tau) = \frac{\text{var}(\mathbf{x}')}{\text{var}(\mathbf{x})} = \frac{\text{tr}(\mathbf{E}_\tau)}{\text{tr}(\mathbf{C})} = 1 - \frac{\text{tr}(\mathbf{C}_\tau)}{\text{tr}(\mathbf{C})} \quad (2.24)$$

where the covariance matrix of noise  $\mathbf{E}_\tau = \langle (\mathbf{x}')^T (\mathbf{x}') \rangle$ ; the covariance of signal  $\mathbf{C}_\tau = e^{\mathbf{A}\tau} \mathbf{C} e^{\mathbf{A}^T \tau}$ . Since the total response is signal plus noise,  $\mathbf{C} = \mathbf{C}_\tau + \mathbf{E}_\tau$ , predictability measure  $\epsilon$  fall in the range  $[0, 1]$  with  $\epsilon(0) = 0$  and  $\epsilon(-\infty) = 1$ . As lead time goes, the error increases monotonically, until it reaches a certain limit above which we consider the prediction loses its value. If the useful skill requires  $\epsilon \leq 0.5$ , i.e. the signal has larger variance than the noise. Then the time scale given by  $\epsilon(\tau_m) = 0.5$  would be a concise measure of the system's predictability. In this dissertation, we use these two different definitions ( $\epsilon(\tau)$  or  $\tau_m$ ) interchangeably, whose meaning should be clear from context.

Two other similar statistics are also commonly used in characterizing a dynamical system (2.3), normalized signal variance (NSV) and signal-to-noise ratio (SNR). They are simply related to error variance through

$$\text{NSV} = 1 - \epsilon, \quad \text{and} \quad \text{SNR} = \text{NSV}/\epsilon. \quad (2.25)$$

#### b. Measures from information theory

In information theory, entropy is used to measure the uncertainty of a random process (Shannon, 1948),

$$\hbar(\mathbf{x}) = - \int f(\mathbf{x}) \ln f(\mathbf{x}) d\mathbf{x}, \quad (2.26)$$

where  $f(\mathbf{x})$  is the probability density function of  $\mathbf{x}$ . If the p.d.f. of  $\mathbf{x}$  is multivariate normal

$$f(\mathbf{x}) = \frac{1}{(2\pi)^{n/2} \sqrt{\det(\mathbf{C})}} \exp \left[ - \frac{(\mathbf{x} - \boldsymbol{\mu})^T \mathbf{C}^{-1} (\mathbf{x} - \boldsymbol{\mu})}{2} \right], \quad (2.27)$$

where  $\boldsymbol{\mu}$  and  $\mathbf{C}$  are mean and covariance of  $n$ -dimensional r.v.  $\mathbf{x}$ . Then

$$\hbar(\mathbf{x}) = \frac{1}{2} \ln (2\pi e)^n \det(\mathbf{C}). \quad (2.28)$$

Furthermore, it can be proved that the Gaussian process actually maximizes the entropy over all distributions with same covariance (Cover and Thomas, 1991). In other words, uncertainty in normal distribution is the largest. On the other hand, a deterministic process has zero entropy  $\bar{h} = 0$ , i.e. no uncertainty.

Within such context, predictability can be defined as the amount of information that prediction  $\bar{\mathbf{x}}$  contains about  $\mathbf{x}$  (Leung and North, 1990). This is the mutual information concept (Cover and Thomas, 1991),

$$I(\bar{\mathbf{x}}; \mathbf{x}) = \bar{h}(\mathbf{x}) - \bar{h}(\mathbf{x}') = \frac{1}{2} \ln \left[ \frac{\det(\mathbf{C})}{\det(\mathbf{E}_\tau)} \right], \quad (2.29)$$

which represents the predictable information (Schneider and Griffies, 1999). In our case here, it is convenient to work with a derived quantity which we call predictive power loss (PPL)

$$\text{PPL}(\tau) = e^{-\frac{2}{n}I(\bar{\mathbf{x}}; \mathbf{x})} = \det(\mathbf{E}_\tau \mathbf{C}^{-1})^{1/n} \quad (2.30)$$

after the predictive power (PP) of Schneider and Griffies (1999). Using the properties of positive definite matrix, one can show  $0 \leq \text{PPL} \leq 1$ . It is consistent with  $\epsilon(\tau)$  in the sense that  $\text{PPL}(0) = 0$  and  $\text{PPL}(-\infty) = 1$ .

The predictive power loss has some nice mathematical properties such as invariant under linear transformation, which leads to a tight upper bound on PPL,

$$\begin{aligned} \text{PPL}(\tau) &= \det \left( 1 - \frac{\mathbf{C}_\tau}{\mathbf{C}} \right)^{1/n} \\ &\leq \prod_{i=1}^n (1 - e^{2\Re[\lambda_i(\mathbf{A})]})^{1/n} \\ &\leq 1 - \exp \left\{ \frac{2}{n} \sum_{i=1}^n \Re[\lambda_i(\mathbf{A})] \right\}. \end{aligned} \quad (2.31)$$

Tippett and Chang (2003) proved the above inequality and further pointed out that nonnormality or correlated (in normal mode space) stochastic forcing always increase

the system's predictability. Such property also holds for other predictability measures, e.g. relative entropy (Lohmann and Schneider, 1999; Kleeman, 2002; Kleeman et al., 2002) and a set of more general measures (Tippett and Chang, 2003), but not for NEV.

c. Predictability of normal system under unitary forcing

If  $\mathbf{A} = \mathbf{U}\text{diag}(\lambda_i)\mathbf{U}^\dagger$  and  $\Sigma = \mathbf{I}$ , then  $\mathbf{C} = \mathbf{U}\text{diag}(c_i)\mathbf{U}^T$  according to Lyapunov equation (2.9), where  $\mathbf{U}\mathbf{U}^\dagger = \mathbf{I}$  and  $c_i = -1/(\lambda_i + \lambda_i^*)$ . Eqs. (2.24) and (2.30) give the predictability in terms of the normalized error variance

$$\epsilon = 1 - \frac{\sum_{i=1}^n \frac{e^{(\lambda_i + \lambda_i^*)\tau}}{\lambda_i + \lambda_i^*}}{\sum_{i=1}^n \frac{1}{\lambda_i + \lambda_i^*}} \quad (2.32)$$

and predictive power loss

$$\text{PPL} = \prod_{i=1}^n (1 - e^{(\lambda_i + \lambda_i^*)\tau})^{1/n}, \quad (2.33)$$

respectively.

Now let's prove  $\epsilon \leq \text{PPL}$  for a normal system with spatially white stochastic forcing.

*Proof.*<sup>1</sup> Let  $a_i = (\lambda_i + \lambda_i^*)\tau$ ,  $f(x) = \frac{1-e^{-x}}{x}$ , and  $g(x) = \frac{1}{1-e^{-x}}$ . Then  $f(a_i)$  and  $g(a_i)$  are similarly ordered positive sequences. From Čebyše's inequality, we know

$$\sum_{i=1}^n \frac{1}{a_i} = \sum_{i=1}^n f(a_i)g(a_i) \geq \frac{1}{n} \sum_{i=1}^n f(a_i) \sum_{i=1}^n g(a_i),$$

---

<sup>1</sup>This proof is provided by Ioan Gavrea from the Department of Mathematics, Technical University of Cluj Napoca, Romania, E-mail: Ioan.Gavrea@math.utcluj.ro.



which is equivalent with the following

$$\frac{n}{\sum_{i=1}^n g(a_i)} \geq \frac{\sum_{i=1}^n f(a_i)}{\sum_{i=1}^n \frac{1}{a_i}} = \epsilon.$$

While the left hand side is the harmonic mean of  $1 - \exp(-a_i)$ , it satisfies another elementary inequality

$$\text{H.M.} \leq \text{G.M.} \implies \text{PPL} \geq \frac{n}{\sum_{i=1}^n g(a_i)} \geq \epsilon$$

□

For the same threshold, such as  $\text{PPL} = \epsilon = 0.5$ , the PPL measure gives a shorter time scale of predictability than the error variance measure. Note that  $\text{PPL} \geq \epsilon$  does not hold for the general case, i.e. nonnormal system or nonunitary forcing.

## 2. Most predictable pattern and optimal forcing

Predictability defined by (2.24) is a global-mean measure in the sense that it characterizes the system as a whole. In order to investigate the spatial variations in predictability, for example tropical climate being more predictable than extratropics (Graham et al., 2000), two new spatial optimal patterns are defined (Schneider and Griffies, 1999; Chang et al., 2003a,b).

### a. Most predictable pattern

The singular vector (2.13) defines the most rapidly growing pattern without taking stochastic forcing effect into account. In the extreme case, it is entirely possible that the system does not have any projection on this pattern. Consequently, the growth mechanism expressed by SV will not act at all. A new approach, the predictable component analysis, was developed to avoid such problem by focusing on the

response from the very beginning (Schneider and Griffies, 1999; DelSole and Chang, 2003). Suppose patterns  $\mathbf{v}_i$  form a complete set. We can expand  $\mathbf{x}$  in terms of  $\mathbf{v}_i$ ,

$$\mathbf{x}(t) = \sum_{i=1}^n a_i(t) \mathbf{v}_i \quad (2.34)$$

From (2.12), we know that  $\max[\text{var}(a_i)]$  is given by the first EOF. In analogy, here we may define the predictability of  $a_i$  and ask which one has the highest score (more predictable). Assume  $\mathbf{v}_i$  and  $\mathbf{u}_i$  are bi-orthogonal sets. We get  $a_i(t) = \mathbf{u}_i^T \mathbf{x}(t)$  by using  $\mathbf{U}^T \mathbf{V} = \mathbf{I}$ . The predictability of  $a_i(t)$  would be

$$\varepsilon = \frac{\text{var}(a')}{\text{var}(a)} = \frac{\mathbf{u}^T \mathbf{E}_\tau \mathbf{u}}{\mathbf{u}^T \mathbf{C} \mathbf{u}} = 1 - \frac{\mathbf{u}^T \mathbf{C}_\tau \mathbf{u}}{\mathbf{u}^T \mathbf{C} \mathbf{u}}. \quad (2.35)$$

One who is familiar with linear algebra will recognize that  $\min \varepsilon$  is equivalent with a generalized eigenvalue problem:

$$\mathbf{E}_\tau \mathbf{u} = \varepsilon \mathbf{C} \mathbf{u}, \quad \text{or} \quad \mathbf{C}_\tau \mathbf{u} = \gamma \mathbf{C} \mathbf{u}, \quad \text{with } \varepsilon = 1 - \gamma. \quad (2.36)$$

For computational efficiency, the patterns  $\mathbf{V}$  are found through the property of the generalized eigenvectors  $\mathbf{V} = \mathbf{C} \mathbf{U}$  not  $\mathbf{U}^{-1}$ . From now on,  $\mathbf{v}$  and  $\mathbf{u}$  are called predictable pattern and filter, respectively. And the most predictable pattern (MPP) is the one with  $\min \varepsilon$  or  $\max \gamma$ , while the least predictable pattern is with  $\max \varepsilon$  or  $\min \gamma$ . One intuitively appealing interpretation is that the most predictable pattern identifies the region with high predictability, in a way just as the first EOF identifies the most energetic area. Although the predictable component (pattern) analysis is a relatively new technique (Schneider and Griffies, 1999; Chang et al., 2003a), it is rooted in some traditional statistical methods, e.g. canonical correlation analysis and autoregressive models. For that matter, DelSole and Chang (2003) provide an excellent review.

b. Optimal forcing with respect to predictability

In terms of variance, the optimal forcing pattern is stochastic optimal given by (2.14). As far as predictability is concerned, a new set of optimal forcing patterns can be defined as the following: According to (2.5) and (2.24), the maximum predictability

$$\varepsilon_{\min} = \min \frac{\text{tr}(\Sigma \mathbf{B}_\tau)}{\text{tr}(\Sigma \mathbf{B})} \quad \text{for given } \mathbf{B} \quad (2.37)$$

is achieved when the forcing pattern is the generalized eigenvector with the smallest eigenvalue

$$\mathbf{B}_\tau \mathbf{v} = \varepsilon \mathbf{B} \mathbf{v} .$$

When stochastic forcing takes the pattern of the generalized eigenvector with the largest  $\varepsilon_{\max}$ , the dynamical system is least predictable. Essentially, it reveals to what degree the stochastic coherent forcing may affect the system's predictability. The range  $\varepsilon_{\min} \leq \varepsilon \leq \varepsilon_{\max}$  is usually large, which implies that two systems with the same deterministic dynamics may differ substantially in predictability.

### 3. Summary

First, we adopt the normalized error variance as the default measure of predictability. With the full acknowledgement of the beautiful mathematical properties of more advanced measures, we think the normalized error variance gives a more realistic estimate of predictive skill. Second, while singular vector and stochastic optimal serve their own purposes well, they are not the patterns we should look for when dealing with the predictability issues. Instead, the predictable pattern and optimal forcing defined through the generalized eigenvalue problem are the optimal patterns of initial condition and stochastic forcing. Taking a dynamical view of the stochastic model, we may have a more pedagogical interpretation: during certain periods, the

system response may resemble the most predictable pattern. According to our theory, these are also the periods when the system is more predictable. The same applies to stochastic forcing. Following this viewpoint, Flügel et al. (2003) found that predictable patterns can be used to explain the decadal modulation of ENSO prediction, i.e. ENSO is more predictable in the 1980s and less predictable in the 1990s.

For reference, we summarize definitions of various optimals in Table II and provide the following inequalities:

$$1 - e^{2\Re[\lambda_1(\mathbf{A})]\tau} \geq \varepsilon_{\min} \geq \max\{0, 1 - e^{\lambda_1(\mathbf{A}+\mathbf{A}^T)\tau}\}, \quad (2.38)$$

$$1 - e^{2\Re[\lambda_n(\mathbf{A})]\tau} \leq \varepsilon_{\max} \leq 1 - e^{\lambda_n(\mathbf{A}+\mathbf{A}^T)\tau}, \quad (2.39)$$

where  $\varepsilon$  is the generalized eigenvalue in (2.36) or (2.37), i.e. the score associated with predictable pattern or optimal forcing. Generally, the predictable pattern and optimal forcing depend on lead time  $\tau$ . However, we can define global optimals as the patterns at  $\varepsilon(\tau_m) = 0.5$ , which give the maximum predictable time-scale  $\tau_m$ .

### C. A low-dimensional approximation

The analysis in Sections A and B requires dealing with large matrices. For example, the global surface temperature, with  $1^\circ \times 1^\circ$  medium resolution, has  $n \approx 6 \times 10^4$  dimensions (this is what GCMs deal with). Then, with 8 bytes double precision, one  $n \times n$  matrix needs about 30 GB (gigabyte) memory to store it (this is what we are dealing with). Usually there are several climatic variables of interest and matrix computation (e.g. eigendecomposition) also needs some workspace. The total requirement for memory would exceed hundreds of GB, which is a formidable task

Table II. Common optimals  $\mathbf{v}$  of linear stochastic system:  $d\mathbf{x}/dt = \mathbf{A}\mathbf{x} + \boldsymbol{\eta}$ 

name	pattern of	definition
normal mode	$\mathbf{x}$	eigenvector of $\mathbf{A}$ , $\mathbf{A}\mathbf{v} = \lambda\mathbf{v}$
EOF of response	$\mathbf{x}$	eigenvector of $\mathbf{C}$ , $\mathbf{C}\mathbf{v} = \lambda\mathbf{v}$
Singular vector	$\mathbf{x}_{\text{initial}}$	SVD of propagator, $e^{\mathbf{A}\tau}\mathbf{v} = s\mathbf{u}$
most predictable pattern	$\mathbf{x}$	generalized eigenvector, $\mathbf{E}_\tau\mathbf{u} = \lambda\mathbf{C}\mathbf{u}$ , $\mathbf{v} = \mathbf{C}\mathbf{u}$
EOF of forcing	$\boldsymbol{\eta}$	eigenvector of $\boldsymbol{\Sigma}$ , $\boldsymbol{\Sigma}\mathbf{v} = \lambda\mathbf{v}$
Stochastic Optimal	$\boldsymbol{\eta}$	eigenvector of $\mathbf{B}$ , $\mathbf{B}\mathbf{v} = \lambda\mathbf{v}$
optimal forcing for predictability	$\boldsymbol{\eta}$	generalized eigenvector, $\mathbf{B}_\tau\mathbf{v} = \lambda\mathbf{B}\mathbf{v}$

even with today's supercomputers.<sup>2</sup> One way to circumvent this difficulty is to find a low-order model and hope the properties of the original dynamical system can be computed, to a certain accuracy, within that subspace. This is also known as a model reduction problem (Obinata and Anderson, 2000).

In addition to the above technical consideration, there is actually a deep physical reason behind model reduction. Dynamical system theory tells us that under certain circumstances, a finite-dimensional manifold may exist in the infinite-dimensional phase space. Therefore, the full dynamics are in principle determined by a finite number of equations. For example, turbulence is a highly chaotic system. However, if some coherent structures appear within a disordered background flow, one can project the Navier-Stokes equation onto these physical patterns to formulate a low-

<sup>2</sup>For the record, earth simulator, the fastest supercomputer as to 2002, has 10 Tera bytes of main memory.

order model. This is the proper orthogonal method introduced by John L. Lumley (Holmes et al., 1996). In analogy, Patil et al. (2001) demonstrate that another extremely high-dimensional dynamical system, the Earth’s atmosphere, also possesses a local low dimensionality. Hence, a low-order model may be used to evaluate the predictability of a weather system (Lorenz, 1965, 1969). The climate system exhibits certain regularities in space and time, e.g. ENSO, Pacific North American (PNA) pattern, North Atlantic Oscillation (NAO), Arctic Oscillation (AO), Pacific Decadal Oscillation (PDO), and Tropical Atlantic dipole mode. Just like a coherent structure in turbulence lays the ground for low-dimensional modeling (Holmes et al., 1996), the mechanisms of these climate modes may also contain a low order approximation, i.e. the attractors reside in low-dimensional manifolds. Here, our objective is not to make a more efficient, accurate, and economical simulation or prediction, but to develop “simple” models that will lead to better understanding of climate variabilities. Of course to do this, we ignore their interactions with the weather (higher modes) and mean circulation(the lowest mode). In the real world, all of them are integrated into one system which has no boundaries between weather, climate, and global change. However,

often, science progresses by a kind of creative ignorance in which one attempts to focus on key phenomena and ignore second order effects

which is especially true in geophysical fluid dynamics (Pedlosky, 1987). On the other hand, one should be prudent about model reduction: first, not every dynamical system possesses low-dimensional approximation; second, given the degree of freedom  $n$ , the performance of reduced model may change dramatically with the basis of projection.

## 1. Objective

In this section, we assume the dynamical system is precisely described by the full order model (FOM)

$$\frac{d\mathbf{x}}{dt} = \mathbf{A}\mathbf{x} + \boldsymbol{\eta}. \quad (2.40)$$

Through linear transformation  $\mathbf{x} = \mathbf{T}\boldsymbol{\alpha}$ , (2.40) is equal to

$$\frac{d\boldsymbol{\alpha}}{dt} = \tilde{\mathbf{A}}\boldsymbol{\alpha} + \boldsymbol{\zeta},$$

where  $\boldsymbol{\alpha} = \mathbf{T}^{-1}\mathbf{x}$ ,  $\tilde{\mathbf{A}} = \mathbf{T}^{-1}\mathbf{A}\mathbf{T}$ , and  $\boldsymbol{\zeta} = \mathbf{T}^{-1}\boldsymbol{\eta}$ . Suppose, according to some criteria, the first  $m$   $\alpha$ s are far more important than the rest. The reduced order model (ROM) would be

$$\frac{d\boldsymbol{\alpha}_{m \times 1}}{dt} = \tilde{\mathbf{A}}_{m \times m}\boldsymbol{\alpha}_{m \times 1} + \boldsymbol{\zeta}_{m \times 1} \quad (2.41)$$

with  $\boldsymbol{\alpha} = \mathbf{L}\mathbf{x}$ ,  $\tilde{\mathbf{A}} = \mathbf{L}\mathbf{A}\mathbf{R}$ , and  $\boldsymbol{\zeta} = \mathbf{L}\boldsymbol{\eta}$ . The low-order model (2.41) may be thought as a projection (truncation) of FOM into subspace  $\mathbf{R}$ . While left projector  $\mathbf{L}_{m \times n}$  is the first  $m$  rows of  $\mathbf{T}^{-1}$ , the right projector  $\mathbf{R}_{n \times m}$  is the first  $m$  columns of  $\mathbf{T}$ , and they satisfy  $\mathbf{L}\mathbf{R} = \mathbf{I}_{m \times m}$ . Back into original space, (2.41) represents an approximation  $\mathbf{x} \approx \mathbf{R}\boldsymbol{\alpha}$ .

When operator  $\mathbf{A}$  is linear time-invariant and forcing  $\boldsymbol{\eta}$  is white noise, both FOM and ROM become the stochastic models discussed in Sections A and B. Within the context of this dissertation, two intimately related questions can be posed here:

First, if we use ROM to predict the full system, how good is it? To answer this, we define the normalized prediction error in physical space (see Eqs. (2.21) and (2.22)),

$$\epsilon_p = \frac{\text{var}(\mathbf{x} - \mathbf{R}\bar{\boldsymbol{\alpha}})}{\text{var}(\mathbf{x})} = \frac{\text{var}[e^{\mathbf{A}\tau}\mathbf{x}(t_0) - \mathbf{R}e^{\tilde{\mathbf{A}}\tau}\mathbf{L}\mathbf{x}(t_0)]}{\text{var}(\mathbf{x})} + \epsilon, \quad (2.42)$$

where  $\bar{\boldsymbol{\alpha}}$  is the optimal prediction of ROM (2.41), and  $\epsilon$  is the predictability of FOM

(2.40). Eqs. (2.19), (2.20), and (2.24) have been used in derivation. As we know, smaller  $\epsilon_p$  means better prediction, hence better model reduction.

The second question is more related to the issue addressed in this dissertation: Do FOM and ROM have similar predictability? A positive answer will ensure the use of low-order model as a substitute for studying the predictability of a high-order complex system. A successful example along this line is Lorenz's work on atmospheric predictability (Lorenz, 1963, 1965, 1969, 1984). Using double-Fourier series as basis, Lorenz derived low-order atmospheric (nonlinear) models and found useful weather forecasts were limited to two weeks. Even with today's operational numerical weather prediction, this limit still holds (Kalnay et al., 1998). Of course, the nature of predictability are fundamentally different for Lorenz's chaotic model and the stochastic model used here. As mentioned in Chapter I, the loss of prediction skill in the former is due to small initial error plus nonlinearity, i.e. *butterfly effect* (Lorenz, 1993), while the latter is due to unknown forcing (perfect initial condition). However, the basic objectives are the same—solve a low-dimensional model for the answer to an intractable problem, e.g. predictability of weather or climate. Before casting any confidence, we need to know how the model reduction affects the estimate of predictability.

Noticing that NEV (2.24) depends on coordinates, we define ROM's predictability as the ratio of variance in physical space (space of FOM),

$$\epsilon_r(\tau) = \frac{\text{var}(\mathbf{R}\boldsymbol{\alpha} - \mathbf{R}\bar{\boldsymbol{\alpha}})}{\text{var}(\mathbf{R}\boldsymbol{\alpha})} = 1 - \frac{\text{tr}(\mathbf{R}e^{\tilde{\mathbf{A}}\tau}\tilde{\mathbf{C}}e^{\tilde{\mathbf{A}}\tau}\mathbf{R}^\dagger)}{\text{tr}(\mathbf{R}\tilde{\mathbf{C}}\mathbf{R}^\dagger)} \quad (2.43)$$

where  $\tilde{\mathbf{C}} = \langle \boldsymbol{\alpha}\boldsymbol{\alpha}^\dagger \rangle$  is determined via Lyapunov equation:  $\tilde{\mathbf{A}}\tilde{\mathbf{C}} + \tilde{\mathbf{C}}\tilde{\mathbf{A}} = -\tilde{\boldsymbol{\Sigma}}$  with  $\tilde{\boldsymbol{\Sigma}} = \langle \boldsymbol{\zeta}\boldsymbol{\zeta}^\dagger \rangle = \mathbf{L}\boldsymbol{\Sigma}\mathbf{L}^\dagger$ . We want  $\epsilon_r(\tau)$  to approach  $\epsilon(\tau)$  as close as possible.

The above two problems can be written as variations,  $\min \epsilon_p(\tau)$  and  $\min |\epsilon_r(\tau) - \epsilon(\tau)|$ , as they depend on the basis function  $\mathbf{R}$ . Unfortunately, we *do not* have definite answers for them unless the system at hand is very special. Therefore, we will just



compare the performance of several common model reduction methods via an example and hopefully return to this general topic in the future.

## 2. Approximation methods

There are many ways to approximate large-scale dynamical systems, and all have their attributes and drawbacks (see overview by Antoulas and Sorensen, 2001). In this study, we are going to chose four kinds of  $\mathbf{R}$ , namely:

### a. Normal mode

Using normal modes as basis functions is called modal reduction. It separates the  $n$ -dimensional system into  $n$  unrelated one-dimensional systems, which makes the computation much easier ( $\tilde{\mathbf{A}}$  is diagonal). It essentially is a similarity transform, hence preserves the eigenvalues. The traditional wisdom is to choose the least-damped  $m$  modes, with the belief that low modes dominate the long-term response while short-living high modes control rapid transitions. During reduction, the forcing structure has been totally ignored, which will cause severe consequences.

Modal reduction can also be applied to a nonlinear system. Hasselmann (1988) proposed one such method: in general, principal interaction patterns (PIPs) are the default projection basis, which is degenerated to principal oscillation patterns (POPs, i.e, normal modes) in the linear case. Kwasniok (1996, 1997, 2001) tested the PIP reduction method with various dynamical systems, and concluded that PIP is comparable to EOF in model reduction and even more efficient in extracting the essential degrees of freedom (Achatz and Schmitz, 1997).

b. EOF

EOF truncation is not unfamiliar to atmospheric scientists and oceanographers. With a low-order model in EOF space, we can study ENSO dynamics and its prediction (Penland and Magorian, 1993; Xue et al., 1994; Johnson et al., 2000; Timmermann et al., 2001), predictability of climate and extratropical synoptic systems (Blumenthal, 1991; Schneider and Griffies, 1999; Wang, 2001), barotropic and baroclinic flow (Selten, 1995, 1997), midlatitude storm tracks (Zhang and Held, 1999), and other low-frequency variability in the atmosphere (Achatz and Branstator, 1999; D’Andrea and Vautard, 2001; Winkler et al., 2001). The popularity of this method is far beyond atmospheric science and oceanography. It is known as principal component analysis, factor analysis, or total-least-squares estimation in statistics and data processing; proper orthogonal decomposition in the context of turbulence (Holmes et al., 1996); and Karhunen-Loève decomposition in mathematical physics. The wide use is partially due to the easy implementation, partially rooted in the firm mathematical ground—Eckart-Young-Mirsky theorem guarantees the optimality of EOF (Eckart and Young, 1936; Mirsky, 1960). Note the problem formulated here is different from (2.12), and therefore ROM in EOF subspace is only sub-optimal at best. Using the orthogonality of EOF and Lyapunov theorem, however, we can prove the reduced model is stable and  $\tilde{\mathbf{C}} = \text{diag}[\lambda_i(\mathbf{C})]$ , where  $\lambda_i$ s are the variances of  $m$  EOFs.

c. Balanced truncation

Another sub-optimal model reduction is the balanced truncation (BT) method proposed by Moore (1981) in the context of control theory. It has been tested extensively since and proved superior over most other methods (Obinata and Anderson, 2000). It has several useful properties, such as retaining the stability, the truncation

error being upper bounded, and extendability to nonlinear system. Recently, Farrell and Ioannou (2001a,b) introduced this idea into atmospheric science and showed that balanced truncations do improve the performance of ROM.

Even though balanced truncation is a well-known procedure in standard textbooks (Dullerud and Paganini, 2000), some details are given here because of its new appearance in our field. The autonomous system (2.40) can be written as a trivial controlled system

$$\begin{aligned}\frac{d\mathbf{x}}{dt} &= \mathbf{A}\mathbf{x} + \boldsymbol{\eta} \\ \mathbf{y} &= \mathbf{x}.\end{aligned}\tag{2.44}$$

With respect to (2.44), internal balancing is seeking a similarity transformation  $\mathbf{T}$  that results in a diagonal covariance matrix and stochastic optimal,

$$\tilde{\mathbf{C}} = \tilde{\mathbf{B}} = \boldsymbol{\Phi} = \text{diag}[h_1, h_2, \dots, h_n]$$

where  $\tilde{\mathbf{C}} = \mathbf{T}^{-1}\mathbf{C}\mathbf{T}^{-\dagger}$ ,  $\tilde{\mathbf{B}} = \mathbf{T}^{\dagger}\mathbf{B}\mathbf{T}$ , and the Hankel singular value  $h_1 \geq h_2 \geq \dots \geq h_n > 0$  reflects the relative contribution of the corresponding mode. Using the first  $k$  modes to form  $\mathbf{L}$  and  $\mathbf{R}$ , (2.41) would be the BT version of (2.40). Here, it is helpful to think of the balanced truncation as a combination of EOFs and SOs. Taking both dynamics and forcing into consideration, balanced truncation is found to be nearly optimal in fluid flow problems (Farrell and Ioannou, 2001a).

Following Lall et al. (2002), balancing two covariance matrices can be done in three steps. First, construct a Cholesky factorization of  $\mathbf{B}$  such that  $\mathbf{B} = \mathbf{Z}^{\dagger}\mathbf{Z}$ , where  $\mathbf{Z}$  is an upper triangular matrix. Then, let  $\mathbf{U}\boldsymbol{\Phi}^2\mathbf{U}^{\dagger}$  be a singular value decomposition of  $\mathbf{Z}\mathbf{C}\mathbf{Z}^{\dagger}$ , and let  $\mathbf{T} = \mathbf{Z}^{-1}\mathbf{U}\boldsymbol{\Phi}^{\frac{1}{2}}$  and  $\mathbf{T}^{-1} = \boldsymbol{\Phi}^{-\frac{1}{2}}\mathbf{U}^{\dagger}\mathbf{Z}$ . Finally,  $\mathbf{T}^{\dagger}\mathbf{B}\mathbf{T} = \boldsymbol{\Phi}$  and  $\mathbf{T}^{-1}\mathbf{C}\mathbf{T}^{-\dagger} = \boldsymbol{\Phi}$ .

d. Most predictable pattern

In analogy to EOF decomposition, we can project the dynamical system  $\mathbf{x}$  into subspace  $\mathbf{R}$  and define a predictability measure there

$$\gamma(\mathbf{L}) = \frac{\text{tr}\{\mathbf{L}\mathbf{C}_\tau\mathbf{L}^\dagger\}}{\text{tr}\{\mathbf{L}\mathbf{C}\mathbf{L}^\dagger\}}. \quad (2.45)$$

where  $\mathbf{L}$  is the projector,  $\mathbf{L}\mathbf{R} = \mathbf{I}$ . Then,

$$\begin{aligned} \max_{\mathbf{L} \in \mathbf{R}^{m \times n}} \gamma(\mathbf{L}) &= \max \frac{\text{tr}\{\mathbf{L}\mathbf{C}_\tau\mathbf{L}^T\}}{\text{tr}\{\mathbf{L}\mathbf{X}\mathbf{X}^T\mathbf{L}^T\}} && \text{Cholesky decomposition : } \mathbf{C} = \mathbf{X}\mathbf{X}^T \\ &= \max \frac{\text{tr}\{\mathbf{L}\mathbf{C}_\tau\mathbf{L}^T\}}{\text{tr}\{\mathbf{Y}\mathbf{Y}^T\}} && \mathbf{Y}_{m \times n} = \mathbf{L}_{m \times n}\mathbf{X}_{n \times n} \\ &= \max\{\text{tr}(\mathbf{Y}\mathbf{\Omega}\mathbf{Y}^T) : \mathbf{Y}\mathbf{Y}^T = \mathbf{I}_{m \times m}\} && \mathbf{\Omega} = \mathbf{X}^{-1}\mathbf{C}_\tau\mathbf{X}^{-T} \\ &= \frac{1}{m} \sum_{i=1}^m \gamma_i \geq \frac{\text{tr}(\mathbf{C}_\tau)}{\text{tr}(\mathbf{C})} \end{aligned} \quad (2.46)$$

is attained when  $\mathbf{R}$  takes the form of the first  $m$  most predictable patterns. In other words,  $\mathbf{L}$  are the first  $m$  filters in (2.36). Note that the measure (2.45) is defined in an oblique coordinate system, and therefore the maximization of  $\gamma$  does not transfer back to the physical space. However, MPP does have its own merit: it can be viewed as a balance between  $\mathbf{C}_\tau$  and  $\mathbf{C}$ . Let  $\mathbf{T}$  denote the MPP defined by the generalized eigenvalue problem, then we have the following property

$$\mathbf{T}^{-1}\mathbf{C}_\tau\mathbf{T}^{-\dagger} = \text{diag}[\gamma_i] \quad \text{and} \quad \mathbf{T}^{-1}\mathbf{C}\mathbf{T}^{-\dagger} = \mathbf{I}$$

where  $\gamma_i$  is the generalized eigenvalue in (2.36) (see, e.g. DelSole and Chang, 2003). Therefore this method may give a better reduction in terms of  $\epsilon_\tau$  and lead to a deeper understanding of the role of MPP in a linear stochastic system. Again, using Lyapunov's theorem, one can show that this method preserves the stability of  $\mathbf{A}$ .

### 3. EOFs are normal modes

EOFs depict normal modes of (2.40) only when the system is normal  $\mathbf{A}\mathbf{A}^\dagger = \mathbf{A}^\dagger\mathbf{A}$  and forcing patterns coincide with normal modes. Assuming the unitary matrix  $\mathbf{V}$  consists of these orthonormal modes, we have diagonal forms such as

$$\mathbf{A} = \mathbf{V}\text{diag}[a_i]\mathbf{V}^\dagger, \quad (2.47)$$

$$\mathbf{B} = \mathbf{V}\text{diag}[b_i]\mathbf{V}^\dagger, \quad (2.48)$$

$$\mathbf{C} = \mathbf{V}\text{diag}[c_i]\mathbf{V}^\dagger, \quad (2.49)$$

$$\mathbf{\Sigma} = \mathbf{V}\text{diag}[d_i]\mathbf{V}^\dagger, \quad (2.50)$$

where  $\mathbf{V}$  is arranged in such an order that  $0 > \Re(a_1) \geq \Re(a_2) \cdots \geq \Re(a_n)$ . According to Lyapunov equations (2.9) and (2.10),  $b$  and  $c$  depend on  $a$  and  $d$ ,

$$c_i = \frac{-d_i}{a_i + a_i^*} \quad \text{and} \quad b_i = \frac{-1}{a_i + a_i^*}. \quad (2.51)$$

Note that  $d_i$ , hence  $c_i$ , are not necessarily in descending order.

Now, different model reduction methods are simplified to be different ways of choosing  $m$  EOFs from set  $\mathbf{V} = [\mathbf{v}_1, \mathbf{v}_2, \cdots, \mathbf{v}_n]$ . For example, modal and MPP reduction use the least damped modes, i.e.  $\mathbf{v}_1, \cdots, \mathbf{v}_m$ ; EOF reduction picks out the most energetic modes  $c_i$ ; while BC chooses the modes with the largest Hankel singular values  $h_i = \sqrt{c_i b_i}$ . Generally speaking, let  $[l_1, \cdots, l_m]$  be the permutation of  $[1, \cdots, n]$ ,  $\mathbf{R} = [\mathbf{v}_{l_1}, \cdots, \mathbf{v}_{l_m}]$ , then  $\mathbf{L} = \mathbf{R}^\dagger$ , prediction error of ROM (Eq. 2.42)

$$\epsilon_p = \epsilon_t + \epsilon = 1 - \frac{\sum_{i=1}^m e^{(a_{l_i} + a_{l_i}^*)\tau} c_{l_i}}{\sum_{i=1}^n c_{l_i}}, \quad (2.52)$$

and the predictability of ROM (Eq. 2.43)

$$\epsilon_r = 1 - \frac{\sum_{i=1}^m e^{(a_{l_i} + a_{l_i}^*)\tau} c_{l_i}}{\sum_{i=1}^m c_{l_i}}, \quad (2.53)$$

where  $\epsilon_t = \epsilon_p - \epsilon$  is the error due to reduction, and  $\epsilon$  is the predictability of FOM. If  $m = n$ , then  $\epsilon_p = \epsilon_r = \epsilon$ . When  $m < n$ , the minimum prediction error (2.52) is achieved if the reduction is through the first  $m$  EOFs of  $\mathbf{C}_\tau$ , i.e. modes with large variance  $e^{a_i+a_i^*}c_i$ . Comparing  $\epsilon_r$  with  $\epsilon$ , we see that the reduced order model can either overestimate or underestimate the predictability. The details depend on the combination of  $\lambda_i$  and  $d_i$ .

One special case, for which we can obtain some analytical answers, is spatially-white noise, i.e.  $d_1 = d_2 = \dots = d_n = 1$ . Under such forcing,  $c_i = b_i$ , and all the reduction methods discussed give the same results. The reduction via the first  $m$  modes gives

$$\epsilon_p^{\min} = 1 - \frac{\sum_{i=1}^m \frac{e^{(a_i+a_i^*)\tau}}{a_i+a_i^*}}{\sum_{i=1}^n \frac{1}{a_i+a_i^*}} \quad \text{and} \quad \epsilon_r^{\min} = 1 - \frac{\sum_{i=1}^m \frac{e^{(a_i+a_i^*)\tau}}{a_i+a_i^*}}{\sum_{i=1}^m \frac{1}{a_i+a_i^*}}, \quad (2.54)$$

while the reduction via last  $m$  modes has

$$\epsilon_p^{\max} = 1 - \frac{\sum_{i=n-m+1}^n \frac{e^{(a_i+a_i^*)\tau}}{a_i+a_i^*}}{\sum_{i=n-m+1}^n \frac{1}{a_i+a_i^*}} \quad \text{and} \quad \epsilon_r^{\max} = 1 - \frac{\sum_{i=n-m+1}^n \frac{e^{(a_i+a_i^*)\tau}}{a_i+a_i^*}}{\sum_{i=n-m+1}^n \frac{1}{a_i+a_i^*}}. \quad (2.55)$$

One can easily prove  $\epsilon_r^{\min} < \epsilon$  and  $\epsilon_r^{\max} > \epsilon$  for arbitrary reduction,

$$\epsilon_p^{\min} \leq \epsilon_p \leq \epsilon_p^{\max} \quad \text{and} \quad \epsilon_r^{\min} \leq \epsilon_r \leq \epsilon_r^{\max}, \quad (2.56)$$

where  $\epsilon_p$  and  $\epsilon_r$  are given by (2.52) and (2.53). Therefore, within this case the usual model reduction (Modal, EOF, BT, or SO) is the global optimal reduction in the sense that its prediction error is minimal at every lead time  $\tau$ , although it always overestimates the predictability.

To illustrate the basic idea, we present an example here.

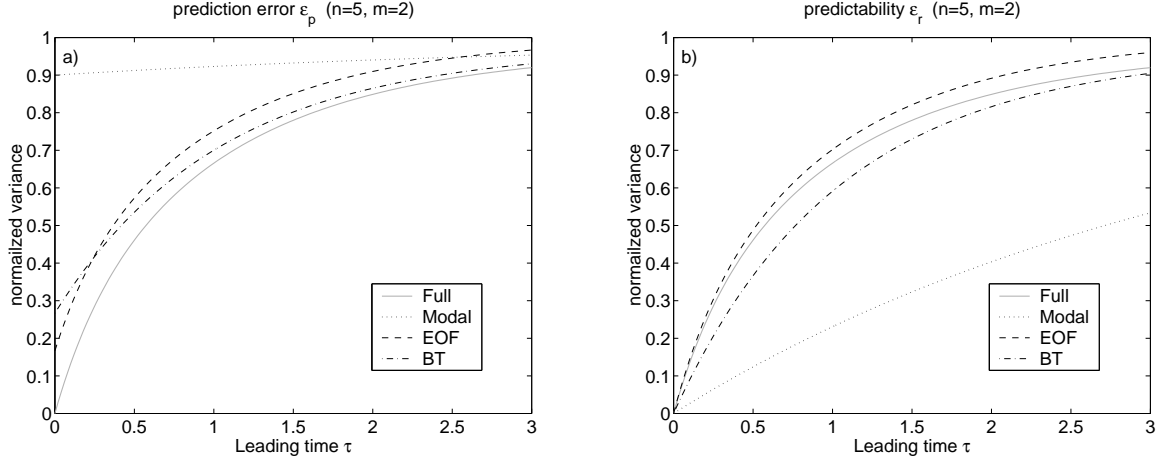


Fig. 1. Performance of different model reductions in Example 1. a) Normalized error variance of prediction; b) predictability of low-order model. Light solid line, skill of full-order model; dotted line, modal reduction; dashed line, EOF truncation; dot-dashed line, BT reduction. Note two light solid lines in a) and b) are identical because we define the normalized error variance of optimal prediction as the predictability.

### Example 1

Let us assume the eigenvalues of the dynamical operator  $A$  and the stochastic forcing covariance  $\Sigma$  are

$$[a_i] = -[0.1, 0.2, 0.3, 0.4, 0.5, 0.6] \quad \text{and} \quad [d_i] = [1, 1, 5, 0.1, 10, 0.1],$$

respectively. Then the skill of modal, EOF, BT, and MPP reduction can be calculated according to Eqs. (2.52) and (2.53). The results for the reduced-order model with two dimensions are presented in Fig. 1.

Figs. 1 a) and b) show that modal reduction is the worst both in terms of prediction and assessing predictability. This is not a surprising result given the setting of  $A$  and  $\Sigma$ , i.e. the least damped modes are not representative in this system. On the contrary, taking the forcing effect into account, EOF and BT reduction produce

much better results. While the EOF truncation overestimates the predictability and BT underestimates it (Fig. 1b), their performances are comparable. However, there are some subtle differences in prediction errors (Fig. 1). When  $\tau = 0$ ,  $\epsilon_p$  represents the error in initial condition due to truncation. From (2.12), we know EOF gives the smallest error. When  $\tau \rightarrow \infty$ , the least damped normal mode dominates, which is well captured by modal reduction. BT somehow combines the benefits of modal and EOF reduction, yielding an overall better prediction. In this case, MPPs are the least damped normal modes, hence it does not give any new information. We have to wait until the next section to see the pros and cons of MPP reduction.

#### 4. EOFs aren't normal modes

Generally, there are two reasons for EOFs  $\neq$  Normal modes: the system is non-normal and the stochastic forcing patterns differ from the normal modes. Such a system is too complex to be solved analytically. We mainly illustrate some ideas with the help of a simple Tropical Atlantic model (Chang et al., 2003b). Before proceeding, let us first consider a very special case where the system is represented by one mode.

When  $m = 1$ ,  $\mathbf{L}$  and  $\mathbf{R}$  would degrade to row vector  $\mathbf{l}$  and column vector  $\mathbf{r}$ , and  $\epsilon_\tau$  is simply an exponential function of  $\tau$ ,

$$\epsilon_{(\tau)} = 1 - e^{(\tilde{a} + \tilde{a}^*)\tau} \quad (2.57)$$

where  $\tilde{a} = \mathbf{lAr}$  is a number. The exponent  $\tilde{a} + \tilde{a}^*$  satisfies the (elementary) algebraic Lyapunov equation,

$$(a + a^*)\mathbf{lC}\mathbf{l}^\dagger = -\mathbf{l}\mathbf{l}^\dagger, \quad (2.58)$$

under unitary forcing  $\Sigma = \mathbf{l}$ . For modal and EOF reduction, we have simple solutions,

$$a + a^* = 2\Re[\lambda_1(\mathbf{A})] \quad \text{and} \quad \frac{-1}{\lambda_1(\mathbf{C})}.$$



However, the optimization property of eigenvalues tells us that  $a + a^*$  is bounded,

$$\frac{-1}{\lambda_{\min}(\mathbf{C})} \leq a + a^* = \frac{-\mathbf{II}^\dagger}{|\mathbf{CI}^\dagger|} \leq \frac{-1}{\lambda_{\max}(\mathbf{C})}. \quad (2.59)$$

In other words, among all reduction methods, the one-dimensional model from EOF truncation possesses maximum predictability.

To make sense of these mathematical concepts, let us turn to a simple but physically more relevant model – a coupled climate model of tropical Atlantic variability (see Chang et al., 2001, for details). The purpose of this model is to study the inter-hemispheric SST variability with a set of reduced physical elements: a zonal averaged temperature equation with northward oceanic mean transport, oceanic damping, and positive air-sea feedback. With all these simplifications, one arrives at a simple linear stochastic climate model,

$$\frac{\partial T}{\partial t} + V \frac{\partial T}{\partial y} + \lambda T - \kappa \frac{\partial^2 T}{\partial y^2} = \beta S(y) T_{\text{ITCZ}} + \eta \quad (2.60)$$

where mean current  $V$ , damping rate  $\lambda$ , and coupling pattern  $S$  are spatial functions based on GCM analysis as well as observations;  $T_{\text{ITCZ}}$  denotes the SST over the active coupling region—ITCZ; diffusion  $\kappa = 1 \times 10^4 \text{m}^2/\text{s}$ ; coupling strength  $\beta = 1/200 \text{day}^{-1}$ ; and  $\eta$  is the spatial-white noise. Here, it is the coupling between atmosphere and ocean that makes the system nonnormal, i.e. the normal modes are not orthogonal. The least damped mode, a dipole, is an oscillatory one with period of about 6 years, which is determined by the mean current. If we define  $\epsilon \leq 0.5$  as a useful skill, TAV is predictable up to two seasons (light solid line in Figs. 2 and 3). However, the predictability comes mainly from coupling (nonnormality) and less from oscillating modes. See Chang et al. (2003b) for an extensive discussion about predictability, including predictable component analysis, of model (2.60).

In this study, we are more interested in the influence of model reduction on

evaluation of predictability. More precisely, do the reduced order models agree well with the full order model in terms of predictability? To answer that question, let us consider a severely truncated model with only one mode (Fig. 2). Similar to Example 1, here we see the same trend in prediction error (panel a.): EOF truncation gives a better prediction at small lead time, while modal reduction does well at longer lead time; BT balances these two, hence perform better overall. However, the large error of short-term prediction by modal reduction and long-term prediction by EOF truncation is due to the nonnormal effect, not the forcing effect as shown in Example 1. When the most predictable pattern at  $\tau = 6$  months is used in reduction, the prediction error grows like EOF truncation, albeit with larger amplitude. Unlike the reduction of a normal system (Example 1), Fig. 2b shows EOF, MPP, and BT reductions of TAV overestimate its predictability while modal reduction underestimates its predictability. And EOF truncation produces the most predictable one-dimensional model, which is proved in inequality (2.59). Another interesting finding from Fig. 2 is that the full system (TAV, light solid line) is more predictable than the least-damped normal mode (dipole, dotted line). This is due to nonnormality induced by the coupling, which can be firmly established by following two inequalities (Gajić and Qureshi, 1995),

$$\text{Normal System} \quad 1 - e^{(\lambda_n(\mathbf{A}) + \lambda_n^*(\mathbf{A}))\tau} \geq \epsilon \geq 1 - e^{(\lambda_1(\mathbf{A}) + \lambda_1^*(\mathbf{A}))\tau}, \quad (2.61)$$

$$\text{Nonnormal system} \quad 1 - e^{\lambda_n(\mathbf{A} + \mathbf{A}^\dagger)\tau} \geq \epsilon \geq 1 - e^{\lambda_1(\mathbf{A} + \mathbf{A}^\dagger)\tau}. \quad (2.62)$$

where  $\lambda_n(\mathbf{A}) + \lambda_n^*(\mathbf{A}) \geq \lambda_n(\mathbf{A} + \mathbf{A}^\dagger)$  and  $\lambda_1(\mathbf{A}) + \lambda_1^*(\mathbf{A}) \leq \lambda_1(\mathbf{A} + \mathbf{A}^\dagger)$ . Basically, (2.61) and (2.62) tell us that a normal system can not be more predictable than its first normal mode, while the nonnormal system can. In other words, the nonnormal system is more extreme, i.e. more or less predictable than the normal system. Although the

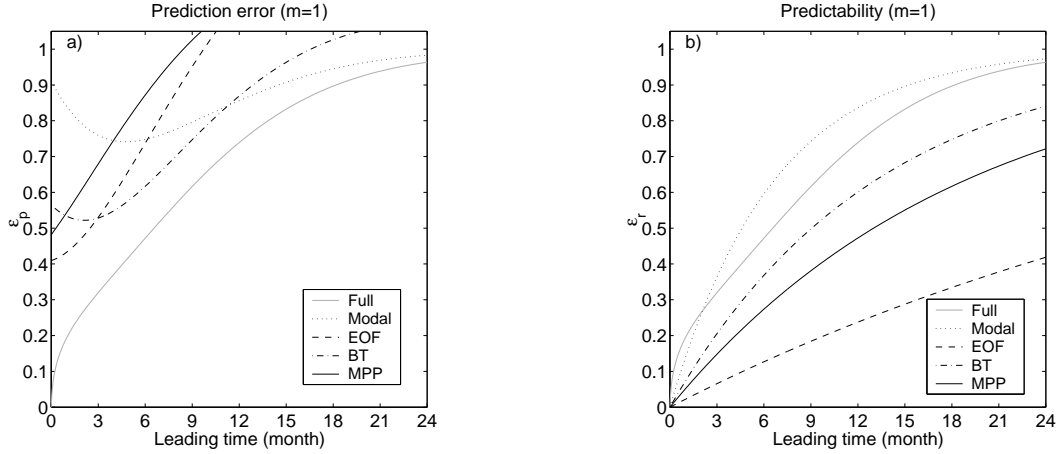


Fig. 2. Reduced order model of tropical Atlantic variability ( $m=1$ ). a) Normalized error variance of prediction; b) predictability of low-order model. Light-thick solid line, full-order model; dotted line, modal reduction; dashed line, EOF truncation; dot-dashed line, BT reduction; solid line, MPP reduction.

predictability of TAV is roughly captured by one normal mode, such agreement does not hold as more modes are included in the reduced order model.

Fig. 3 shows the skill of a truncated model of TAV with four modes. As the number of modes increases, the truncated models using EOF, BT, and MPP methods all give a more accurate description of TAV, both in terms of prediction error and predictability. Nevertheless, there are still some subtle differences: while BT produces the best prediction, MPP reduction preserves the predictability of TAV better. However, a surprising result comes from modal reduction. It does not converge to the full system at all. When four normal modes are used, not only does prediction get worse, except for longer-lead time (Fig. 3 a), the predictability estimate also further deviates from its real value. The poor performance of modal reduction is due to the lack of nonnormality: when we project the full system onto its normal mode space, a nonnormal operator  $\mathbf{A}$  becomes a normal operator. In other words, modal reduction does not preserve nonnormality. However, *it is the nonnormality (coupling) that*

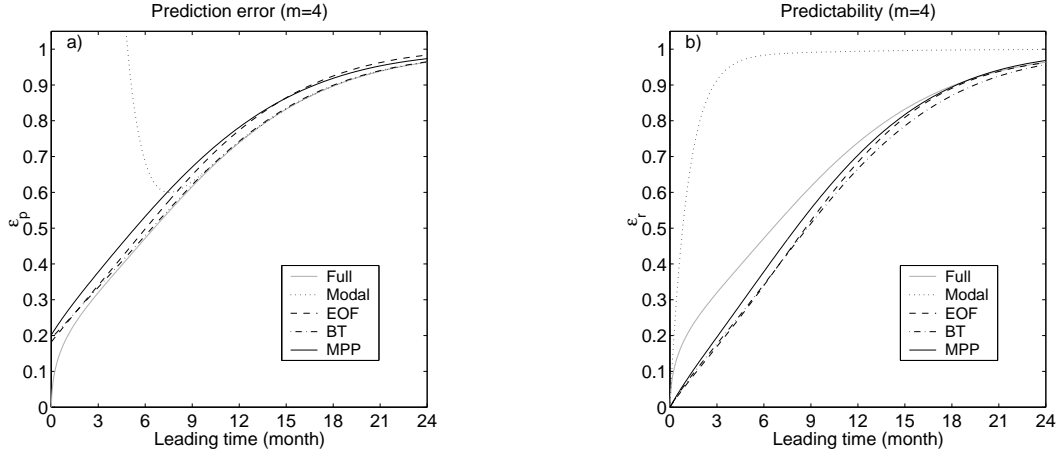


Fig. 3. Reduced order model of tropical Atlantic variability ( $m=4$ ). a) Prediction error; and b) predictability of various lower order model. Line styles are same as that of Fig. 2.

determines the error growth of TAV. Without this air-sea feedback, tropical Atlantic variability is far less predictable. As we said before, nonnormal growth only dominates the short-time prediction, but for the long lead-time, only the least normal modes survive. This explains the almost perfect prediction made by four normal modes for lead time greater than 9 months.

## 5. Some thoughts

Four model reduction methods — modal truncation, EOF truncation, balanced truncation, and MPP truncation, have been tested with two examples. Among them, modal reduction is not an encouraging technique. It ignores the forcing effect and destroys the nonnormality, hence the inherent properties of the full system is lost. EOF truncation has long been used in prediction and predictability analysis because of its robustness and easy implementation. However, one should keep in mind that EOF truncation only keeps the leading modes which are usually large-scale and long-lived. Such low-pass filtering of the data is likely to artificially enhance the persistence

and the predictability (Munk, 1960). In our context, EOF truncation overestimates the system's predictability, the degree of which depends on the number of EOFs being used. Balanced truncation, introduced to atmospheric science recently (Farrell and Ioannou, 2001a,b), is another promising method. It combines the merits of modal reduction and EOF truncation and creates an overall better representation of the full dynamical system. Its use, however, largely depends on how easy it is to find the stochastic operator  $\mathbf{B}$ . In climate studies, usually at least one realization is available, so we know the covariance matrix  $\mathbf{C}$  by assuming ergodicity. Finding  $\mathbf{B}$ , on the other hand, is not a trivial task. It is equivalent to solving the covariance matrix of its adjoint system. At last, we propose a new method, MPP truncation, which is the default pattern for predictability analysis. Again, computational difficulty may limit its use in practice.

Some insight of the dynamical system (2.3) is also gained from this study. Three factors interact in a linear stochastic system, normal modes, forcing patterns, and nonnormality (e.g. air-sea feedback in TAV). Normal modes and coherent forcing together determine the system's response. Therefore, the leading EOF may not be consistent with the least damped normal mode. Through stochastic resonance, forcing affects the predictability: if the least (most) damped modes are excited, the system is most (least) predictable. For the prediction problem, short-term error growth is mainly caused by nonnormality, which is revealed by an SVD analysis of the propagator. As a consequence, a nonnormal system could be more predictable than that indicated by its first normal mode. In general, predictability of one dynamical system can not be inferred from its normal modes, i.e. the stability analysis. This seems against the conventional wisdom that the system's predictability is determined by the leading oscillating mode. This issue will be investigated in the next chapter. We think, as many have advocated already (e.g. Farrell and Ioannou, 1996a; Neumaier

and Schneider, 2001), that a systematic strategy has to be taken in order to achieve a profound understanding of the climate system: Stability + Stochastic Optimal + Predictable Component (SSP) analysis. This strategy has been applied to the study of the predictability of tropical Atlantic variability (Chang et al., 2003b). The following two chapters give two more examples on how the predictability of a climate system can be understood.

#### D. Numerical recipes

Given a dynamical system  $\mathbf{y}$ , our first task is to decide whether a linear model

$$\frac{d\mathbf{x}}{dt} = \mathbf{A}\mathbf{x} + \boldsymbol{\eta} \quad (2.63)$$

is a good approximation, i.e.  $\mathbf{y} \approx \mathbf{x}$ . Very often, it can not be answered until the linear model has been built and tested against  $\mathbf{y}$ . If we assign an answer *yes*, the next step is to estimate dynamical operator  $\mathbf{A}$  and forcing  $\boldsymbol{\eta}$ . Depending on one's knowledge of  $\mathbf{y}$ , one may proceed in two ways,

**Forward approach** We assume that a set of nonlinear equations describing climate variability is known. Then a linear approximation can be defined with respect to certain mean state;

**Inverse approach** We assume that only observation  $\mathbf{y}$  is known. Then a linear equation describing  $\mathbf{y}$  can be estimated via a linear inverse modeling (LIM).

Linearizing a dynamical system is a classical procedure. The advantage is that from the beginning we know clearly which physical processes are included. The difficulty is that, often in practice, the governing equation is either unknown or too complex to be linearized. The LIM method avoids such difficulty by estimating  $\mathbf{A}$  directly from observation. Its computational algorithm is briefly reviewed here, and interested

readers are referred to a series of papers by Cécile Penland and her collaborators (Penland and Magorian, 1993; Penland and Ghil, 1993; Penland and Sardeshmukh, 1995; Penland and Matrosova, 1998; Penland et al., 2000; Penland and Matrosova, 2001).

Suppose that observation  $\mathbf{y}(t)$  is stationary, and we want to find the best fit of a linear model (2.63). According to Eq. (2.4), the fitting is equivalent to constructing an autoregressive (AR) model

$$\mathbf{x}(t_0 + \tau) = \mathbf{P}\mathbf{x}(t_0) + \boldsymbol{\xi} \quad (2.64)$$

where unknown noise  $\boldsymbol{\xi}$  is assumed independent of  $\mathbf{x}$ . The best-fit propagator is found through least squares estimator,

$$\mathbf{P} = \frac{\langle \mathbf{y}(t_0 + \tau)\mathbf{y}^T(t_0) \rangle}{\langle \mathbf{y}(t_0)\mathbf{y}^T(t_0) \rangle}. \quad (2.65)$$

Then, eigen-decomposition of  $\mathbf{P}$  yields the dynamical operator  $\mathbf{A}$ ,

$$\mathbf{P} = e^{\mathbf{A}\tau} = \mathbf{U}\text{diag}(\gamma_i)\mathbf{U}^{-1} \implies \mathbf{A} = \mathbf{U}\text{diag}(\lambda_i)\mathbf{U}^{-1} \quad (2.66)$$

where  $\lambda_i = \ln(\gamma_i)/\tau$ . Here, one needs to test whether  $\mathbf{A}$  is independent of lag  $\tau$ . For the non-autonomous operator, the analysis laid out in this chapter does not apply (Blumenthal, 1991; Farrell and Ioannou, 1996b).

For time-invariant stable  $\mathbf{A}$ , the covariance matrix of noise is computed via Lyapunov equation

$$-\hat{\boldsymbol{\Sigma}} = \mathbf{A}\hat{\mathbf{C}} + \hat{\mathbf{C}}\mathbf{A}^T,$$

where sampling covariance  $\hat{\mathbf{C}} = \langle \mathbf{y}\mathbf{y}^T \rangle$ . However, the above estimation does not guarantee the positive-definiteness of  $\hat{\boldsymbol{\Sigma}}$ . It should be adjusted by replacing the non-positive eigenvalues with small positive numbers. The new forcing covariance  $\boldsymbol{\Sigma}$  is

then used to solve for a new  $\mathbf{C}$ , because  $\mathbf{A}$ ,  $\mathbf{C}$ , and  $\mathbf{\Sigma}$  of linear stochastic model (2.63) have to satisfy the Lyapunov equation:

$$\mathbf{AC} + \mathbf{CA} = -\mathbf{\Sigma}.$$

Once we know  $\mathbf{C}$  and  $\mathbf{A}$ , the rest of the analysis follows.

Another issue related to stochastic models is the white noise assumption. Based on time-scales separation, Hasselmann (1976) argued that the weather system is a white noise generator for the climate system. A rigorous test of that idea is challenging, if not impossible. Furthermore, the stochastic forcing may include some climate noise which is red (Roulston and Neelin, 2000). Therefore, it is an essential step to check the whiteness of  $\eta$  in our linear stochastic modeling framework. Here is a simple testing procedure based on autocorrelation (Lütkepohl, 1993):

Let  $\eta(t)$  be a univariate stochastic time series of length  $N$ , its sample autocorrelation function is

$$\rho(\tau) = \frac{\frac{1}{N-\tau} \sum_{t=1}^{N-\tau} \eta(t)\eta(t+\tau)}{\frac{1}{N} \sum_{t=1}^N \eta(t)\eta(t)}.$$

Now, the null hypothesis for white noise is posed as

$$H_0 : \rho(\tau) = 0 \quad \text{against} \quad H_1 : \rho(\tau) \neq 0. \quad (2.67)$$

On the other hand, the asymptotic distribution of  $\rho(\tau)$  is proved to be a normal distribution  $\sim \mathcal{N}(0, \frac{1}{N})$ . Therefore, if  $|\rho| > 1/\sqrt{N}$ , then  $H_0$  is rejected with 70% confidence interval; if  $|\rho| > 2/\sqrt{N}$ ,  $H_0$  is rejected with 95% confidence interval. In layman language, if we calculate autocorrelation at 20 lags  $\tau = 1, \dots, 20$  and find two of them greater than  $2/\sqrt{N}$ , then the stochastic process  $\eta$  is unlikely to be a white noise. Since red noise can always be simulated by another linear stochastic model, this issue does not invalidate our fundamental strategy here, but it does affect the



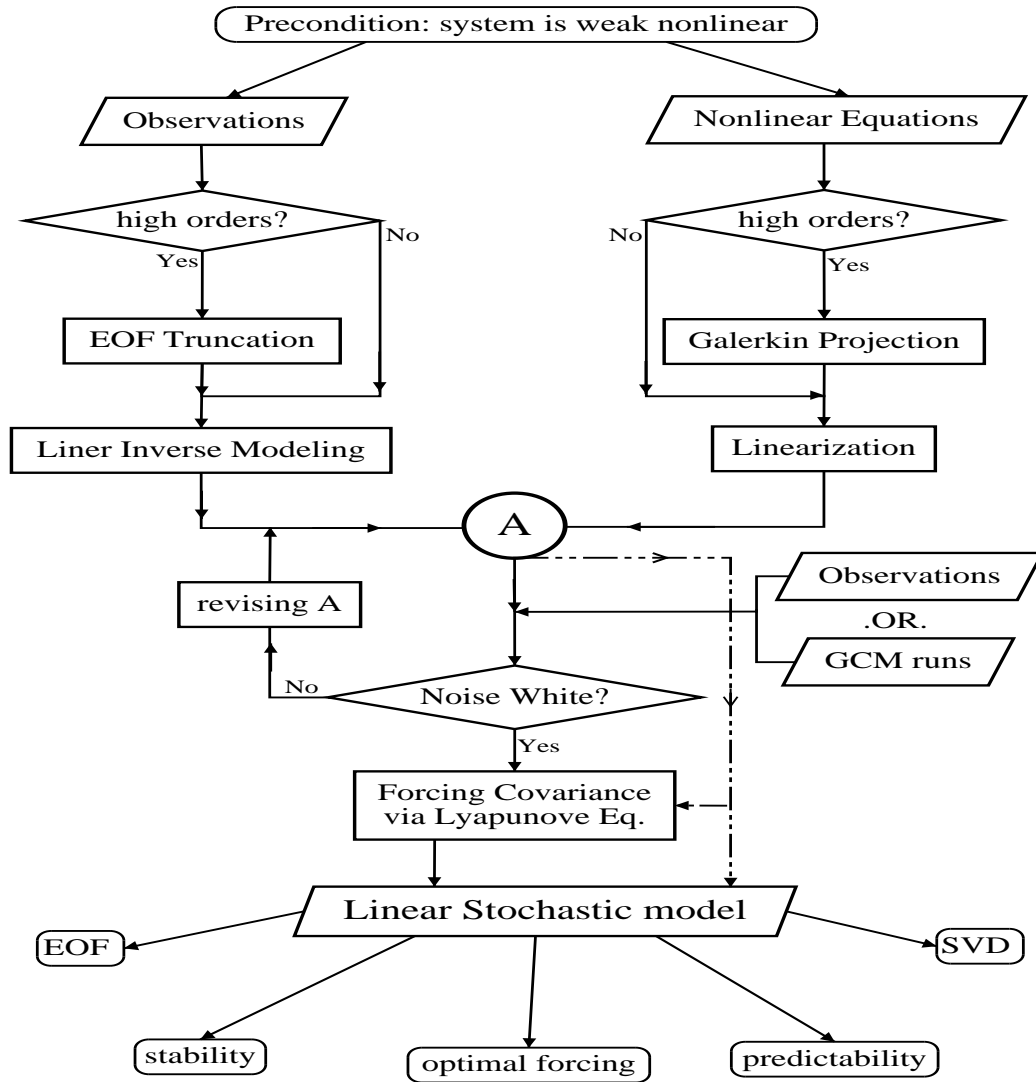


Fig. 4. Flowchart of linear stochastic modeling.

predictability of a dynamical system (see Appendix A for possible solution).

The above building blocks plus model reduction form the backbone of linear stochastic modeling framework. Depending on one's needs, these blocks can be combined to create different tactics. We summarize the main point in a flow chart (Fig. 4).

## CHAPTER III

EFFECT OF OCEANIC ADVECTION ON THE PREDICTABILITY OF  
MIDLATITUDE SST

## A. Introduction

On climate timescales, the day-to-day weather events seem uncorrelated. This leads to the idea of the stochastic climate model: certain slow variables of the climate system, such as SST, can be modeled as a response of the ocean mixed layer to weather fluctuations. By approximating weather fluctuations as a white noise forcing, Hasselmann (1976) proposed a stochastic climate model which is able to explain the red background spectrum of SST

$$\frac{dT}{dt} = -\lambda T + \xi, \quad (3.1)$$

where  $T$  is SST anomaly,  $\lambda$  is the thermal damping of the mixed layer, and  $\xi$  is a white noise. The predictability of climate system (3.1) is given by  $e^{-2\lambda\tau}$ , and thus depends only on the local damping  $\lambda$ . Studies have shown that much of the midlatitude SST variability can be described by this simple stochastic model (Frankignoul and Hasselmann, 1977; Frankignoul, 1985; Manabe and Stouffer, 1996; Czaja and Frankignoul, 2002; Kushnir et al., 2002a; Deser et al., 2003).

A number of recent studies have extended Hasselmann's simple stochastic climate model by including additional physics. For example, Barsugli and Battisti (1998) constructed a simple coupled stochastic model to study the effects of atmosphere-ocean thermal coupling. Their results show that the coupling will enhance the variance by reducing the thermal damping through air-sea feedback. Thus, the predictability of the atmosphere will be enhanced by the coupling, but the predictability of SST is still

governed by the local ocean mixed layer damping (Bretherton and Battisti, 2000). Saravanan and McWilliams (1998) added the advective effect to the Hasselmann model and showed the possibility that a spatial coherent atmospheric white noise forcing can give rise to a decadal mode of variability through a stochastic resonance. The timescale of this mode is determined by the spatial scale of the atmospheric forcing and the velocity of the ocean circulation. If the damping is weak relative to the advective effect, a spectral peak can be detected around that timescale. This has been proposed as one of the potential mechanisms for decadal variation in the climate system. An interesting question arising from the study by Saravanan and McWilliams (1998) is how this decadal mode can potentially affect the prediction of SST. More generally, how does the oceanic advection affect the predictability? Does the existence of a decadal mode necessarily lead to an enhancement of predictability?

The role of oceanic advection in enhancing the predictability of SST has been suggested by a number of recent studies. For example, Sutton and Allen (1997), based on an empirical analysis of observed SST, showed that SST anomaly can be tracked along the Gulf Stream and North Atlantic current system for several years, and thus hinted that the climate of North Atlantic may be predicted several years in advance. A more recent study by Scott (2003) explicitly addressed the effect of oceanic advection on SST predictability from a theoretical perspective. Using an idealized one-dimensional advective stochastic model, Scott showed that the advection can enhance the predictability in certain areas through a so-called stochastic cancellation process, while in other areas the predictability is reduced.

The purpose of this study is to take a further look at the role of oceanic advection in predictability of SST under a more realistic setting, using the tools recently developed for the study of predictability of a linear coupled system (Chang et al., 2003a,b). In Section B, a general advective stochastic model of midlatitude SST anomalies is

formulated, and the magnitude of key parameter is assessed. In Section C, the predictability of an idealized one-dimension model, similar to the one used by Scott (2003), is solved analytically and discussed in a more general context with the aid of Predictable Component Analysis (Schneider and Griffies, 1999). In Section D, a more realistic two-dimensional advective model is derived along with realistic parameters; the predictability of the system is analyzed fully and contrasted to the nonadvective version of the model to obtain a quantitative estimate of the effect of North Atlantic circulation gyres on SST predictability. Finally, in Section E some conclusions of the study are drawn, and their implication to the real climate system is discussed.

#### B. A stochastically forced ocean mixed layer model

In oceanic mixed layer, the first law of thermodynamics takes the form

$$h \frac{\partial T}{\partial t} + h \mathbf{v} \cdot \nabla T + w_e (T - T_h) - \kappa h \nabla^2 T = \frac{Q - Q_h}{\rho C_p} \quad (3.2)$$

where  $T$ ,  $\mathbf{v}$ , and  $h$  denote temperature, velocity, and mixed layer depth;  $T_h$  is the temperature of the lower layer;  $\rho$  and  $C_p$  the water density and specific heat, respectively;  $Q$  the net surface heat flux into the mixed layer *which is the sum of latent heat flux, sensible heat flux, shortwave radiation and longwave radiation*;  $Q_h$  is the heat flux at the bottom of the mixed layer. The diffusivity  $\kappa$  parameterizes the horizontal turbulent mixing. The vertical turbulent mixing at the base of the mixed layer is parameterized by an entrainment velocity  $w_e$

$$w_e \equiv H_{\left(\frac{\partial h}{\partial t} + \nabla \cdot (h \mathbf{v})\right)} \quad (3.3)$$

where  $H_{(x)} = x$  if  $x \geq 0$ ,  $H_{(x)} = 0$  if  $x < 0$ .

Each variable in Eq. (3.2) can be decomposed into two components: climatology

and anomaly. To the first order of approximation, the equation of SST anomalies can be written as

$$\frac{\partial T'}{\partial t} + \bar{\mathbf{v}} \cdot \nabla T' + \frac{T' - T'_h}{\bar{h}} \bar{w}_e - \kappa \nabla^2 T' = \underbrace{\frac{Q'}{\rho C_p \bar{h}}}_A - \underbrace{\mathbf{v}' \cdot \nabla \bar{T}}_B - \underbrace{\frac{h'}{\bar{h}} \bar{\mathbf{v}} \cdot \nabla \bar{T}}_C - \underbrace{\frac{\bar{T} - \bar{T}_h}{\bar{h}} w'_e}_D \quad (3.4)$$

where overbars denote mean fields; primes denote anomalies. For the sake of simplicity, the seasonal cycle is omitted in our model. The terms on the right hand side (RHS) are: anomalous atmospheric forcing via heat flux (A), anomalous currents (B), mixed-layer perturbations (C), and entrainment anomalies (D), respectively (Frankignoul, 1985). Among them, heat flux  $Q'$  is the primary driving force (Cayan, 1992), though anomalous advection also plays a significant role (Latif and Barnett, 1994; Marshall et al., 2001a); both  $C$  and  $D$  are highly correlated with the anomalous winds and may not be negligible (Alexander and Penland, 1996).

In order to close Eq.(3.4), the details of atmosphere-ocean thermodynamic and dynamic coupling should be known. However, in the extratropics the experiments of coupled GCMs show that the main effects of coupling are an increase of climate variance and a decrease of heat flux; it does not alter the large-scale spatial pattern of atmospheric variability (Manabe and Stouffer, 1996; Bladé, 1997; Saravanan, 1998; Seager et al., 2000). This characteristic is approximated well by a local linear air-sea feedback (Barsugli and Battisti, 1998). Therefore, the RHS of Eq.(3.4) could be written as a sum of linear feedback  $-\lambda_a T'$  and atmospheric internal variability  $\mathcal{F}$ , which is independent on SST anomalies by definition. Eq.(3.4) can be greatly simplified as

$$\frac{\partial T'}{\partial t} + \bar{\mathbf{v}} \cdot \nabla T' + \frac{\bar{w}_e}{\bar{h}} (T' - T'_h) - \kappa \nabla^2 T' = \mathcal{F} - \lambda_a T' \quad (3.5)$$

where  $T'_h$  denotes temperature anomaly below the mixed layer. Associated with seasonal shoaling and deepening, water detrains out of or entrains into the mixed layer. This reemergence mechanism effectively reduces the thermal damping and enables SST anomalies to persist longer (Alexander et al., 1999; Watanabe and Kimoto, 2000). Consequently,  $T'_h$  can be approximated as a small fraction of  $T'$  in the sense of annual mean,

$$T'_h \approx \delta T'$$

where  $\delta \approx 0.3$  (Watanabe and Kimoto, 2000). Then, Eq.(3.5) can be written in the familiar form

$$\frac{\partial T'}{\partial t} + (\lambda_a + \lambda_o)T' + \bar{\mathbf{v}} \cdot \nabla T' - \kappa \nabla^2 T' = \mathcal{F} \quad (3.6)$$

where  $\lambda_o = (1 - \delta)\frac{w_e}{h}$ . And  $\lambda_a$  could be negative which means a positive air-sea feedback. Note both  $\lambda_o$  and  $\mathcal{F}$  are inversely proportional to the mean mixed layer depth  $\bar{h}$ .

Dropping the prime and overbar from Eq. (3.6), we write the governing equation as

$$\frac{\partial T}{\partial t} + \lambda T + \mathbf{v} \cdot \nabla T - \kappa \nabla^2 T = \mathcal{F}, \quad (3.7)$$

where  $T$  is the temperature anomaly within the mixed layer,  $\mathbf{v}$  is the mean surface current,  $\kappa$  is the eddy-diffusivity coefficient,  $\lambda = \lambda_o + \lambda_a$  represents a local damping rate determined by the strength of the air-sea feedback and oceanic mixing, and  $\mathcal{F}$  denotes atmospheric stochastic processes that are internal to atmospheric dynamics and independent of SST anomalies.

Parameters of the governing system can be estimated either directly or indirectly from the observation. The parameter taken from the observation is the mean surface current. Other parameters, such as the damping rate  $\lambda$ , can not be estimated from direct observation and must be derived from empirical analysis. The estimation of

the damping rate  $\lambda_a$  is often based on properties of the lag correlation between SST and heat flux anomalies. Frankignoul et al. (1998) estimated that the turbulent heat flux feedback contributes  $20 \text{ W m}^{-2} \text{ K}^{-1}$ . It is equivalent to a negative atmospheric damping  $\lambda_a = \frac{1}{8} \text{ mon}^{-1}$  for a 100 m mixed layer with 1 K temperature anomaly. On the other hand, the oceanic damping rate  $\lambda_o$  is largely determined by subsurface entrainment. And the estimated entrainment rate is typically on the order of  $10^{-5} \text{ m s}^{-1}$  based on regression analysis of the mixed layer temperature (Ostrovskii and Piterbarg, 2000) and kinematic diagnosis of the mixed layer (Marshall et al., 1993; Hazeleger and Drijfhout, 2000). This value leads to an estimation of the oceanic damping rate  $\lambda_o$  to be about  $\frac{1}{4} \text{ mon}^{-1}$ . Thus, a typical time scale of mixed layer damping  $\lambda$  is on the order of 3 months.

The forcing term on the right hand side of Eq. (3.7) is due to atmospheric internal variability. Beyond two weeks, the atmospheric internal variability is unpredictable (Lorenz, 1969, 1984). Therefore,  $\mathcal{F}$  can be treated as white noise in Eq. (3.7). The random atmospheric forcing gives the unpredictable component of the system. Note that even though the atmospheric forcing can be approximated by a white noise process in time, the spatial structure of the forcing is generally coherent. These spatial coherent structures have important implication to the variability and predictability of the coupled system, as will be illustrated in Section C and Section D.

### C. Analytical solution to 1D advective model

To begin our exploration of advective effects on predictability, it is instructive to first consider a simple 1D model for which an analytical solution can be obtained. A similar solution was presented by Scott (2003), but in this study we discuss the solution in a somewhat different perspective with the aid of PrCA analysis. Assuming

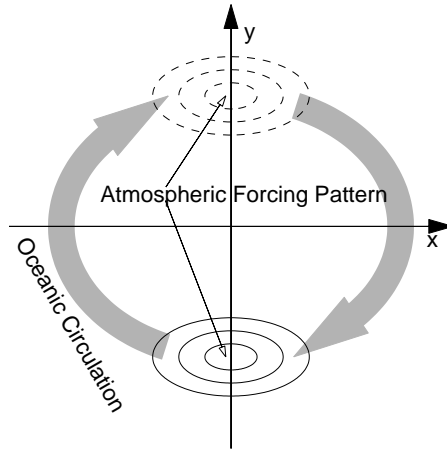


Fig. 5. Schematic sketch of oceanic gyre and atmospheric forcing. The characteristic velocity of the gyre is  $U$ . The atmospheric forcing, although random in time, has a spatially fixed structure of characteristic length  $L$ . Together, they give a characteristic timescale  $L/U$ .

a uniform oceanic current and a dipole atmosphere forcing (see Fig. 5), we formulate a one-dimensional version of (3.7) as

$$\frac{\partial T}{\partial t} + \lambda T + U \frac{\partial T}{\partial x} - \kappa \frac{\partial^2 T}{\partial x^2} = f_0 \sin\left(\frac{2\pi x}{L}\right) \xi, \quad (3.8)$$

where  $U$  and  $L$  are the characteristic velocity and length scale of ocean circulation,  $f_0$  is the magnitude of atmospheric forcing, and  $\xi$  is the standard white noise. For simplicity, we assume a periodic boundary condition which is, strictly speaking, unrealistic because in the real ocean the water parcels, instead of being advected around a gyre in the surface layer, are subducted into the subsurface. This issue is discussed in Saravanan and McWilliams (1998). This boundary condition, however, will not fundamentally alter the results of this study.



### 1. Solving the 1D model

In the absence of forcing, (3.8) supports a set of normal modes given by

$$\psi_m = \exp(-\alpha_m t) \left( \sin(\beta_m (\frac{x}{U} - t)), \cos(\beta_m (\frac{x}{U} - t)) \right), \quad m = 0, 1, \dots \quad (3.9)$$

where eigenvalues  $\alpha_m = \lambda + \kappa(2m\pi)^2/(L)^2$  and  $\beta_m = 2m\pi U/L$  are the damping rate and frequency of the normal modes. These normal modes describe a series of damped traveling waves with different zonal scales, which have the same propagating speed determined by the characteristic velocity  $U$ .

Usually we will not see all these normal modes because the response depends on the excitation from external forcing. If the spatial scale of the forcing is large, only the normal modes with large spatial scale will be excited. In particular, if the forcing structure resembles the structure of one of the normal modes, as we assumed in this study, then a resonance occurs despite the fact that the forcing is random in time. The resonant response has a stationary structure with a time scale determined by the spatial scale divided by the advective speed. Saravanan and McWilliams (1998) proposed that this resonance may be regarded as one of the mechanisms for the generation of low-frequency variations in the ocean. The forced solution of (3.8) clearly exhibits such property.

Assuming  $T$  to evolve long enough to lose the memory of the initial condition, only the specific solution of Eq. (3.8) would be left

$$T(x, t) = a(t) \sin(\frac{2\pi x}{L}) + b(t) \cos(\frac{2\pi x}{L}), \quad (3.10)$$

where  $a(t)$  and  $b(t)$  are stochastic processes driven by white noise  $\xi(t)$ . Generally, they are not white due to the integrating effect of the oceanic mixed layer. Substituting Eq. (3.10) into Eq. (3.8) gives the solutions of  $a(t)$  and  $b(t)$ . This can be done in

spectral space via Fourier transform

$$\mathcal{T}(x, \omega) = f_0 \frac{\mathcal{W}(\omega)}{(\alpha + i\omega)^2 + \beta^2} \left[ (\alpha + i\omega) \sin\left(\frac{2\pi x}{L}\right) - \beta \cos\left(\frac{2\pi x}{L}\right) \right], \quad (3.11)$$

where  $\alpha$  and  $\beta$  are  $\alpha_1$  and  $\beta_1$  in Eq. (3.9),  $\mathcal{W}(\omega)$  is the Fourier transform of white noise  $\xi(t)$ , and  $i = \sqrt{-1}$ .

The predictable signal is the evolution of initial condition under the reduced homogeneous equation (3.8), which is essentially an initial value problem. The solution

$$\begin{aligned} \hat{T}(x, t_0 + \tau) &= e^{-\alpha\tau} \left[ a_{(t_0)} \sin\left(\frac{2\pi x}{L} - \beta\tau\right) + b_{(t_0)} \cos\left(\frac{2\pi x}{L} - \beta\tau\right) \right] \\ &= e^{-\alpha\tau} T(x - U\tau, t_0) \end{aligned} \quad (3.12)$$

shows how to make a prediction— using upstream information predicts downstream area. After some mathematical manipulation and tedious Fourier inverse transform, its covariance function can be written as

$$\begin{aligned} \mathbf{C}(x_1, x_2; \tau) &= \frac{f_0^2}{4\alpha} \exp(-2\alpha\tau) \left( \sin\left(\frac{2\pi x_1}{L} - \beta\tau\right) \sin\left(\frac{2\pi x_2}{L} - \beta\tau\right) \right. \\ &\quad \left. + \sin\left(\frac{2\pi x_1}{L} - \beta\tau - \theta\right) \sin\left(\frac{2\pi x_2}{L} - \beta\tau - \theta\right) \right), \end{aligned} \quad (3.13)$$

where  $\theta = \arctan(\beta/\alpha)$  is the rotational angle. The eigenfunctions of  $\mathbf{C}(x_1, x_2; 0)$  are the EOFs. And the projection of  $\mathcal{T}(x, \omega)$  onto these EOFs gives the corresponding spectra.

For the linear system, the total response is signal plus noise, i.e.  $\mathbf{C} = \mathbf{E}_\tau + \mathbf{C}_\tau$ . Therefore, the predictability is given by

$$\epsilon(\tau) = 1 - \frac{\int_0^L \mathbf{C}(x, x; \tau) dx}{\int_0^L \mathbf{C}(x, x; 0) dx}, \quad (3.14)$$

and the predictable patterns are defined through the generalized eigen problem

$$\int_0^L \mathbf{q}(\tau, x') \mathbf{C}(x, x'; \tau) dx' = \gamma(\tau) \int_0^L \mathbf{q}(\tau, x') \mathbf{C}(x, x'; 0) dx', \quad (3.15)$$

where  $\mathbf{q}$  is the filter, and  $\mathbf{p} = \int \mathbf{q} \mathbf{C}(x, x'; 0) dx'$  is the predictable pattern with skill  $\varepsilon = 1 - \gamma$ .

In our problem, the response is confined in the space spanned by  $\sin(\frac{2\pi x}{L})$  and  $\cos(\frac{2\pi x}{L})$ , so are the  $\mathbf{p}$  and  $\mathbf{q}$

$$\begin{aligned}\mathbf{q}_{1,2} &= \sin\left(\frac{2\pi x}{L} + \phi_{1,2}\right) \\ \mathbf{p}_{1,2} &= \sin\left(\frac{2\pi x}{L} + \varphi_{1,2}\right).\end{aligned}\tag{3.16}$$

Eq. (3.15) gives the relationships for the phase angle  $\phi_{1,2}$

$$\cos \theta \cos(\beta\tau) + \cos(\beta\tau + \theta + 2\phi) = 0\tag{3.17}$$

and skill  $\gamma$ . Finally,  $\mathbf{p}$  is found by using the orthogonality property of the generalized eigenvectors,  $\mathbf{p}_1 \perp \mathbf{q}_2$  and  $\mathbf{p}_2 \perp \mathbf{q}_1$ , which gives  $\varphi_{1,2}(\tau) = \phi_{2,1} - \frac{\pi}{2}$ .

## 2. Variance analysis

The solution (3.11) can be conveniently expressed as a sum of EOFs which are the eigenfunctions of covariance matrix  $\mathbf{C}$  (3.13). For the problem at hand,  $\mathbf{C}$  is singular with only two nonzero eigenvalues. The response  $T$  can be described completely by the two EOFs and the associated Principal Component (PC) time series. These EOFs (Fig. 6) and the spectra of their PC time series are given by:

$$\begin{aligned}\text{1st EOF} & \quad \sin\left(\frac{2\pi x}{L} - \frac{\theta}{2}\right), \\ \text{Spectrum} & \quad \frac{f_0^2 L}{4} \left( \frac{1}{(\omega - \beta)^2 + \alpha^2} + \frac{1}{(\omega + \beta)^2 + \alpha^2} \right) \cos^2\left(\frac{\theta}{2}\right), \\ \text{2nd EOF} & \quad \cos\left(\frac{2\pi x}{L} - \frac{\theta}{2}\right), \\ \text{Spectrum} & \quad \frac{f_0^2 L}{4} \left( \frac{1}{(\omega - \beta)^2 + \alpha^2} + \frac{1}{(\omega + \beta)^2 + \alpha^2} \right) \sin^2\left(\frac{\theta}{2}\right),\end{aligned}\tag{3.18}$$

where the phase angle  $\theta = \arctan(\beta/\alpha)$  gives a measure of downstream shift of the location of the maximum response relative to the maximum forcing. The shift is determined by the relative importance of the advective effect to the damping effect. In the absence of advection, the location of the maximum response, as expected, coincides the location of the maximum forcing. The total energy excited by a white noise is given by  $f_0^2 L / (4\alpha)$  and is independent of the advection. Of the total energy, EOF 1 and EOF 2 contribute  $\cos^2(\theta/2)$  and  $\sin^2(\theta/2)$ , respectively. Without advection ( $\mathbf{v} = 0$ ), the oceanic response is a direct footprint of atmospheric forcing ( $\theta = 0$ ), and all the energy is contained in EOF 1. Therefore, the advection effect causes the system to partition its total energy onto two uncorrelated components. The center of action of each components shifts downstream relative to the maximum forcing location (Fig. 6) even though the total energy remains unchanged.

Since the energy of the system is represented by two uncorrelated components, the total power spectral density is equal to the sum of the two power spectral density functions associated with the two EOFs,

$$S_{(\omega)} = \frac{\alpha}{(\omega - \beta)^2 + \alpha^2} + \frac{\alpha}{(\omega + \beta)^2 + \alpha^2}. \quad (3.19)$$

The spectrum has pronounced peaks only when the advection effect is sufficiently stronger than the damping effect, i.e.  $\beta > \frac{\sqrt{3}}{3}\alpha$ . When this happens, the system can be said to have a strong resonant response to the stochastic forcing, although the period of the response is usually longer than the period of the normal modes. This finding is consistent with result of Saravanan and McWilliams (1998). In their study, the ocean-atmosphere system shows a preferred timescale only in the so-called *fast/deep* regime, i.e. current is strong and mixed layer is deep. This parameter regime is equivalent to large  $\beta$  and small  $\alpha$  in our solution. The autocorrelation is the inverse

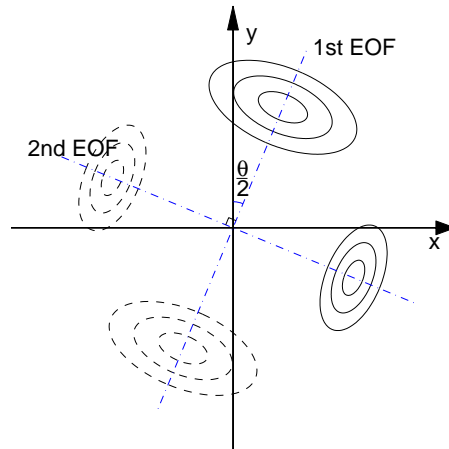


Fig. 6. Schematic drawing of SST EOFs in the 1D system. First EOF, denoted by big ellipses, counts  $\cos^2(\theta/2)$  of total variance; while second EOF, represented by small ellipses, contributes  $\sin^2(\theta/2)$ . The spatial structure is inherit from the coherent forcing. The phase angle  $\theta$  ( $0 \leq \theta < \pi/2$ ) is determined by the advection of the oceanic gyre. The stronger the current, the larger the downstream shift.

Fourier transform of power spectrum,  $\rho(\tau) = \mathfrak{F}^{-1} [S(\omega)] = \exp(-\alpha\tau) \cos(\beta\tau)$ . This is consistent with our physical intuition that advection enhances the local damping effect by moving the anomaly away from its initial location, making it less persistent.

### 3. Predictability analysis

Like the total variance, the normalized error variance of the optimal prediction defined by (3.14),

$$\epsilon(\tau) = 1 - \exp(-2\alpha\tau), \quad (3.20)$$

is also independent of advection and solely determined by the damping and diffusion time scale. Scott (2003) analyzed the normalized error variance at every grid point  $x$  and showed that the predictability in certain areas can be enhanced due to stochastic cancellation. Here, we take an alternative approach to analyze the heterogeneity of predictable variance based on PrCA analysis.

As shown in the previous section, PrCA requires solving a generalized eigenvalue problem. Since the covariance function  $\mathbf{C}$  has only two nonzero eigenfunctions, the generalized eigenvalue problem can be solved in the  $2 \times 2$  eigenfunction space (3.16). The resulting predictable patterns are

$$\mathbf{p}_{1,2}(\tau) = \cos\left(\frac{2\pi x}{L} + \phi_{2,1}\right),$$

where  $\phi_{1,2}(\tau) = \pm 0.5(\arccos(-\cos\theta \cos(\beta\tau)) - \beta\tau - \theta)$  is given by (3.17). The skill or predictability associated with predictable pattern is given by the corresponding eigenvalue which represents the normalized prediction error growth of the projection time series onto the filter pattern  $\mathbf{q}_{1,2}$ ,

$$\varepsilon_{1,2}(\tau) = 1 - \left(\frac{2 + 2\cos\theta \cos(2\phi_{2,1} + \theta)}{\sin^2\theta} - 1\right) \exp(-2\alpha\tau). \quad (3.21)$$

Clearly, at a given lead time the most predictable pattern corresponds to the smallest  $\varepsilon$  while the least predictable pattern corresponds to the largest  $\varepsilon$ .

To gain understanding of these patterns, it is instructive to consider first the case of small lead time, i.e.  $\tau \rightarrow 0$ . In this case,  $\varphi_1 \rightarrow 0$ ,  $\varphi_2 \rightarrow -\theta$ , and  $\varepsilon_2 < \varepsilon_1$ . This means that  $\mathbf{p}_2$  is the most predictable pattern, and  $\mathbf{p}_1$  is the least predictable pattern. Therefore, at short lead times the center of action of the most predictable pattern  $\mathbf{p}_2$  is further downstream of the leading EOF, and is located in-between the maximal loading of the first EOF and the minimal noise forcing. A simple explanation for the structure of this pattern can be put forward as follows: Since the absolute prediction error is determined by the noise forcing, the large (small) error growth is expected to occur near the maximal (minimal) forcing region. Furthermore, since the predictability is measured not simply by the absolute error growth but by the *normalized* error, the structure of the most predictable pattern must also depend on the location of the maximum variance in the system (given by the leading EOF). The

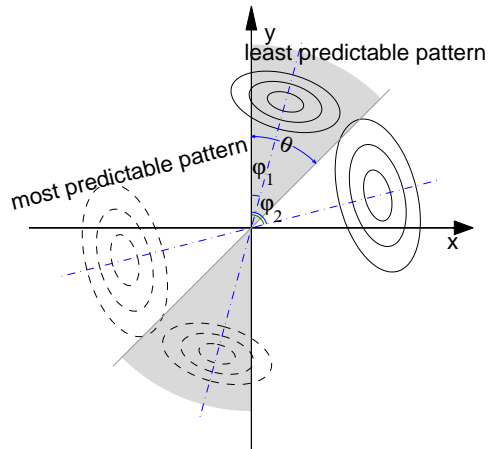


Fig. 7. Most and least predictable patterns of the simple 1D model. Bigger ellipses denote most predictable pattern, smaller ellipses the least predictable pattern. Their downstream shift, compared with the forcing (Fig. 5), are  $\varphi_1$  and  $\varphi_2$ , respectively. The centers of the least predictable pattern are confined to the shaded areas, and the centers of the most predictable pattern are in the blank area. Note both  $\varphi_1$  and  $\varphi_2$  depend on lead time  $\tau$ , and  $\varphi_2 - \varphi_1 \neq \pi/2$ .

pattern that maximizes the ratio between the two, therefore, should locate somewhere in between the regions of the minimal noise forcing and maximal variance.

As lead time  $\tau$  increases, advective effect comes into play, and the pattern of error growth is determined by the sum of the noise forcing at each  $t \in (0, \tau)$  transported by the current  $U$ . Each of the transformed noise forcing represents a damped response shifted downstream by the advective effect during initial time  $t = 0$  to  $t \in (0, \tau)$ . The sum represents an average of the system's response to noise forcing. It is expected that the resultant maximal error growth takes place downstream of the location of maximal noise forcing. Consequently, the most predictable variance also shifts further downstream relative to its initial location. Fig. 7 depicts the structures of the most and least predictable pattern at a given lead time. It is worth emphasizing that the structure of the noise forcing plays an important role in determining the structure of the predictable variance. If the noise forcing is white in space, then the predictable

patterns will be determined solely by the variance structure of the system at short lead times. In this case, the most predictable pattern simply coincides with the leading EOF at very short lead time, as shown by Chang et al. (2003a). In general, the predictable patterns differ from the EOFs. The latter is subject to the spatial orthogonality constraint while the former generally is not.

In the absence of advection,  $\varphi_1 = \varphi_2 = 0$  and  $\varepsilon_1 = \varepsilon_2 = 1 - \exp(-2\alpha\tau)$ . This means that the predictable variance is spatially uniform with normalized error given by  $\epsilon = 1 - \exp(-2\alpha\tau)$  everywhere. This is because without advection the maximal forcing and maximal variance co-locate and tend to cancel out each other, giving no special preference for the predictable variance. The system degenerates to Hasselmann’s zero-dimensional model.

Special attention should be paid to the interpretation of our results here. Although the predictability of atmosphere-ocean systems with and without advection are the same, we are not saying that the ocean circulation is trivial in climate modeling. As far as prediction error is concerned, excluding advection would deteriorate the performance of a forecast model. For the idealized stochastic climate system (3.7), the error of persistence prediction (specifying SST for atmospheric GCM)

$$\epsilon_{\text{persist}} = \frac{\text{Var}(T_{t_0+\tau} - T_{t_0})}{\text{Var}(T_{t_0})} = 2(1 - \rho_\tau) = 2 - 2\exp(-\alpha\tau)\cos(\beta\tau)$$

and the error of damped persistence prediction (couple slab ocean to atmosphere)

$$\epsilon_{\text{dpp}} = \frac{\text{Var}(T_{t_0+\tau} - \exp(-\alpha_1\tau)T_{t_0})}{\text{Var}(T_{t_0})} = 1 + \exp(-2\alpha\tau)[1 - 2\cos(\beta\tau)]$$

are larger than that of optimal prediction—predictability,  $\epsilon_{\text{persist}}^2 > \epsilon_{\text{dpp}}^2 > \epsilon^2$ .

However, one can argue conversely: since the predictability is determined by damping and mixing, not the advection, as long as the ocean model contains a realistic mixing scheme, it will capture most of the climate predictability (at least for seasonal



prediction). In fact, if the current is weak  $\beta \leq \alpha$ , damped persistence prediction gives pretty good forecasting of SST, i.e.  $\epsilon_{\text{persist}} \gg \epsilon_{\text{dpp}} \asymp \epsilon$ . Numerical experiments with slab-ocean mixed layer model confirm this statement (Manabe and Stouffer, 1996). Of course one exception is the strong current area, such as the western boundary of Atlantic ocean, where a good prediction model of SST needs to resolve the western boundary current.

#### 4. An example with realistic parameters

Let us consider a basin-scale noise forcing acting on an ocean with advective speed of  $U = 0.05 \text{ m s}^{-1}$ , basin size of  $L = 1 \times 10^7 \text{ m}$ , local thermal damping of  $\lambda = \frac{1}{3} \text{ mon}^{-1}$ , and eddy diffusivity of  $\kappa = 1 \times 10^4 \text{ m}^2 \text{ s}^{-1}$ . With these parameters, the one-dimensional system supports a severely damped normal mode with a period of approximately 6.5 years. The power spectrum and predictability are shown in Figs. 8 and 9.

Compared to the case without advection, there is a small shift of energy towards the high frequency by the advection, as indicated by the spectral analysis (Fig. 8), so that the overall spectrum is flatter than the red spectrum ( $U = 0$ ). Since the damping effect is much stronger in comparison to the advective effect, no spectral peak is observed. This corresponds to the *slow/shallow* regime of Saravanan and McWilliams (1998).

Although the advection has an impact on the energy spectrum of the system, the normalized prediction error variance integrated over the domain turns out to be identical with and without advection, which is depicted by the solid line in Fig. 9. Using  $\epsilon = 0.5$  as a threshold for predictability limit, the simple model's forecast skill is limited to about one month. In the absence of advection, this also presents the model's skill at each grid point. Because the skill is the same everywhere in the domain,

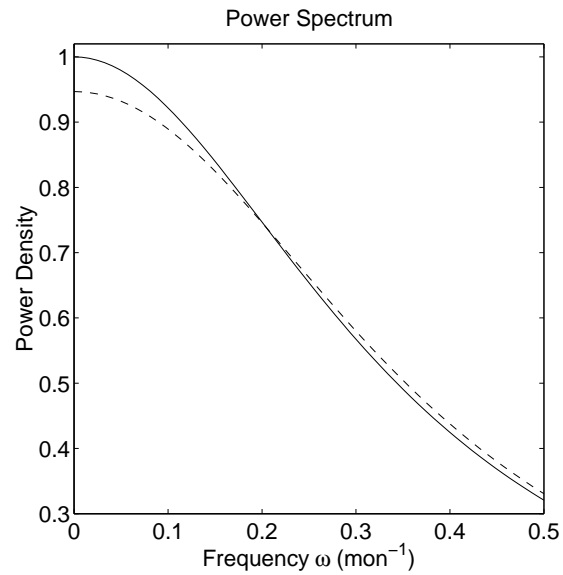


Fig. 8. Power spectrum of the 1D climate system with realistic parameters. The solid line is the spectrum without advection; the dashed line is with advection. Note the integrals of both, which represent the total energy, are the same.

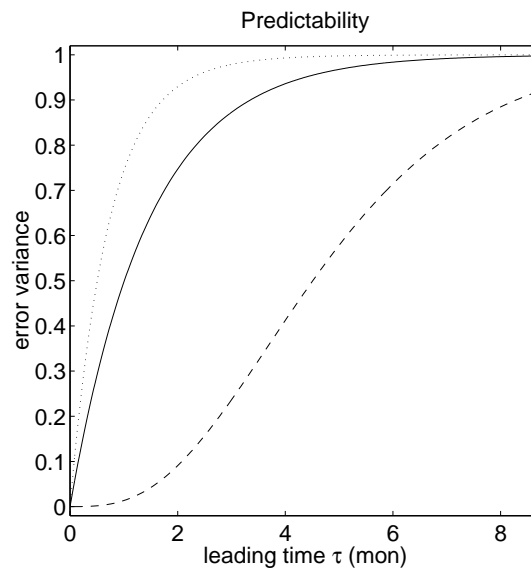


Fig. 9. Predictability of 1D advective ocean. Solid line, domain averaged error variance; dashed line, skill of most predictable pattern; dotted line, skill of least predictable pattern. The useful skill is defined as  $\leq 0.5$ .

there is no special region where the predictability is enhanced. However, when the advection effect is included, at a given lead time the prediction error of the system can be decomposed into two spatial patterns — one (the most predictable pattern) with the smallest normalized error variance and the other (the least predictable pattern) with the largest normalized error variance. The error growth along the direction of the most (least) predictable pattern is shown as dashed (dotted) line in Fig. 9. The lead time corresponding to  $\varepsilon = 0.5$  is 4.5 months along the direction of the most predictable pattern while it is only 0.5 month along the least predictable pattern. Therefore the system is expected to have better predictability when initial conditions bear a close resemblance to the most predictable pattern.

### 5. A general white noise forcing

When the eigenfunctions of the stochastic forcing have the same patterns as the normal modes of Eq 3.7, then the forcing can be expressed as a series

$$\mathcal{F} = \sum_{n=0}^{\infty} f_n \sin\left(\frac{2n\pi x}{L}\right) + g_n \cos\left(\frac{2n\pi x}{L}\right); \quad n = 0, 1, \dots \quad (3.22)$$

where the time coefficients  $f_n$  and  $g_n$  are independent and white. By the superposition principle, many results will follow directly. For example, the total variance

$$\sigma^2(T') = \frac{L}{4} \sum \frac{\sigma_{f_n}^2 + \sigma_{g_n}^2}{\alpha_n} \quad (3.23)$$

is independent of advection.

The total power spectral density function is

$$S_{(\omega)} = \sum \frac{(\sigma_{f_n}^2 + \sigma_{g_n}^2)L}{4} \left( \frac{1}{(\omega - \beta_n)^2 + \alpha_n^2} + \frac{1}{(\omega + \beta_n)^2 + \alpha_n^2} \right). \quad (3.24)$$

The autocorrelation is

$$\rho(\tau) = \frac{\sum \frac{\sigma_{f_n}^2 + \sigma_{g_n}^2}{\alpha_n} \cos(\beta_n \tau) \exp(-\alpha_n \tau)}{\sum \frac{\sigma_{f_n}^2 + \sigma_{g_n}^2}{\alpha_n}}. \quad (3.25)$$

Finally, the normalized signal variance is

$$\chi_{(\tau)}^2 = \frac{\sum \frac{\sigma_{f_n}^2 + \sigma_{g_n}^2}{\alpha_n} \exp(-2\alpha_n \tau)}{\sum \frac{\sigma_{f_n}^2 + \sigma_{g_n}^2}{\alpha_n}}. \quad (3.26)$$

So even with more general forcing, the independence of total energy and total normalized error variance with advection still holds.

A special case in this category is the spatial white noise, i.e.  $\sigma_{f_n} = \sigma_{g_n} = 1$ . Then the total variance is  $\sigma^2(T') = \frac{L}{4} \left( \frac{1}{\lambda} + \frac{L}{2\sqrt{\lambda\kappa}} \coth\left(\frac{L}{2} \sqrt{\frac{\lambda}{\kappa}}\right) \right)$ . And its predictability has an upper bound,  $\chi_{(\tau)}^2 < e^{-2\lambda\tau}$ . In fact, if only short range prediction is of concern, any coherent stochastic forcing would give more predictability than the spatial white noise (compare their Taylor expansion around  $\tau = 0$ ). Furthermore, its normal modes, EOFs, and predictable patterns are the same—a complete set of orthonormal functions  $\{\sin \frac{2n\pi x}{L}; \cos \frac{2n\pi x}{L}\}$  on interval  $[0, L]$ . The variance and predictability associated with these patterns are  $1/(2\alpha_n)$  and  $\exp(-2\alpha_n)$ , respectively. This is a degenerate case because the presence of advection makes no difference in any characteristics. For advection to take effect, some heterogeneity has to be introduced into the model, either through  $\lambda$  or through  $\mathcal{F}$ . In this study, the main concern is the coherent structure of the atmospheric forcing.

Throughout our discussion, the diffusion (second order) is treated as damping (zeroth order),  $\alpha_n = \lambda + \kappa n^2$  (the length scale has been incorporated into  $\kappa$ ). One tends to ask what is the special role of high-order mixing. In addition to mathematical and numerical considerations, a deep physical implication can be argued as following: due to diffusion, the energy is nonuniformly distributing along EOFs even though the

forcing has no preferred spatial scale. The first EOF explains  $1/\lambda$ , the second explains  $1/(\lambda + \kappa)$ , and the third explains  $1/(\lambda + 4\kappa)$ , etc.. In analogy to Hasselmann’s model Eq. (3.1), which provides a simple explanation of red spectrum in climate, diffusion might be one, probably an oversimplified one, of many possible mechanisms generating *spatial redness* of climate—large patterns dominate. Just like all stochastic climate models, the difficulty is to identify the one that operates in the real world, stochastic theory or deterministic (for example, baroclinic instability) theory.

#### D. Predictability of North Atlantic SST

The analytical result in the previous section is useful to shed light on the effect of advection on predictability. In this section, we apply this analysis to a more realistic model. The model is a two-dimensional mixed layer model for the North Atlantic with realistic currents, forcing structure and coastal geometry. Before proceeding to the predictability analysis, we first give a brief outline of the procedure to estimate the unknown parameters and atmospheric forcing from the observational data sets.

##### 1. Parameter estimation

The parameters to be determined are the damping rate  $\lambda$ , advection velocity  $\mathbf{v}$ , eddy diffusivity coefficient  $\kappa$ , and covariance of atmospheric forcing  $\Sigma(x_1, x_2) = E[\mathcal{F}(x_1)\mathcal{F}(x_2)]$ . Several studies discussed the estimation of these parameters using various approaches. Herterich and Hasselmann (1987) compared the spectra of modeled SST according to Eq. (3.7) to those of observed SST anomalies and found that the fit between the computed and observed spectra was successively improved when the advective term was included. The inclusion of eddy diffusive effect, on the other hand, did not have a significant impact on the fit. They further showed that the

inferred parameters from the spectrum fitting are generally in agreement with the direct measurements. Using an autoregressive (AR) model, Ostrovskii and Piterbarg (2000) demonstrated that adding entrainment in the estimation further enhanced the performance of the AR model. However, they cautioned that the model improvement due to the inclusion of more adjustable parameters could be, to a certain extent, offset by a decrease of significant level in the estimation. Therefore in this study we use direct measurements whenever possible. Specifically, the mean current estimation was taken from the gridded Data Set Atlas for Oceanographic Modeling compiled by Samuels and Cox (1987), which is based on ship drift observations. Since Hertwich and Hasselmann (1987) showed that the response of (3.7) was not particularly sensitive to the eddy diffusivity parameter, we simply set it to a constant value of  $\kappa = 1 \times 10^4 \text{ m}^2 \text{ s}^{-1}$ , as commonly used in a coarse resolution ocean circulation model. The two remaining parameters, the damping coefficient and atmospheric forcing, are estimated via the least squares method.

We first cast (3.7) into a finite difference form which contains the two unknown parameters. At each geographical location, the governing equation can be written as

$$\Phi = -\lambda T + \mathcal{F},$$

where  $\lambda$  is the unknown damping parameter,  $\mathcal{F}$  is the unknown noise forcing; and  $\Phi$  represents the sum of all the terms on the left hand side of (3.7) except the damping term. Each of the terms in  $\Phi$ , i.e. the tendency term, the advective term, and diffusion, can be estimated from observed SST, provided that the velocity  $\mathbf{v}$  and eddy diffusivity  $\kappa$  are given. In this study, we used COADS monthly SST from 1945-1992 for the estimations. If  $\mathcal{F}$  is white, then  $T$  and  $\mathcal{F}$  are uncorrelated. The least

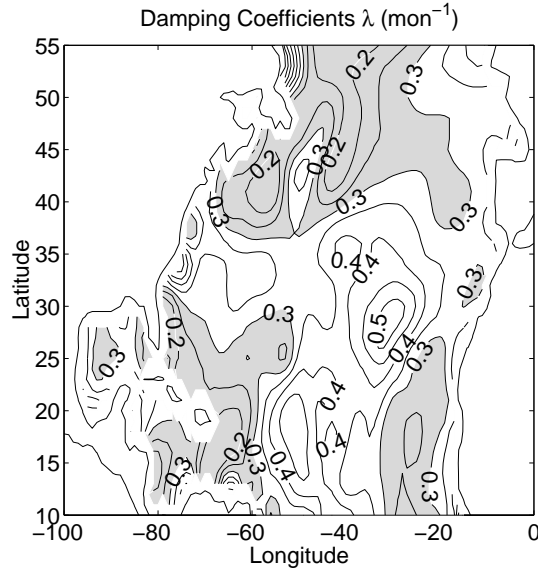


Fig. 10. Estimated damping rate of SST in North Atlantic. The contour interval is 0.05, the unit  $\text{mon}^{-1}$ . Weak damping regions ( $\lambda < 0.3\text{mon}^{-1}$ ) are shaded.

squares method gives the estimator of  $\lambda$  in terms of second momentums

$$\lambda(x) = -\frac{E[\Phi(x) T(x)]}{E[T(x) T(x)]}.$$

Once  $\lambda$  is determined, the residual between  $\Phi$  and  $\lambda T$  gives an estimation of the white noise forcing  $\mathcal{F}$  at this location. The covariance matrix of the forcing can be obtained by an ensemble average over the sampling period. An eigen-decomposition of the forcing covariance gives the leading EOF of the noise forcing which characterizes the dominant spatial structure.

The estimated damping coefficient and atmospheric forcing structure are presented in Figs. 10 and 11. Over much of the North Atlantic the damping time scale is around 3 months, which is consistent with previous studies (Herterich and Hasselmann, 1987; Marshall et al., 1993; Frankignoul et al., 1998; Ostrovskii and Piterbarg, 2000). Three regions of weak damping (with time scale 4~5 months) can be identified: the high latitude Northwestern Atlantic (above 40°N), the Caribbean sea, and off the

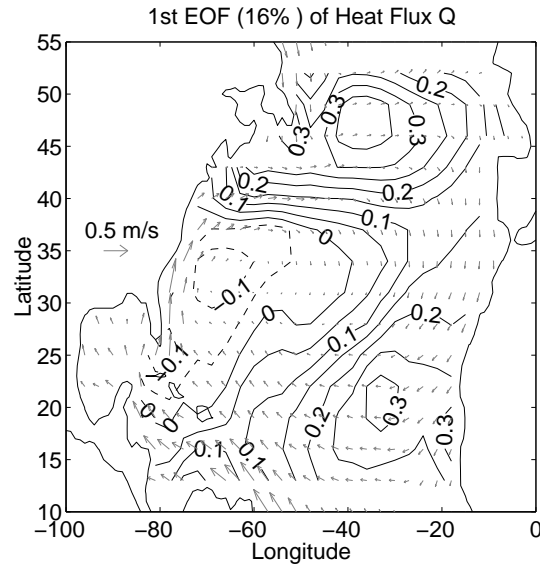


Fig. 11. First EOF of the estimated atmosphere white noise forcing. The background is the velocity field from Data Set Atlas for Oceanographic modeling.

coast of west Africa. While the relatively long damping time scale in the high latitude Northwestern Atlantic region can be attributed to the deeper mixed layer, the weak atmospheric damping in the air-sea exchange of the subtropics may be responsible for the long damping time scale in the other two regions.

The first EOF of estimated atmospheric forcing, a triple-pole structure, resembles the typical pattern associated with the North Atlantic Oscillation (NAO). It explains 16% of the total noise forcing variance. The second EOF (not shown), which accounts for about 13% of the variance, is a dipole-like structure. This finding is consistent with previous studies that based on empirically estimated surface heat fluxes (Wallace et al., 1990; Cayan, 1992), thereby lending support to our statistical estimation.

## 2. Normal modes and EOFs of SST

Once the parameters of the 2D model are determined, a stability analysis is then readily applied to identify the dominant normal modes that affect the predictable



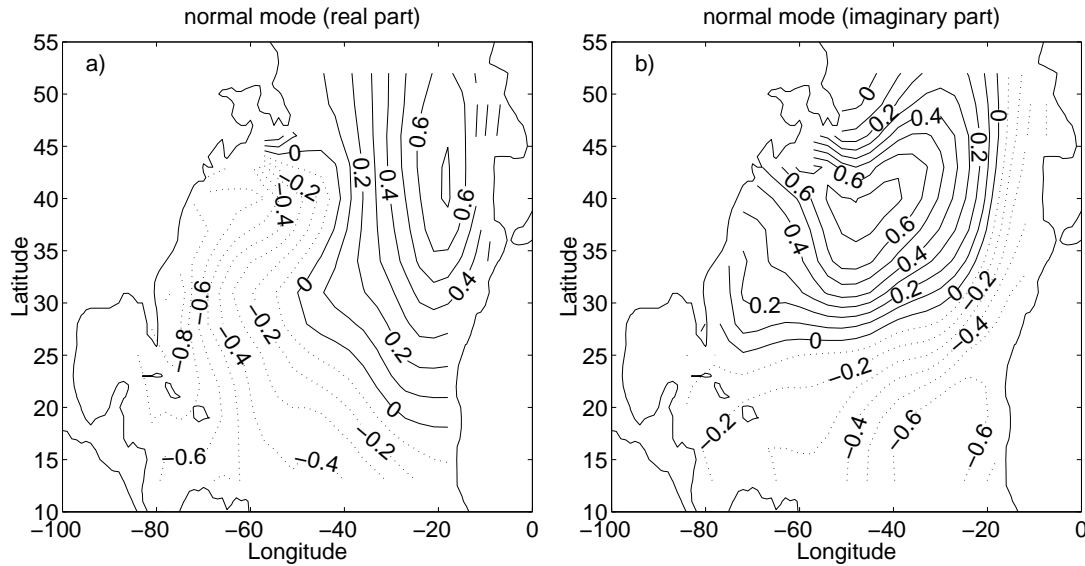


Fig. 12. The normal mode of advective ocean. a) The real part; b) the imaginary part of the eigenvector of linear operator in Eq. (3.7). They constitute a rotary amphidromic wave with a period of 6 years.

dynamics of the system. The normal modes of the system are the eigenvectors of the dynamical operator  $A$ , which can be arranged in the descending order of the real part of the eigenvalues (the damping rate). For the problem at hand, the two least damped normal modes have comparable damping rates of  $0.31 \text{ mon}^{-1}$  and  $0.33 \text{ mon}^{-1}$ . The first one (not shown) is a purely damped mode, while the second one (Fig. 12) represents a pair of severely damped oscillatory modes, which form a rotary wave. The period of the propagating mode is determined by the time that it takes to advect the temperature anomaly around the ocean basin by the subtropical gyre, which is about 6 years. In the simple 1D case where the spatial structure of the forcing is assumed to be the same as that of the advective normal mode, we show that the EOFs of the resonant response have the same spatial structure. This result can not be easily generalized to the more realistic case where the forcing structure does not take the structure of a particular normal mode. The response in this case does not

necessarily resemble any of the individual normal modes even when resonance takes place, but it can consist of several normal modes on which the forcing projects.

Knowing both deterministic dynamics and external forcing allows us to calculate the covariance matrix of SST according to the fluctuation-dissipation theorem (2.9), hence the EOFs of SST. This theorem gives a relationship between the covariance of SST  $\mathbf{C}$ , the dynamical operator  $\mathbf{A}$ , and the forcing covariance  $\mathbf{\Sigma}$ . This relationship hints that the EOFs of the response may be close to the EOFs of the noise forcing for a certain dynamical operator  $\mathbf{A}$ . To explore this further, let us first consider the non-advective case where  $\mathbf{v} = 0$ , and the system degenerates to the simple Hasselmann model. The system matrix  $\mathbf{A}$  in this case reduces to a diagonal matrix with each of its diagonal elements representing the damping rate at one geographic location. If the damping rate does not vary considerably from location to location, then it is readily shown that the EOFs of the SST response will be similar to the EOFs of the forcing. In the case that advection is present,  $\mathbf{A}$  is no longer diagonal and the EOFs of the response in principle could depart from those of the forcing. However, if the advective effect is sufficiently weak compared to the damping effect, one expects the leading EOFs of the SST to bear a resemblance to the dominant EOFs of the forcing. Indeed, for the chosen parameters, we found that the leading EOFs of SST (not shown) and forcing show similar structure, suggesting that in a realistic setting, the advective effect is sufficiently weak so that the dominant response is largely determined by the forcing, as in the simple Hasselmann model.

A further examination of the PC time series indicates a red spectrum with no significant spectral peaks at non-zero frequency (not shown). Compared to the case of no advection, there is a shift of energy towards the high frequency by the advection, as in the 1D case. Such deviation from the AR(1) model (red spectrum) is also a robust feature in observations and GCM runs (Dommenges and Latif, 2002a). Processes in

the ocean are responsible for this slower increase of SST variance from interannual to longer timescales (Fig. 8). In the presence of advection, one way to explain the gentle slope of the SST spectra is that the system's response consists of a strong resonant response at zero frequency corresponding to the leading purely damped normal mode which gives rise to the red spectrum, plus some weak resonances at higher frequencies corresponding to the severely damped oscillatory modes, which enhance variability on shorter timescales. Strong resonance at non-zero frequency (spectral peak) can occur only when the advective effect is stronger than the damping effect, which does not seem likely in a realistic setting.

### 3. Predictability and predictable component

Fig. 13 compares the domain average normalized-error-variance for the advective and non-advective models. As can be seen, the error variances for both systems are nearly identical. Taking  $\epsilon = 0.5$  as a threshold for predictability limit, on average the SST field in the North Atlantic can be predicted one month ahead. This finding is consistent with the 1D result (see Fig. 9).

However, the advection, albeit weak, does produce a noticeable impact on the most predictable pattern. This is clearly illustrated in Fig. 14, which compares the most predictable pattern of the advective case with that of the non-advective case.

To gain understanding of this result, let us again consider first the non-advective ocean. In this case, the predictability of the system depends on the local damping rate at this location. A high predictability corresponds to a weak damping and vice versa. A comparison between Figs. 10 and 14a shows that the three regions where the most predictable pattern has large loading correspond to the areas of weak damping.

When advection is present, the most predictable pattern changes significantly along the strong western boundary current region (Fig. 14b). Large loadings in the

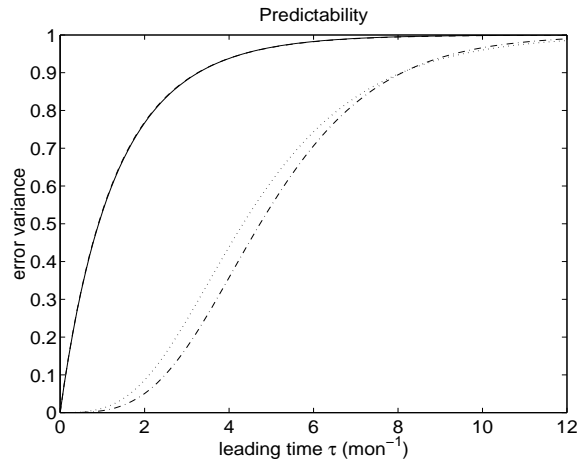


Fig. 13. Predictability of North Atlantic Ocean SST. The overlaying solid and dashed lines denote domain averaged skills for advective ocean and motionless ocean. The dash-dot line and the dotted line are the skills of the most predictable patterns with and without advection.

most predictable pattern are now found along the Gulf Stream region and Caribbean Sea. A closer inspection indicates that the maximal amplitude of the most predictable pattern in these regions tends to occur in the areas where the dominant forcing amplitude is nearly zero (see Fig. 11). This structure seems to be consistent with the mechanism proposed for the 1D case in previous section where it is argued that the center of the most predictable pattern tends to occur close to the location of minimal forcing amplitude (Fig. 11 to Fig. 14b as Fig. 5 to Fig. 7). On the other hand, the pattern in Northwestern Atlantic remains basically unchanged because the circulation is weak there. Overall, the predictability associated with the most predictable pattern shows a modest increase from 4 months in the absence of advection to about 5 months in the presence of advection (Fig. 13). This finding again agrees with the 1D results (the difference between dashed line and solid line in Fig. 9), although for the North Atlantic Ocean, the enhancement of predictability due to advection is relatively small.

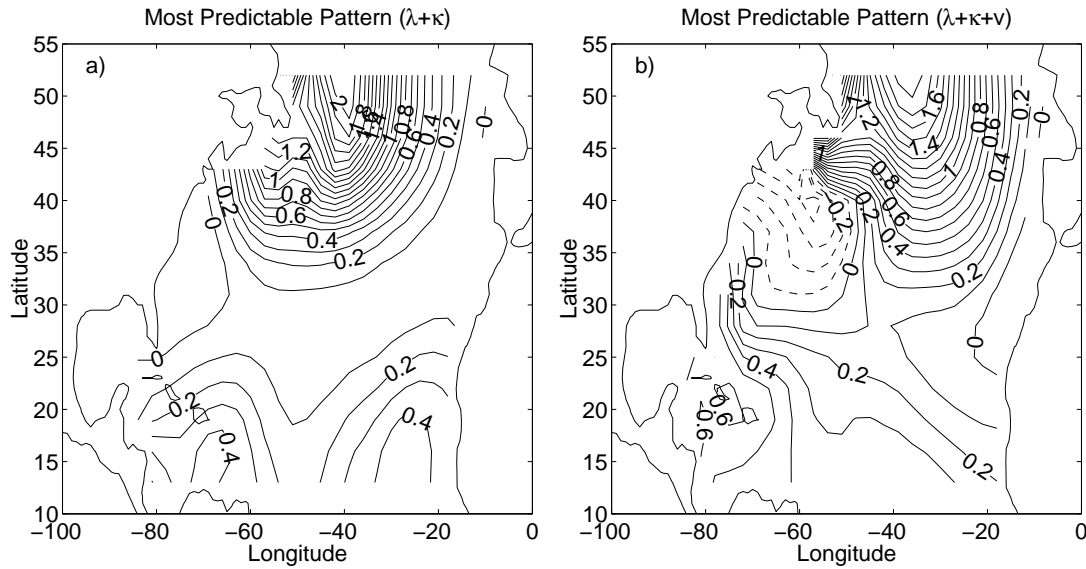


Fig. 14. Most Predictable Pattern at 5 month lead time: a) Without advection; b) with advection. Contour interval is 0.1, and high values denote predictable regions.

## E. Summary

The purpose of this chapter is to study the effect of oceanic advection on the predictability of the sea surface temperature (SST) in the framework of linear stochastic climate models. Using an idealized 1D model, we have found that the total variance and global averaged predictability are determined by local damping and diffusion, independent of advection. Scott (2003) reached the same conclusion using a similar 1D model. He further proposed a “stochastic cancellation” mechanism to explain the spatial inhomogeneity of the predictability. His explanation relies on a local predictability measure. Our approach differs from his in the interpretation of the predictability spatial inhomogeneity. In our approach, we decomposed the total predictive information of the system into a set of uncorrelated components, called predictable patterns, in a similar way that the total variance can be decomposed into a set of EOFs. These predictable patterns give us a global view on how the predictable variance in the

system is distributed. By comparing the most predictable patterns with and without the advection, we are able to examine the effect of the oceanic advection on SST predictability. This analysis not only confirms the theoretical finding of Scott (2003), but also allows us to examine the effect of oceanic advection on SST predictability under a more realistic condition.

As a case study, we applied the predictability analysis to North Atlantic SST with realistic model parameters, such as ocean currents, damping rate, and forcing patterns. The result suggests that the advective effect in the midlatitude ocean is generally weak and does not alter the SST response significantly both in terms of spectral characteristics and spatial structures. The predictability of SST is determined, to a large extent, by the local processes, e.g. air-sea feedback and oceanic entrainment. It implies that for most of the North Atlantic Ocean, Hasselmann's zero-dimensional model is a good approximation. However, ocean circulation can have a significant impact on the spatial distribution of predictable variance. In particular, strong western boundary currents can enhance the predictable variance along the western boundary region where otherwise SST is far less predictable. The enhancement of predictability along the western boundary seems to follow the argument presented in the 1D case where it is shown that the enhanced predictable variance tends to occur in the regions of large SST variance and small noise forcing.

Although the goal of the paper is not to provide an accurate prediction of SST, we believe that the findings here do have an implication on issues concerning climate prediction in reality. In particular, the predictable component analysis of the North Atlantic SST points to the potential important role of the strong western boundary current system in enhancing SST predictability in the region. Given that the SST anomaly in this region may have an effect on predicting regional climate, it is necessary to improve coupled climate models' simulation of the western boundary current.

## CHAPTER IV

## TROPICAL ATLANTIC VARIABILITY AND ITS PREDICTABILITY

## A. Introduction

Perhaps because of its relatively small basin size, the tropical Atlantic Ocean is not dominated by any single mode like the El Niño—Southern Oscillation (ENSO) in tropical Pacific Ocean. Rather, the climate variability in this region is shaped by many influences whose mechanisms and origins are subjected to considerable recent debate. Generally, these influences can be classified into two category: remote forcing such as ENSO and NAO, and variability due to local processes (see Fig. 15).

ENSO is the strongest climate signal on interannual scales and exerts a global influence through teleconnection (Diaz et al., 2001; Alexander et al., 2002). It affects climate in the tropical Atlantic directly by altering the large-scale atmospheric circulation and indirectly through feedback from local SST (Nobre and Shukla, 1996; Enfield and Mayer, 1997; Saravanan and Chang, 2000; Sutton et al., 2000; Giannini et al., 2001a,b; Mo and Häkkinen, 2001; Chiang and Sobel, 2002; Czaja et al., 2002). Only in the latter case, the tropical Atlantic ocean is involved. The main feature of ENSO response in the tropical Atlantic is the weakening of northeast trade winds during boreal winter and spring, which induces positive latent heat anomaly and in turn a warming event in the Atlantic (Enfield and Mayer, 1997; Sutton et al., 2000; Czaja et al., 2002).

Another remote forcing is the atmospheric internal variability from midlatitude, mainly the NAO. Studies show that large portions of the North Atlantic SST variability can be explained as a passive response to this mode (Cayan, 1992; Seager et al., 2000; Marshall et al., 2001b). Such influence can extend as far south as 10°N

## Mechanisms of Tropical Atlantic Variability

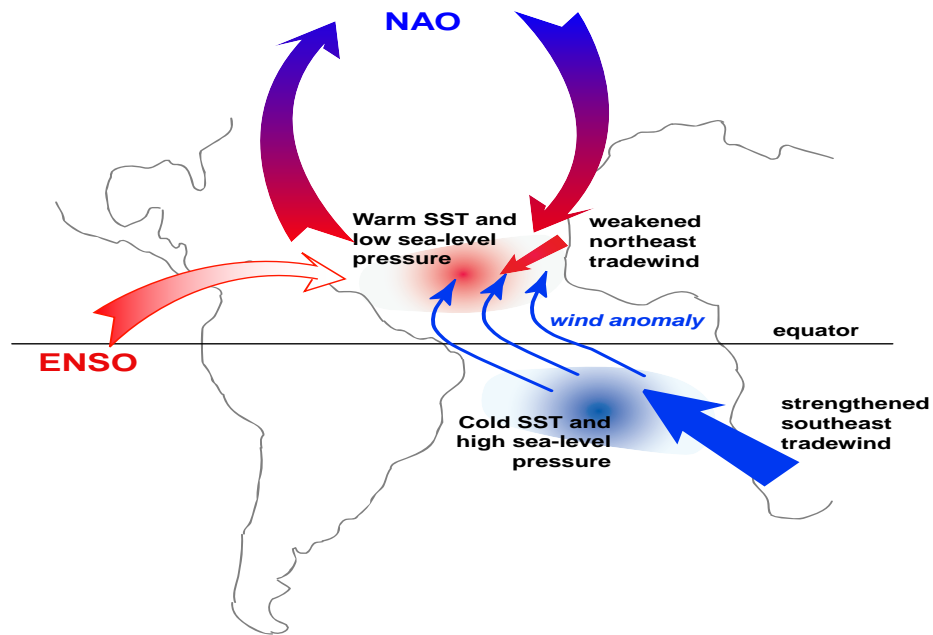


Fig. 15. Elements of tropical Atlantic variability: ENSO, NAO, and local feedback.

during winter when the NAO is most pronounced. Although there are some indications that the NAO is partially driven by SST (Christoph et al., 2000; Hoerling et al., 2001), analysis reveals that most of its variance can be attributed to nonlinear instability processes intrinsic to the atmosphere that possess little predictability on climatic timescales (Greatbatch, 2000; Hurrell et al., 2003).

An inter-hemispheric dipole structure usually stands out in the EOF analysis of tropical Atlantic SSTs, which leads some to believe that it is a coupled mode intrinsic to the Atlantic atmosphere-ocean system (Servain, 1991; Mehta and Delworth, 1995; Nobre and Shukla, 1996; Tourre et al., 1999). Various modeling studies provide further support for the existence of such a decadal meridional mode (Servain et al., 2000; Sutton et al., 2000; Chang et al., 2000, 2001). It is often argued that the most relevant feature of this mode is the SST gradient across equator: it affects the cross-equatorial



low-level winds, hence the location of ITCZ and associated rainfall (Chang et al., 2000; Ruiz-Barradas et al., 2000; Chiang et al., 2002; Tanimoto and Xie, 2002). One of the hypotheses is that the thermodynamical feedback between evaporation heating and SST generates this meridional mode. If initially the SST anomaly is positive (negative) in northern (southern) tropical Atlantic, then a negative pressure gradient is set up, which drives a northward flow across the equator. This secondary Hadley cell interacts with the primary Hadley cell in a such way that the north (south) trades weaken (strengthen), which then creates positive (negative) latent heat flux anomaly in the north (south) and amplifies the initial signal (Carton et al., 1996; Chang et al., 1997). This positive feedback, often referred to as the wind-evaporation-SST (WES) mechanism, has been demonstrated within simple coupled climate models (Xie, 1999; Chang et al., 2001; Kushnir et al., 2002b). However, this hypothesis remains controversial, and some criticisms have been raised because 1) the variability of the north tropical Atlantic (NTA) and the south tropical Atlantic (STA) are uncorrelated to a large extent (Mehta, 1998; Enfield et al., 1999; Dommengeset and Latif, 2000; Häkkinen and Mo, 2002), and the meridional mode is argued to be an artifact of EOF analysis (Dommengeset and Latif, 2002b; Baquero-Bernal et al., 2002), 2) some modeling studies suggest that TAV can be explained as passive oceanic response to atmospheric forcing (Mehta, 1998; Dommengeset and Latif, 2000; Seager et al., 2000, 2001; Häkkinen and Mo, 2002; Czaja et al., 2002), hence positive air-sea feedback may not be a necessary element in defining the TAV (Frankignoul and Kestenare, 2002). Unsurprisingly, such ambiguousness is also reflected by its names: inter-hemisphere gradient mode, meridional mode, thermodynamical mode, and dipole mode.

The other atmosphere-ocean coupled mode within the tropical Atlantic is the equatorial mode (Zebiak, 1993). This equatorial mode has an interannual timescale of about 3-4 years and has been shown to be not self-sustained. Although the spatial

structure and amplitude have notable differences, the basic characteristics of this oscillation are the same as that of the Pacific ENSO mode. During a warm event, SST rises in the eastern equatorial basin, accompanied by a relaxation of the trade winds and a deepening (shoaling) of thermocline in the east (west), which in turn creates a positive feedback. This is different from the above meridional mode, as upper ocean dynamics play an active role here (Battisti and Hirst, 1989). This dynamical mode has maximum amplitude during boreal summer and fall, when ITCZ is furthest away from the equator (Carton et al., 1996; Chang et al., 2000; Ruiz-Barradas et al., 2000; Sutton et al., 2000).

Much of the controversy of the TAV centers on the roles of various elements in defining the climate variability over the tropical Atlantic region. Undoubtedly, to a certain extent this reflects the complex nature of the TAV—there is just no easy way to separate the variability due to internal processes from those due to external forcing, especially for a coupled system. However, some of the confusion may result from: 1) bad experiment design, for example, forcing an AGCM with prescribed SST or forcing OGCM with observations will introduce some artificial effects which misrepresent the coupled feedbacks in the real system (see Seager et al., 1988; Barsugli and Battisti, 1998, for further discussion); 2) misinterpretation of statistical analysis results. From Chapter II and Chapter III, we know that the response of a stochastically forced system is determined by system dynamics plus forcing. Therefore, EOF analysis often does not reveal the modal structure of the dynamical system. In the case of TAV, this means the simple correlation analysis between NTA and STA can not be used to reject or confirm the existence of the thermodynamical feedback. It is entirely conceivable that the NTA is forced by ENSO while STA is forced by midlatitude processes, and thus the independence of the forcing is transferred into the low correlation between the inter-hemisphere SST anomalies. This does not mean that the positive feedback

mechanism is not operating. Another issue is the predictability of TAV, i.e. to what extent tropical Atlantic SSTs are predictable and what the control factors are. To date, there has been no systematic analysis on this important question.

In this study, we try to shed some light on the predictable dynamics of tropical Atlantic SSTs within the framework developed in Chapter II. First, we construct a linear coupled model of intermediate complexity with stochastic atmospheric forcing. Then, the dynamics of the TAV are explored by linear stability analysis, and the predictable components are analyzed. Finally, some conclusions are drawn, and the findings are highlighted.

## B. Model description

The framework developed in Chapter II is only for linear systems. While most climate modes involve more or less nonlinearity, especially in the thermodynamical processes, a linearized coupled system can always be derived by assuming certain steady state and small perturbations. Of course, the question is how good the linearized model is. For example, the irregularity in the well-known Zebiak and Cane (1987) model is critically depended on the existence of nonlinearity, without which the simulated ENSO mode behaves as a regular oscillation with pure growth or decay. As mentioned in Chapter I, another competitive view is that ENSO resides in a linear stable regime under stochastic forcing (Penland et al., 2000). The linear version of the Cane-Zebiak model, constructed by either inverse modeling (Xue et al., 1994; Blumenthal, 1991) or direct linearization (Thompson and Battisti, 2000, 2001), has shown great success in ENSO prediction and predictability studies. Independently, Moore and Kleeman (1996, 1999) have linearized a similar intermediate coupled model of ENSO (Kleeman, 1993) in studying the error growth during the ENSO onset. In

fact, much of the understanding of ENSO, or climate in general, is achieved through linear analysis (for example, Jin and Neelin, 1993a,b; Neelin and Jin, 1993; Weng and Neelin, 1999; Neelin and Weng, 1999), because the full nonlinear system is generally difficult to handle.

For the tropical Atlantic, most observational and modeling studies point to a scenario that the TAV consists of damped oscillations forced by ENSO and NAO (Zebiak, 1993; Chang et al., 2001). Despite its weaker nonlinearity, however, to date we are not aware of any linear model of TAV that includes both thermodynamical feedback and the dynamical feedback, as well as realistic stochastic forcing due to NAO and ENSO. This study will fill this gap by constructing a linearized intermediate coupled model (ICM) of the tropical Atlantic using a forward approach.

### 1. Nonlinear intermediate coupled model

The model used here is a modified version of the intermediate coupled model developed by Chang (1994) and Wang et al. (1995). The oceanic part is an extension of the conventional  $1\frac{1}{2}$  layer (a single moving layer above a motionless abyss) shallow water reduced gravity model which includes thermodynamics of the upper ocean.

Assuming that the effects of compressibility and salinity are of secondary importance within the mixed layer, the equation of SST (or first thermodynamic law) takes the form

$$\frac{\partial T}{\partial t} + \mathbf{u}_s \cdot \nabla T = \kappa \nabla^2 T - \lambda(T - \bar{T}_{\text{obs}}) + \frac{Q}{\rho_0 C_p H_{\text{mix}}} - \frac{1}{H_{\text{mix}}} w_e \mathcal{H}(w_e)(T - T_e) \quad (4.1)$$

where density  $\rho_0 = 1 \times 10^3 \text{ kg m}^{-3}$ ; specific heat at constant pressure  $C_p = 4.2 \times 10^3 \text{ J kg}^{-1} \text{ K}^{-1}$ ; mean depth of mixed layer  $H_{\text{mix}} = 50 \text{ m}$ ; and the coefficient of horizontal turbulent heat diffusivity  $\kappa = 1 \times 10^4 \text{ m}^2 \text{ s}^{-1}$ . And the flux correction term  $\lambda = \frac{1}{200} \text{ day}^{-1}$  is needed to confine the evolution of SST around the observed mean

$\bar{T}_{\text{obs}}$ .

The forcing from the atmosphere is represented by  $Q$  – the sum of all the components of surface heat flux; the effect from bottom (fluid below the mixed layer) is parameterized as entrainment  $w_e$ , which is determined as divergence of surface flow

$$w_e = H_{mix} \nabla \cdot \mathbf{u}_s.$$

The use of Heaviside function  $\mathcal{H}(\cdot)$  in Eq. (4.1) is due to the fact that only entrainment changes  $T$  and detrainment just sinks water down to sublayer without modifying the surface temperature. The temperature of entrained water  $T_e$  is assumed to take a linear form

$$T_e = 0.5 (T + \bar{T}|_{z=50}) + 2 \left. \frac{\partial \bar{T}}{\partial z} \right|_{z=50} h',$$

where  $\bar{T}_{50}$  is the observed mean temperature;  $\left. \frac{\partial \bar{T}}{\partial z} \right|_{z=50}$  is the vertical gradient of  $\bar{T}$  at 50 m depth;  $h'$  denotes the fluctuation of thermocline, i.e.  $h' = h - \bar{h}$ .

The horizontal velocity in the surface mixed layer  $\mathbf{u}_s$  is separated into two components:  $\mathbf{u}_s = \mathbf{u} + \mathbf{u}_e(H - H_{mix})/H$ , where  $H = 100\text{m}$  is the mean depth of thermocline, i.e. the spatial average of  $\bar{h}$ .

Surface Ekman flow  $\mathbf{u}_e = (u_e, v_e)$  is determined by balancing the friction, the Coriolis effect, and wind stress

$$\begin{aligned} r_s u_e - f v_e &= \frac{\tau_x}{\rho_0 H_{mix}} \\ r_s v_e + f u_e &= \frac{\tau_y}{\rho_0 H_{mix}} \end{aligned} \quad (4.2)$$

where the frictional processes in the Ekman layer are idealized to be linear damping  $r_s = \frac{1}{1.5} \text{day}^{-1}$ ;  $f = \beta_0 y$  is the Coriolis parameter of the equatorial beta-plane approximation with  $\beta_0 = 2.29 \times 10^{-11} \text{m}^{-1} \text{s}^{-1}$ ;  $\boldsymbol{\tau} = (\tau_x, \tau_y)$  is the wind stress at sea surface.

The geostrophic flow  $\mathbf{u} = (u, v)$  is governed by linearized shallow-water dynamics

$$\begin{aligned} \frac{\partial u}{\partial t} - fv &= -g' \frac{\partial h}{\partial x} + \frac{\tau_x}{\rho_0 H} + \gamma \nabla^2 u - \alpha u \\ \frac{\partial v}{\partial t} + fu &= -g' \frac{\partial h}{\partial y} + \frac{\tau_y}{\rho_0 H} + \gamma \nabla^2 v - \alpha v \\ \frac{\partial h}{\partial t} + H \nabla \cdot \mathbf{u} &= 0 \end{aligned} \quad (4.3)$$

where  $g' = g\Delta\rho/\rho_0 = 4.17 \text{ cm s}^{-2}$  is the reduced gravity, and  $\alpha = \frac{1}{2.5} \text{ yr}^{-1}$  is the coefficient of linear friction. Note the horizontal eddy viscosity,  $\gamma = 2.5 \times 10^4 \text{ m}^2 \text{ s}^{-1}$ , takes a different value from heat diffusivity  $\kappa$ .

As a common approximation, the atmospheric forcing can be nominally written as the sum of annual mean (or climatology of monthly mean when seasonal cycle is involved), coupled feedback, and atmosphere internal variability

$$\begin{pmatrix} \tau_x \\ \tau_y \\ Q \end{pmatrix} = \begin{pmatrix} \bar{\tau}_x \\ \bar{\tau}_y \\ \bar{Q} \end{pmatrix} + \begin{pmatrix} \mathcal{A}_x(T') \\ \mathcal{A}_y(T') \\ \mathcal{B}(T') \end{pmatrix} + \begin{pmatrix} \zeta_x \\ \zeta_y \\ \eta \end{pmatrix} \quad (4.4)$$

where climatology  $\bar{\tau}$  and  $\bar{Q}$  are usually prescribed from observations;  $\mathcal{A}$  and  $\mathcal{B}$  represent coupling between atmosphere and ocean and are nonlocal functions of SST anomaly. In theory, they can be written as linear integral operator over the entire domain  $\Omega$

$$\begin{aligned} \mathcal{A}(T') &= (\Psi, T') = \iint_{\Omega} \Psi_{(x,y;x',y')} T'_{(x',y';t)} dx' dy' \\ \mathcal{B}(T') &= (\Phi, T') = \iint_{\Omega} \Phi_{(x,y;x',y')} T'_{(x',y';t)} dx' dy' \end{aligned} \quad (4.5)$$

where  $\Psi$  and  $\Phi$  are either estimated by linear regression over observational data sets of  $T'$ ,  $\tau'$ , and  $Q'$ , or given by a simple dynamical model of atmosphere.

Together (4.1), (4.3), and (4.4) form a coupled system with nonlinearity only appearing in the SST equation.

## 2. Linear stochastic model of ICM

Before linearizing a nonlinear system, we need to find an appropriate equilibrium state first. To be consistent in this study, we set the mean state as the steady solution of the ocean model forced by observed mean winds and heat flux. In other words, turn off the coupling and weather noise in (4.4), and then let the ICM run freely to achieve a steady state  $(\bar{\mathbf{u}}, \bar{w}_e, \bar{T})$ . In this way, the constructed state becomes independent of the atmosphere model being used.

Now, let  $T = \bar{T} + T'$ ,  $\mathbf{u} = \bar{\mathbf{u}} + \mathbf{u}'$ . By assuming small perturbations and neglecting the higher order terms, the linearized form of Eqs. (4.1) and (4.3) can be written as

$$\begin{aligned}\frac{\partial T'}{\partial t} &= \mathcal{L}_1 T' - \mathcal{L}_2 \cdot \mathbf{u}' + \mathcal{L}_3 h' + \frac{\eta}{\rho_0 C_p H_{mix}} - \frac{\mathcal{E}\zeta}{\rho_0 H} \\ \frac{\partial \mathbf{u}'}{\partial t} &= \frac{\mu}{\rho_0 H} \mathcal{A} T' + (\kappa \nabla^2 - \alpha - f \mathbf{k} \times) \mathbf{u}' - g' \nabla h' + \frac{\zeta}{\rho_0 H} \\ \frac{\partial h'}{\partial t} &= -H \nabla \cdot \mathbf{u}'\end{aligned}\tag{4.6}$$

where  $\mathbf{k}$  is the unit vector along the vertical axis. Note the Ekman layer dynamics (4.2) and air-sea feedback (4.4) have been implicitly built into the linear model (4.6), constituting four dependent variables  $(T', u', v', h')$  and four equations. All the operators  $\mathcal{L}_i$  are linear and time-invariant (no seasonal cycle)

$$\begin{aligned}\mathcal{L}_1 &= \kappa \nabla^2 - \lambda - \bar{\mathbf{u}}_s \cdot \nabla - \frac{0.5}{H_{mix}} \bar{w}_e \mathcal{H}(\bar{w}_e) + \frac{\nu}{\rho_0 C_p H_{mix}} \mathcal{B} - \frac{\mu}{\rho_0 H} \mathcal{E} \mathcal{A} \\ \mathcal{L}_2 &= \nabla \bar{T} + 0.5 \mathcal{H}(\bar{w}_e) (\bar{T} - \bar{T}_{50}) \nabla \\ \mathcal{L}_3 &= \frac{2}{H_{mix}} \bar{w}_e \mathcal{H}(\bar{w}_e) \frac{\partial \bar{T}}{\partial z} \Big|_{z=50}\end{aligned}\tag{4.7}$$

where operator  $\mathcal{E}$  is due to Ekman pumping and Ekman drift

$$\begin{aligned}\mathcal{E} &= \frac{H - H_{mix}}{H_{mix}} \frac{1}{r_s^2 + f^2} \left\{ \nabla \bar{T} \cdot (r_s - f \mathbf{k} \times) + \right. \\ &\quad \left. \frac{\mathcal{H}(\bar{w}_e)}{2} (\bar{T} - \bar{T}_{50}) \left[ (r_s \nabla - \frac{2f\beta_0}{r_s^2 + f^2} (r_s \mathbf{j} - f \mathbf{i}) - \beta_0 \mathbf{i}) \cdot -f \nabla \cdot \mathbf{k} \times \right] \right\}.\end{aligned}$$

Two new nondimensional parameters are introduced: the coupling strength of the wind stress  $\mu$  and the coupling strength of the heat flux  $\nu$ . They are used to parameterize the sensitivity of coupled system to the air-sea feedback strength. Since the zonal mode and the meridional mode owe their existence to the air-sea coupling, small changes in the coupling strength may induce significant modifications of the behavior of TAV. In fact, studies have shown that boreal spring favors the growth of the meridional mode while boreal fall favors the zonal mode (Ruiz-Barradas et al., 2000; Chang et al., 2000; Sutton et al., 2000). One explanation is the mechanism hypothesized by Zebiak and Cane (1987): the annual cycle causes changes in the mean fields, which in turn affect the strength of the atmosphere-ocean coupling. Therefore, the mean circulation in one season may provide favorable conditions for the development of one type mode but less favorable conditions for the other mode. Without explicitly taking seasonal cycle in consideration, we attempt to study the sensitivity of the coupled system by adjusting coupling strength  $\mu$  and  $\nu$  directly without changing the circulation pattern. For the sake of convenience, we normalize the coupling parameters  $\mu$  and  $\nu$ , such that  $\mu = \nu = 1$  corresponds to the best fit to the observational estimate of air-sea feedback strength for TAV. Naturally, setting  $\mu$  to zero means no coupling in wind stress, and setting  $\nu$  to zero means no coupling in heat flux. In this study, we refer to  $\mu$  as the dynamical coupling parameter and  $\nu$  as the thermodynamical coupling parameter. Furthermore, we assume no dynamical coupling between meridional winds and SST because of its small impact in equatorial region.

a. Statistical atmosphere

$\mathcal{A}(T')$  and  $\mathcal{B}(T')$  in (4.4) represent the steady tropical atmosphere response to SST anomalies. ENSO studies (Neelin et al., 1998) show that simple atmospheric dy-



namical models can give an adequate representation of the surface wind field, i.e. the wind stress feedback  $\mathcal{A}$ . On the other hand, there also exist simple thermodynamical models of heat flux feedback  $\mathcal{B}$  (Seager et al., 1988, 1995). However, simple models for the tropical Pacific may not gain the same success in the tropical Atlantic, and empirical models usually achieve a better performance (Chung et al., 2002).

Following the approach of Chang et al. (1997, 2001), here we construct a statistical atmosphere based on the singular value decomposition (SVD) analysis of SST, wind stress, and heat flux. The basic idea is to identify the coupled mode through analyzing the cross-covariance matrix (see Bretherton et al., 1992; Syu and Neelin, 1995, for details). In the following, we only give a brief description of this technique for discrete data sets.

Let  $n \times m$  matrices  $\mathbf{T}$ ,  $\Theta_x$ ,  $\Theta_y$ , and  $\mathbf{Q}$  denote SST, wind stress, and heat flux anomaly, respectively. If  $n$  is the spatial dimension and  $m$  is the temporal dimension, then the cross-covariance matrix is computed as

$$\mathbf{C}_{3n \times n} = \begin{pmatrix} \Theta_x \\ \Theta_y \\ \mathbf{Q} \end{pmatrix} \mathbf{T}^T. \quad (4.8)$$

The SVD of  $\mathbf{C}$  gives pairs of coupled mode  $(\mathbf{u}_j, \mathbf{v}_j)$  and their relative strength  $s_j$

$$\mathbf{C} = [\mathbf{u}_1, \dots, \mathbf{u}_n, \mathbf{0}] [\text{diag}(s_1, \dots, s_n), \mathbf{0}]^T [\mathbf{v}_1, \dots, \mathbf{v}_n]^T. \quad (4.9)$$

Projecting the state vectors  $\Theta_x$ ,  $\Theta_y$ ,  $\mathbf{Q}$ , and  $\mathbf{T}$  onto their corresponding vectors results in two sets of time series

$$\mathbf{x}_j = \mathbf{T}^T \mathbf{v}_j \quad \text{and} \quad \mathbf{y}_j = \begin{pmatrix} \Theta_x \\ \Theta_y \\ \mathbf{Q} \end{pmatrix}^T \mathbf{u}_j.$$

Because SVD maximizes the covariance between  $\mathbf{x}_j$  and  $\mathbf{y}_j$ , we may write  $y_j$  in terms of  $x_j$  as a linear model by least-squares regression

$$y_j = a_j x_j + \epsilon \quad \text{where} \quad a_j = \frac{\mathbf{y}_j^T \mathbf{x}_j}{\mathbf{x}_j^T \mathbf{x}_j} = \frac{s_j}{\mathbf{x}_j^T \mathbf{x}_j}.$$

Transferring back to physical space gives us the linear relationship of atmosphere-ocean coupling

$$\begin{pmatrix} \mathcal{A}_x \\ \mathcal{A}_y \\ \mathbf{B} \end{pmatrix} = [\mathbf{u}_1, \dots, \mathbf{u}_k] \text{diag}(a_1, \dots, a_k) [\mathbf{v}_1, \dots, \mathbf{v}_k]^T \quad (4.10)$$

where the first  $k$  modes are retained. Generally speaking, it is a multivariate linear regression in space spanned by the singular vectors.

There are two problems associated with the SVD method. One is determining the truncation order  $k$ , which is usually quite arbitrary and guided by physical intuition. In principle, only the first few singular vectors contain useful information since the higher modes are strongly contaminated by noise. In practice, mode number  $k$  is chosen empirically, and then its robustness is tested by studying the sensitivity of the results to  $k$ . The other problem is more severe—there is a loophole in the theoretical formulation. As pointed out by Frankignoul (1999), the above SVD procedure will identify a positive feedback even for a purely atmosphere-force-ocean system. One should be cautious about unstable modes if a statistical atmospheric model is used. One remedy is applying SVD to lag-covariance, which has been tried by Solomon et al. (2003) without much success. On the other hand, if we know there is a positive feedback in the system, SVD analysis will identify it correctly, which is the case in the tropical Atlantic (Chang et al., 2001)

Finally, the atmospheric internal variability needs to be specified. According to

(4.4), if we know the total field, the climatology, and the linear response to local SST, the residual could be regarded as the external forcing

$$\begin{pmatrix} \zeta_x \\ \zeta_y \\ \eta \end{pmatrix} = \begin{pmatrix} \Theta_x \\ \Theta_y \\ Q \end{pmatrix} - \begin{pmatrix} \mathcal{A}_x \\ \mathcal{A}_y \\ \mathcal{B} \end{pmatrix}^T, \quad (4.11)$$

where the linear feedbacks are given by (4.10). EOF decomposition is applied to determine the spatial and temporal characteristics of the forcing

$$\begin{pmatrix} \eta \\ \zeta_x \\ \zeta_y \end{pmatrix} = \mathbf{F}_{3n \times l} \mathbf{W}_{l \times m} \quad (4.12)$$

where the first  $l$  EOFs are used. The EOFs have been weighed by their variance, i.e.  $\mathbf{F}^T \mathbf{F} = \text{diag}[\sigma_1^2, \dots, \sigma_l^2]$ , and  $\mathbf{W} \mathbf{W}^T = \mathbf{I}_{l \times l}$ .

The characteristics of the PC time series are crucial in defining the evolution of the linear dynamical system (4.6): if  $\mathbf{W}$  is precisely known, then future states of (4.6) can be predicted without any error. The worst scenario, in a prediction sense, is that we know nothing about  $\mathbf{W}$  except its variance (zero mean by default). In that case, we are unable to infer the future state of forcing based on its present and past states. In statistical language, this means the process  $\mathbf{W}$  is totally unpredictable. Such a stochastic process is usually categorized as white noise with Gaussian distribution  $\mathcal{N}(0, 1)$ . To test whether  $\mathbf{W}$  is indeed a white noise process, we apply the procedure outlined in Chapter II. Fig. 16 shows the results for the first 200 PC time series along with 99% confidence interval. Most of the sampled autocorrelations are not significantly different from zero, which means the white-noise hypothesis is an acceptable assumption overall. However, we also note a few PC time series, not necessarily the dominant ones, have non-zero lag-correlations (with 99% confidence). We speculate

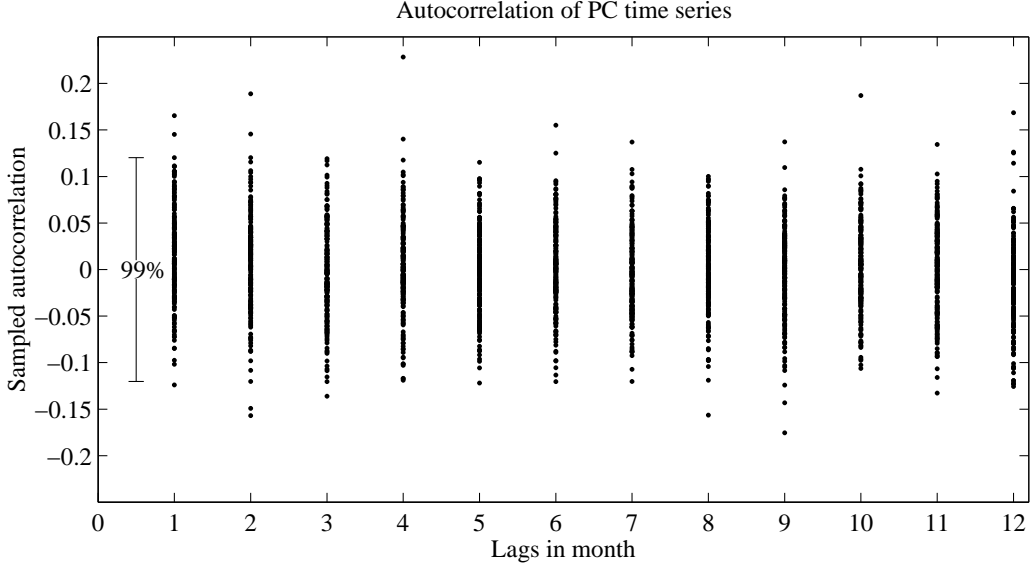


Fig. 16. Whiteness test of stochastic forcing in tropical Atlantic. The null hypothesis is that time series is white noise, i.e. its autocorrelation should be zero at any lag. If the sampled correlation lies outside the confidence interval, the null hypothesis is rejected, and the stochastic process is not white.

that these modes represent the influence from ENSO which has a longer persistence. Assuming ENSO forcing, contains a red spectrum with a broad interannual peak, white will certainly underestimate the predictability of TAV.

In summary, we have derived a linear stochastic model for TAV

$$\frac{d\mathbf{x}}{dt} = \mathbf{A}\mathbf{x} + \mathcal{F}\boldsymbol{\xi} \quad (4.13)$$

where the linear operator  $\mathbf{A}$  denotes the deterministic dynamics of (4.6),

$$\text{state variable } \mathbf{x} = \begin{pmatrix} T' \\ u' \\ v' \\ h' \end{pmatrix}, \quad \text{forcing pattern } \mathcal{F} = \frac{1}{\rho H} \begin{pmatrix} \frac{H}{C_p H_{mix}} & -\mathcal{E}_x & -\mathcal{E}_y \\ 0 & | & 0 \\ 0 & 0 & | \\ 0 & 0 & 0 \end{pmatrix} \mathbf{F},$$

and the white noise  $\langle \boldsymbol{\xi}(t)\boldsymbol{\xi}^T(\tau+t) \rangle = \delta(\tau)\mathbf{I}$ . (4.13) falls into the framework of stochastic climate model, thus the analysis is straightforward. The following discussion will mainly focus on the physical implication, and interested readers are referred back to Chapter II for technical details.

#### b. Numerics

The differential operator  $\mathbf{A}$  and  $\mathcal{F}$  are casted into a matrix form by finite-differencing on a staggered C-grid with a resolution of  $\Delta x = 2^\circ$ ,  $\Delta y = 1^\circ$  within the tropical Atlantic basin from  $20^\circ\text{S}$  to  $20^\circ\text{N}$ , which gives a dimension of  $3462 \times 3462$ . The boundary conditions are no-flux for SST and  $h$ , no-normal flow and free-slip for current.  $1^\circ$  sponge layers are added along the southern and northern boundaries into thermodynamical equation, while for dynamical equations it is  $10^\circ$ . The observations are taken from the monthly COADS data set (da Silva et al., 1994) for 1950-1990 with  $2^\circ \times 2^\circ$  resolution and projected onto the model grid by simple meridional interpolation.

In our statistical atmosphere, the SST-forced component is composed of the first three singular vectors, which explain 27% of the squared variance in SVD space. The remaining variance is due to atmospheric internal variability, which is modeled by 200 EOFs. This in general agrees well with the estimate of Sutton et al. (2000) in the tropical Atlantic: atmospheric internal variability dominates the fluctuations of the wind stress and heat flux while SST-forced variance is low ( 30%). Since SST is the oceanic variable of interest to climate, in this study we define its skill as the measure of the predictability of TAV. Finally, all the computations are made possible by two free Fortran libraries, LAPACK (Anderson et al., 2000) and SLICOT (Benner et al.,

1999), and most figures are drawn in MATLAB<sup>®</sup>.<sup>1</sup>

### C. Physical modes in the tropical Atlantic atmosphere-ocean system

For the linear system (4.13), eigenmodes of operator  $\mathbf{A}$ , in which the boundary condition is embedded, represent the true (in ICM sense) physical modes of the tropical Atlantic atmosphere-ocean system.

#### 1. Free modes

Without coupling, the shallow-water equations in (4.6) separate from the SST equation, while each contains its own set of eigen-modes.

The SST modes are the eigenfunctions of operator  $\mathcal{L}_1$  defined in (4.7), which are determined by the advection and dissipation processes. The modes, as shown in Chapter III, typically contain a set of purely damped modes and a set of propagating modes with phase speed  $U$  and period  $T = \frac{L}{nU}$ , where  $U$  and  $L$  are characteristic length and time scales of the circulation. The equatorial (surface) current system of the Atlantic Ocean includes mainly three zonal features: Equatorial Countercurrent, North Equatorial Current, and South Equatorial Current, plus one northward western boundary current, namely North Brazil Current  $\rightarrow$  Guyanan Current  $\rightarrow$  Caribbean Current. Due to truncated north and south boundaries, however, the ocean circulation within the model domain does not form a closed loop. Therefore, the eigen-spectrum of these SST modes is a continuum rather than a discrete set as in Chapter III.

For an unlimited basin, the free modes of shallow-water equations are the equatorial Kelvin, Rossby, and inertia-gravity waves (see Philander, 1990). While short

---

<sup>1</sup>MATLAB<sup>®</sup> is a registered trademark of The MathWorks, Inc.

high-frequency waves dissipate very quickly in the ocean once generated, the gravest baroclinic waves can survive a long time to exert pivotal influence on interannual variability like ENSO. In our ICM, the phase speed of the first Kelvin wave is  $c = \sqrt{g'H} = 2 \text{ m/s}$  eastward, which gives a cross-basin travel time of about 1 month for equatorial Atlantic ( $L = 6000 \text{ km}$ ). The first Rossby wave travels westward with  $\frac{c}{3}$ , hence a 3-month cross-basin time. Once they reach the boundaries, reflections take place. At the eastern boundary, incident Kelvin waves reflect into a pair of coastal Kelvin waves and a set of long Rossby waves with less energy (due to poleward leak); at the western boundary, Rossby waves reflect as equatorial Kelvin waves plus a set of short Rossby waves (Philander, 1990). Therefore, the free Kelvin and Rossby waves for an unbounded ocean are no longer eigensolutions for a zonally bounded basin. Taken the lateral boundary into consideration, a new set of eigenmodes, known as the basin modes, can be found (Cane and Moore, 1981; Neelin and Jin, 1993; Jin, 2001). These modes are composed of Kelvin and long Rossby waves with periods determined by the sum of their crossing time. For the least damped basin mode, theory predicts a period  $\frac{L}{c} + \frac{3L}{c}$  (Cane and Moore, 1981).

Using realistic coastline, we identify the basin mode of the tropical Atlantic ocean by solving the linear shallow-water model within the equatorial band  $10^\circ N \sim 10^\circ S$ . To prevent the boundary-trapped Kelvin waves from crossing the basin along the southern and northern boundaries,  $2^\circ$ -wide sponge layers are added to the model. Fig. 17 shows the least damped basin mode along with the SST component. As the theory predicts, the basin mode propagates westward with a period about 4 months. It is best described as the sum of equatorial Kelvin and long Rossby waves. Variations in SST are a passive response to basin mode ( $\mathbf{u}'$ ,  $h'$ ): anticyclone  $\rightarrow$  convergence  $\rightarrow$  downwelling  $\rightarrow$  warm anomaly, vice visa, cyclone  $\rightarrow$  divergence  $\rightarrow$  upwelling  $\rightarrow$  cold anomaly. Note the argument is based on the first equation of (4.6) with  $\mathcal{L}_1 = 0$ .

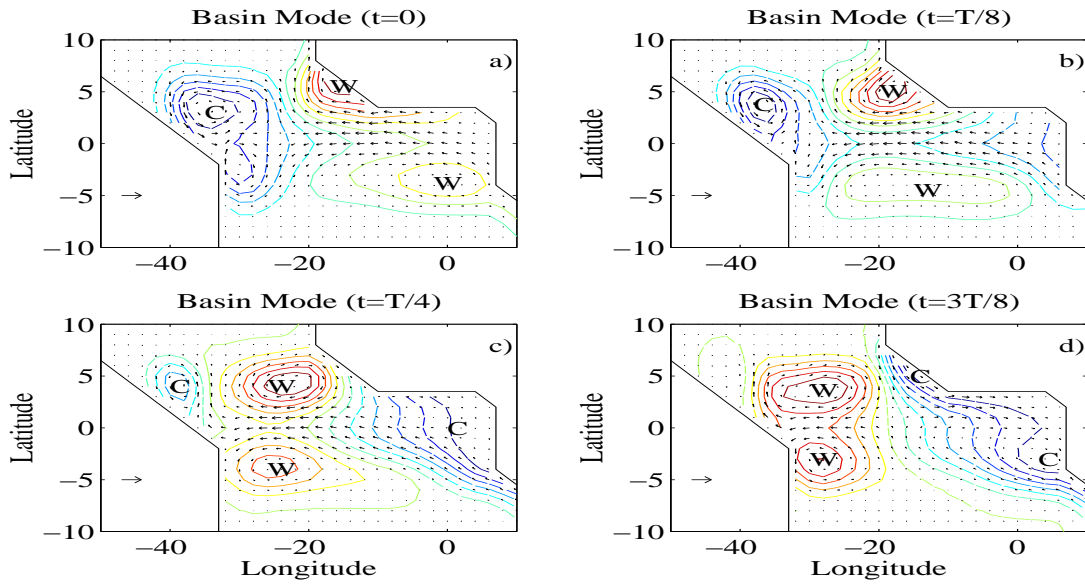


Fig. 17. Basin mode of equatorial Atlantic Ocean at different phases: a) 0; b)  $\frac{\pi}{4}$ ; c)  $\frac{\pi}{2}$ ; d)  $\frac{3\pi}{4}$ . Solid (dashed) line denotes positive (negative) thermocline anomaly, while W (C) denotes warm (cold) anomaly. Arrows are ocean currents.

One fundamental implication of this uncoupled case is that within the tropical Atlantic basin, there is no ocean mode at interannual and decadal timescale (except for the mean current). One must look elsewhere for an explanation of the meridional and the equatorial mode.

## 2. Coupled modes

When atmosphere and ocean are coupled together through energy and momentum transfer, some new modes emerge from the large-scale air-sea interaction. To facilitate this discussion, we adopt the common usage here: all modes are sorted in ascending order in terms of the damping rate, i.e. the first mode is the least damped (most unstable) mode. Complex conjugate pairs of eigenvectors, which form oscillatory modes, are regarded as possessing two degrees-of-freedom. Real eigenvectors



are referred to as stationary modes which may grow or decay exponentially. Within parameter space, the merging of two eigenvalues is an indication of 2-degeneracy, by which an oscillatory mode may split up into two distinct stationary modes.

a. Pure thermodynamical coupled mode

Without wind stress feedback, the leading modes in our model are pure SST modes, in the sense that there is no corresponding signal in the dynamical components,  $u$ ,  $v$ , and  $h$ . For a realistic thermodynamical coupling strength  $\nu = 1$ , the first mode is an oscillatory mode with a period of 25 years, an  $e$ -folding time of 10 months, and antisymmetric centers of action at  $15^\circ S$  and  $15^\circ N$  (Fig. 18). The main feature of this decadal oscillation resembles the meridional mode described in other literature (Carton et al., 1996; Nobre and Shukla, 1996; Chang et al., 1997, 2000, 2001; Sutton et al., 2000; Ruiz-Barradas et al., 2000), although the cause of the slow southward propagation shown in Fig. 18 is not quite clear at this moment (but see Section D).

In order to reveal its relation to the free SST modes described in Section C.1, we have tested the sensitivity of this meridional mode by varying the thermodynamical coupling strength. Fig. 19 shows the damping rate and frequency of the first three modes as a function of  $\nu$  for  $\mu = 0$ . The most notable feature is the linear increase in frequency and decrease in damping rate of the meridional mode with an increasing  $\nu$  and the seemingly zero-effect of coupling on the background free mode. When the coupling is sufficiently strong,  $\nu > 1.6$ , the system becomes unstable although the spatial pattern of the meridional mode remains unchanged. When the coupling strength is reduced, the meridional mode goes through a series of bifurcations. First, 2-degeneracy occurs at  $\nu = 0.76$  where the oscillatory meridional mode changes into two stationary modes with similar spatial structure. However, if the thermodynamical feedback is further weakened to the point that the first three modes have similar

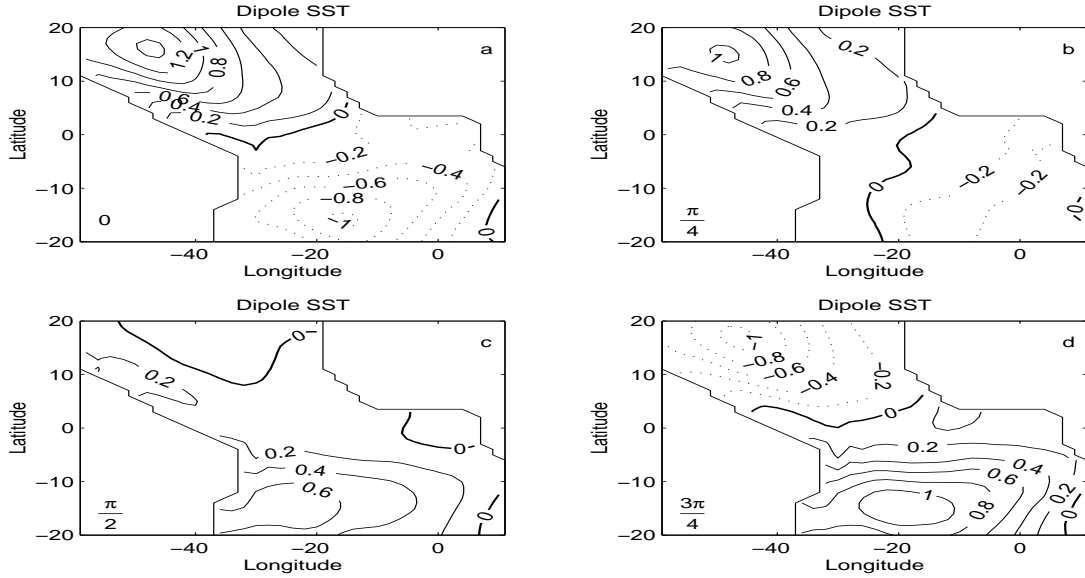


Fig. 18. Meridional mode for  $\mu = 0$ ,  $\nu = 1$ . (a), (b), (c), and (d) depict half period of the oscillation. Unit of SST,  $^{\circ}\text{C}$ ; period, 25 years;  $e$ -folding time, 10 months.

damping rate, mutual-interference begins, and the meridional mode loses its dipole character. Through 2-degeneracy at  $\nu = 0.32$ , a new oscillatory mode emerges with a century-long period. Fig. 20 shows the half-period evolution of this mode: it behaves like a standing oscillation with only a monopole feature in the northern tropical Atlantic. When  $\nu \rightarrow 0$ , the leading modes are essentially the stationary modes in the zero-coupling case. It is convenient to think that the role of thermodynamical coupling in this parameter regime ( $\nu < 0.13$ ) is to give strength to the free mode with a north-south dipole structure. Therefore, depending on the coupling strength, the SST may exhibit an oscillating meridional mode, two stationary modes, or an oscillating monopole features, which makes the TAV a much harder problem to study.

In Fig. 19, most if not all background free modes are not affected by thermodynamical feedback, which leaves us wonder whether the meridional mode is really a purely coupled phenomenon. By stripping down the ICM (4.6), i.e. eliminating the

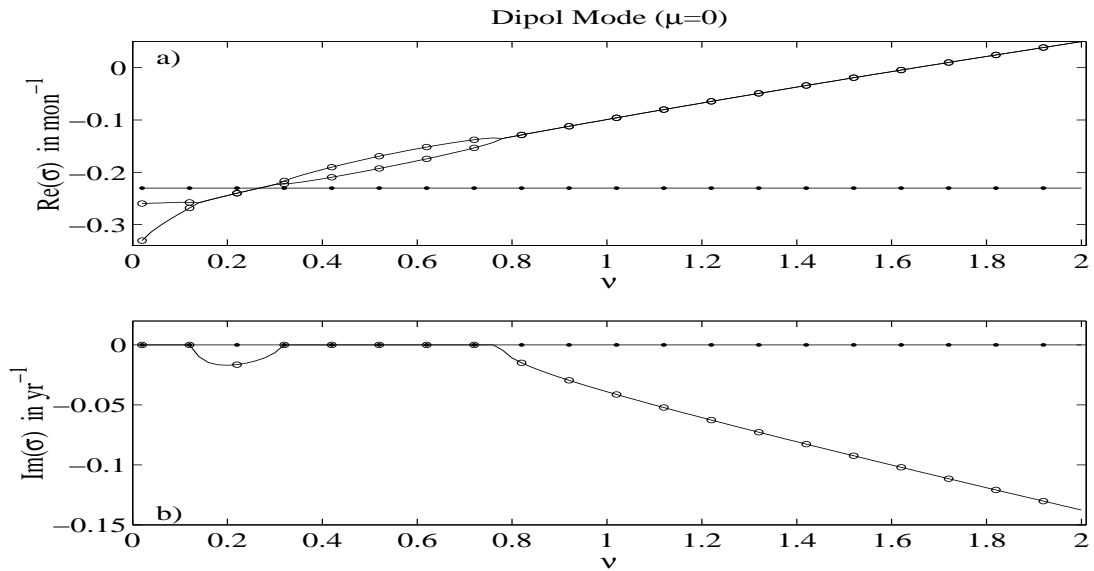


Fig. 19. Eigenvalue of the meridional mode for  $\mu = 0$ : growth rate,  $\text{Re}(\sigma)$ ; frequency,  $\text{Im}(\sigma)$ . The meridional mode is marked by open circles; free mode is solid dots.

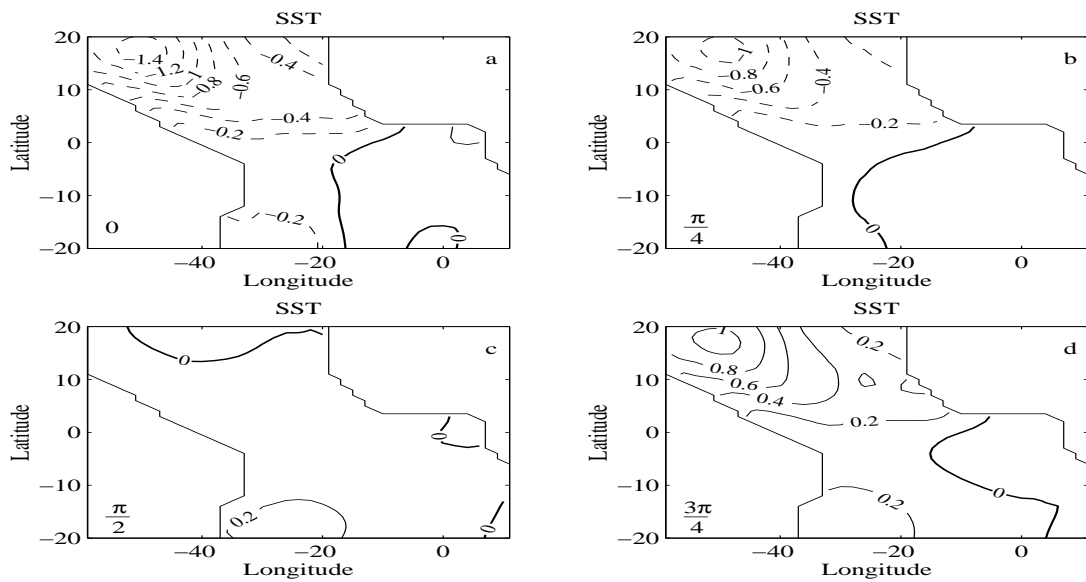


Fig. 20. A weak coupled SST mode for  $\mu = 0$ ,  $\nu = 0.3$ . Oscillating period, 150 years; and damping time scale, 4.5 months.

dynamic terms one by one, we conclude that the meridional mode truly originates from thermodynamic air-sea interaction, and without  $\mathcal{B}$  in  $\mathcal{L}_1$ , no oscillation can be found as leading mode. Fig. 21 depicts the eigenmode of  $\mathcal{B}$  with standard coupling  $\mu = 1$  and diffusion. The signature of the southward-propagating meridional mode is eminent, even though the oscillating period, 11 years, is shorter than that of the mode with ocean advection. Some variability also appears along the equator at transient states. Based on the fact that the coupled model is a meridional feature and the mean meridional ocean transport is northward, a one-dimensional picture can be drawn to explain why the mean advection seems to slow down TAV and how the 2-degeneracy happens. The thermodynamical coupling gives rise to an southward propagating signal, while the mean advection creates northward movement. In the strong coupling case, the former dominates which results in a slower (longer period) oscillation. As the strength of coupling decreases, the northward and southward propagation tendencies are canceling each other out and achieving a balance where the mode becomes stationary. This corresponds to the bifurcation point at  $\nu = 0.76$  in Fig. 19. The crucial role of the mean meridional transport was first invoked in explaining the meridional mode by Chang et al. (1997, 2001). Passing this point, we might still loosely think the leading modes are dipole but without decadal oscillation. However, for weak coupling ( $\nu < 0.32$ ), the mean basic states and finite-basin effects play a much more decisive role. The structures of leading modes are mainly inherited from the SST modes in the ocean without air-sea coupling ( $\nu = 0$ ). Since the realistic parameter regime of TAV lies around  $\nu = 1$ , the decadal meridional oscillation is likely to be a robust feature in the tropical Atlantic sector.

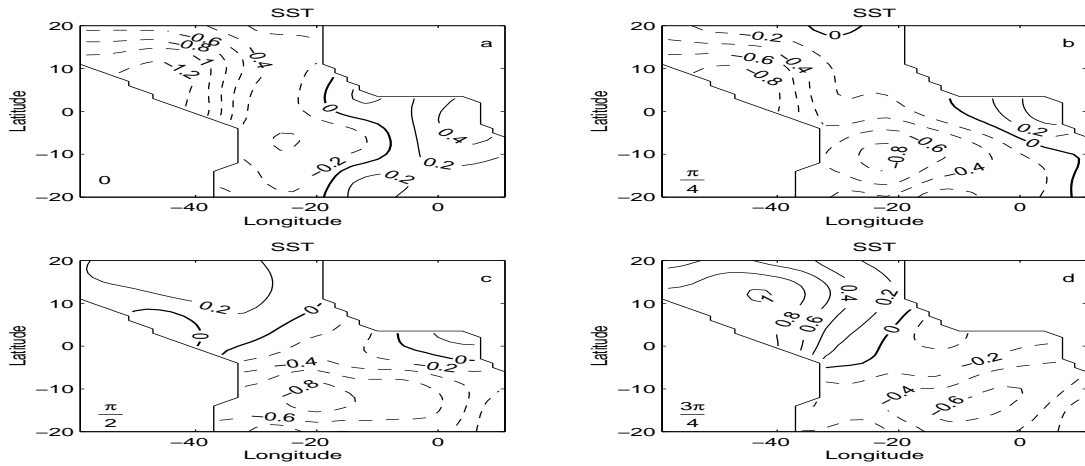


Fig. 21. Thermodynamical mode given by SVD analysis of COADS data. First three singular vectors are used, and oscillating period is 10 years for  $\nu = 1$ .

b. Pure dynamical coupled mode

Without thermodynamical feedback, (4.6) in principle are similar to the governing equations of ENSO dynamics (Cane and Zebiak, 1985; Zebiak and Cane, 1987). For a realistic coupling parameter of tropical Atlantic, it does produce an equatorial mode: the east equatorial region experiences anomalous warm and cold events iteratively within a 3 year period. Fig. 22 shows the half-period evolution of SST and thermocline anomalies associated with this mode. Phase 0 represent the structure of a mature cold episode. The cold SST anomaly extends to  $30^\circ\text{W}$  with a maximum being locate near the eastern boundary. We also see the slight eastward migration of positive anomalies from the western region during retreat of the cold event and rapid westward migration from eastern region during growth of the warm event. On the other hand, the maximum thermocline variability (about 8 m) occurs along the western boundary, while the eastern tropical Atlantic experiences a weak thermocline perturbation (less than 4 m). However, because of the shallow location of mean

thermocline over the eastern equatorial Atlantic, a small perturbation in thermocline induces a significant change in SST via modulation of subsurface upwelling. In addition, Fig. 22 shows a dynamically significant feature: the thermocline anomaly leads the SST anomaly. Although the phase difference is small, it characterizes the oceanic memory and produces the interannual oscillation.

The essential elements of this equatorial mode are usually summarized as the Bjerknes (1969) hypothesis: SST anomalies cause trade winds to strengthen or weaken which in turn drive the ocean circulation to enhance the initial SST changes. This provides a positive dynamical feedback in which SST affects the atmosphere through diabatic heating. Suarez and Schopf (1988) and Battisti (1988) further advanced our understanding by proposing the prototype of simple model—the delayed oscillator—for ENSO

$$\frac{dT(t)}{dt} = T(t) - \alpha T(t - \delta_T) - T^3(t). \quad (4.14)$$

This paradigm of ENSO physics incorporates the propagation and reflection of the first baroclinic Kelvin wave and Rossby waves into a conceptual simple dynamic framework. Crucial factors in this model include the time delay  $\delta_T$ , which is about 6 months for the tropical Pacific and 4 months for the tropical Atlantic, and the relative strength of the positive air-sea feedback to thermal damping  $\alpha$ . When the air-sea feedback and oceanic adjustment reach a proper balance, a 3~4-year oscillation arises. Subsequently, model (4.14) has been modified to include more dynamical details (see Jin, 1997a,b; Galanti and Tziperman, 2000). Even though some issues have been raised to question the relevance of the delayed oscillator to ENSO, this simple model remains to be a useful concept in our understanding of ENSO dynamics. We will not elaborate on this theoretical aspect further and instead refer interested readers to relevant literature on this subject.

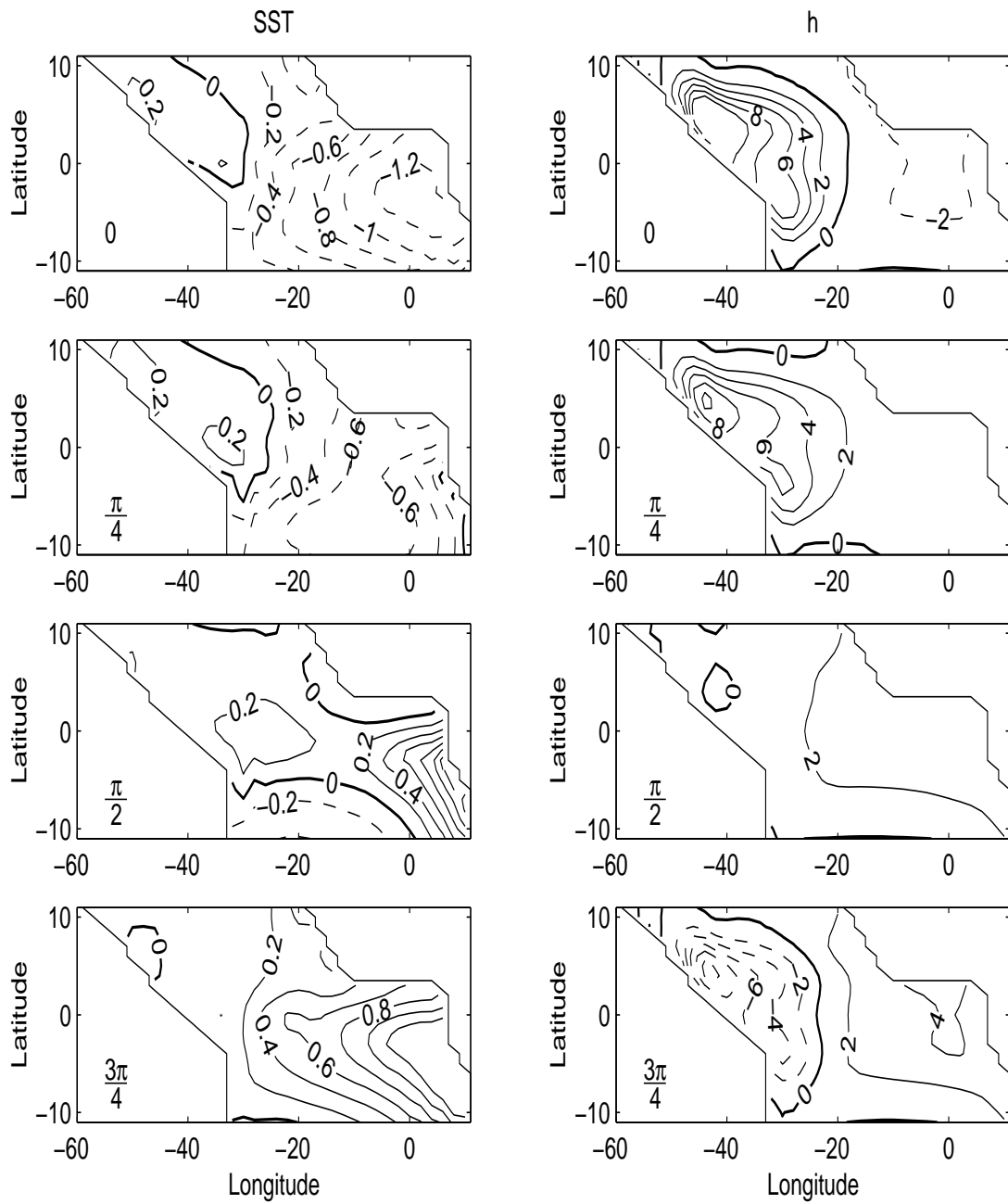


Fig. 22. Equatorial mode in tropical Atlantic for  $\mu = 1, \nu = 0$ : cold (0)  $\rightarrow$  transient ( $\frac{\pi}{4}$ ,  $\frac{\pi}{2}$ )  $\rightarrow$  warm ( $\frac{3\pi}{4}$ ). Left panel, SST anomaly in degree; right panel, thermocline perturbation in meters. The associated anomalous currents are not shown here. Period, 3 years; damping time, 6 months.

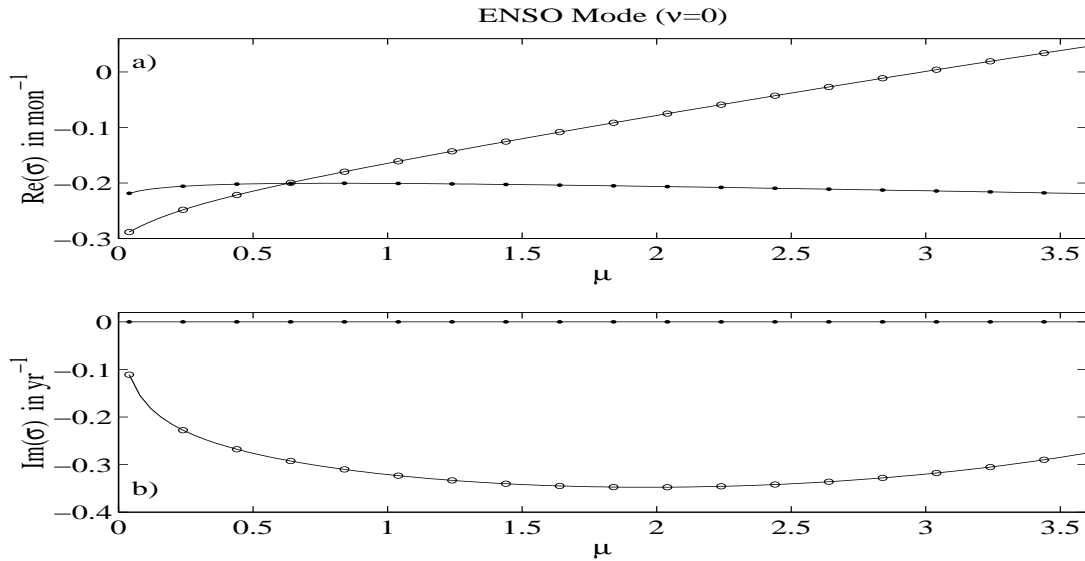


Fig. 23. Eigenvalue of the equatorial mode for  $\nu = 0$ . Equatorial mode is marked by open circles; background mode is marked by solid dots. Note the  $2\pi$  factor has been absorbed into  $\text{Im}(\sigma)$ .

We will now focus on the discussion of how the coupling strength affects the period, structure, and stability of this dynamical mode in the tropical Atlantic Ocean. Fig. 23 shows the real and imaginary parts of first three eigenvalues as a function of the dynamical coupling strength  $\mu$ . The stationary background mode, which is independent of coupling, remains the same as the thermodynamical coupling case, except now it has a pattern similar to the mature phase of the equatorial mode. For a moderate coupling, the Atlantic equatorial mode becomes the most dominant mode with its growth rate increasing linearly with coupling strength. The characteristic spatial structure of this oscillating mode is determined by the mean SST, ocean current field, and coupling pattern (not strength). Unlike the meridional mode, the period of equatorial mode has a parabolic relation with coupling strength  $\mu$ . Too weak or too strong coupling always results in a longer timescale variability. Even



though the Atlantic basin has small geometry, no less than a 3 year oscillation can be found, which is consistent with the finding of Zebiak (1993). He demonstrated that the differences in mean currents and ocean stratification of the Pacific and Atlantic offset the differences in basin size, allowing similar oscillation periods. Overall, this equatorial coupled mode is another robust feature of tropical Atlantic, and it appears once the dynamical feedback, no matter how weak, is introduced.

### 3. Mixed modes

Following the last two sections, one natural question is what happens when both the meridional mode and the equatorial mode coexist. This is not just a theoretical issue, it has important practical value because observation and modeling evidence (Carton et al., 1996; Chang et al., 2000; Dommenges and Latif, 2000; Sutton et al., 2000; Ruiz-Barradas et al., 2000) points to the fact that TAV has two preferred timescales: interannual (equatorial mode) and decadal (meridional mode). In order to better understand the predictability of TAV, the ICM should capture both modes and the interaction between them.

For realistic thermodynamical and dynamical coupling strength, Figs. 24 and 25 show the structure of the first two leading modes. The least damped one has a decadal period of 24.6 years with a dipole pattern (Fig. 24 ); the second least-damped mode is an interannual oscillation of 3.4 years with an ENSO-like appearance (Fig. 25). By comparing with the pure thermodynamical coupled mode (Fig. 18) and the dynamical coupled mode (Fig. 22), one notices some new features. the meridional mode is now more confined against the western boundary, while some variability appears in east equatorial Atlantic— a trace of the equatorial mode. On the other hand, the equatorial mode spreads more meridionally such that its influence reaches beyond 10°N and 10°S. The *e*-folding timescale of the meridional mode is 10 months, which

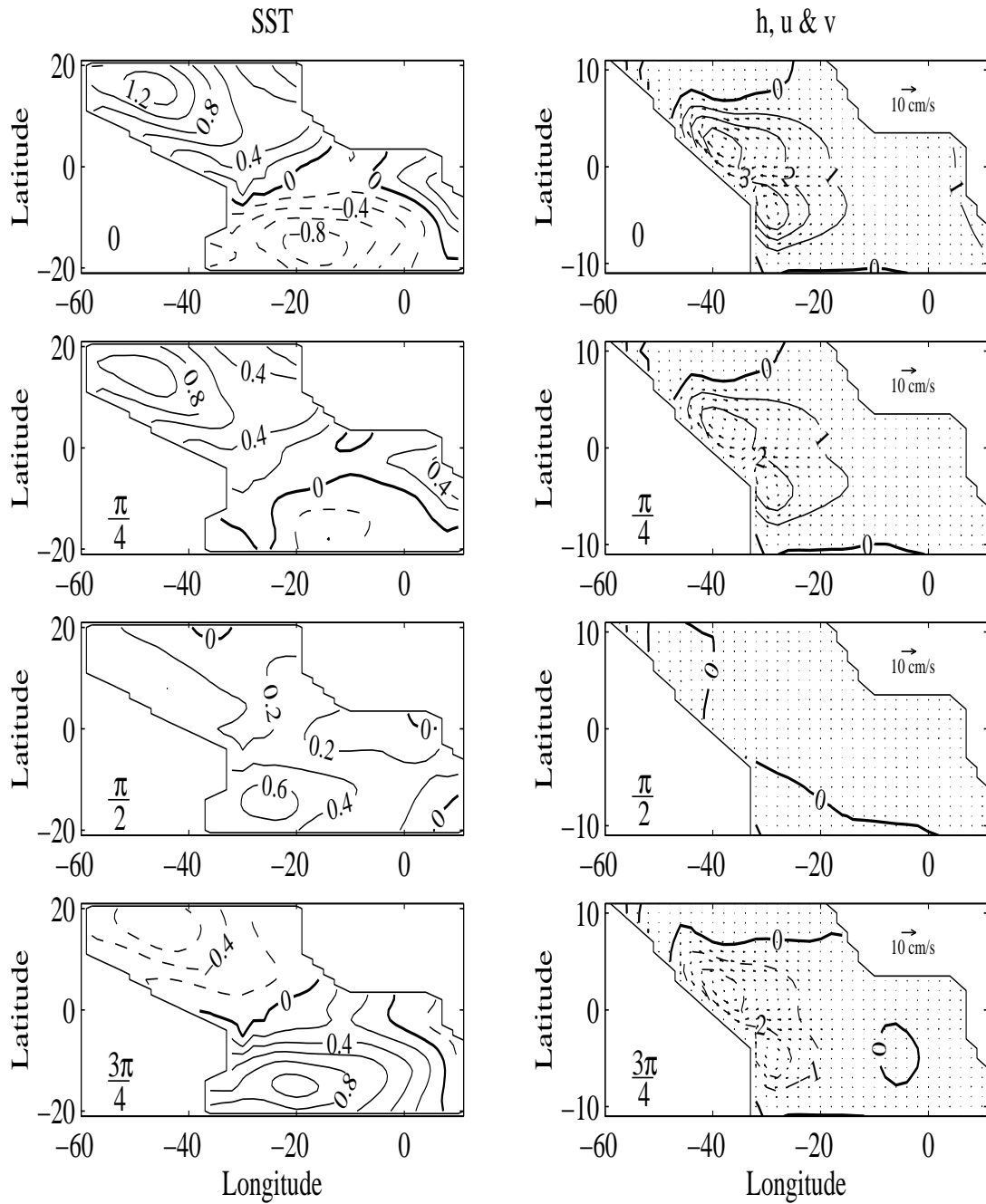
Dipole Mode ( $\mu=1, \nu=1$ )

Fig. 24. Mixed meridional mode for  $\mu = 1, \nu = 1$ . Compare with Fig. 18.

is essentially unchanged from the pure thermodynamical-coupling case; whereas the damping timescale is 4 months for the Atlantic equatorial mode, which has been shortened in comparison to the case of pure dynamical-coupling.

To further illustrate the interaction between these two coupled modes, we test their sensitivity to changes in coupling parameters  $\mu$  and  $\nu$ . Figs. 26 and 27 show the first four eigenvalues as a function of the strength of thermodynamical feedback  $\nu$  and dynamical feedback  $\mu$ , respectively. The two feedbacks compete with each other in an exclusive way: when one dominates, the effect of other is suppressed. For example, increasing the strength of thermodynamical feedback while keeping the dynamical feedback constant will make the meridional mode less stable and equatorial mode more stable (Fig. 26), and vice versa (Fig. 27). This competing effect between the two modes has an impact on the predictability of TAV, as will be seen in Section F.

The common variable which controls both thermodynamical feedback and dynamical feedback is the wind that is tightly coupled to SST in the deep tropics. This leads us to a simple explanation for the competing effect of feedback. The inter-hemisphere SST gradient associated with the meridional mode drives cross-equator winds, which due to the Coriolis effect have zonal components near the equator. The zonal winds, which are essential to ENSO-like dynamics, link the meridional mode to the equatorial mode. However, the phase and period of the meridional mode is totally distinct from the equatorial zonal-mode. Therefore, the slacken or strength of trade winds in the western and central equatorial Atlantic correlates little with the SST over the eastern equatorial Atlantic, which means the positive feedback loop of ENSO is broken-down or suppressed. The above scenario is the case when thermodynamical coupling is dominant. When equatorial dynamics prevail, the same argument can be applied: strong zonal winds associated with the equatorial mode prevent the inter-hemisphere transport through the atmosphere, hence the meridional mode will be

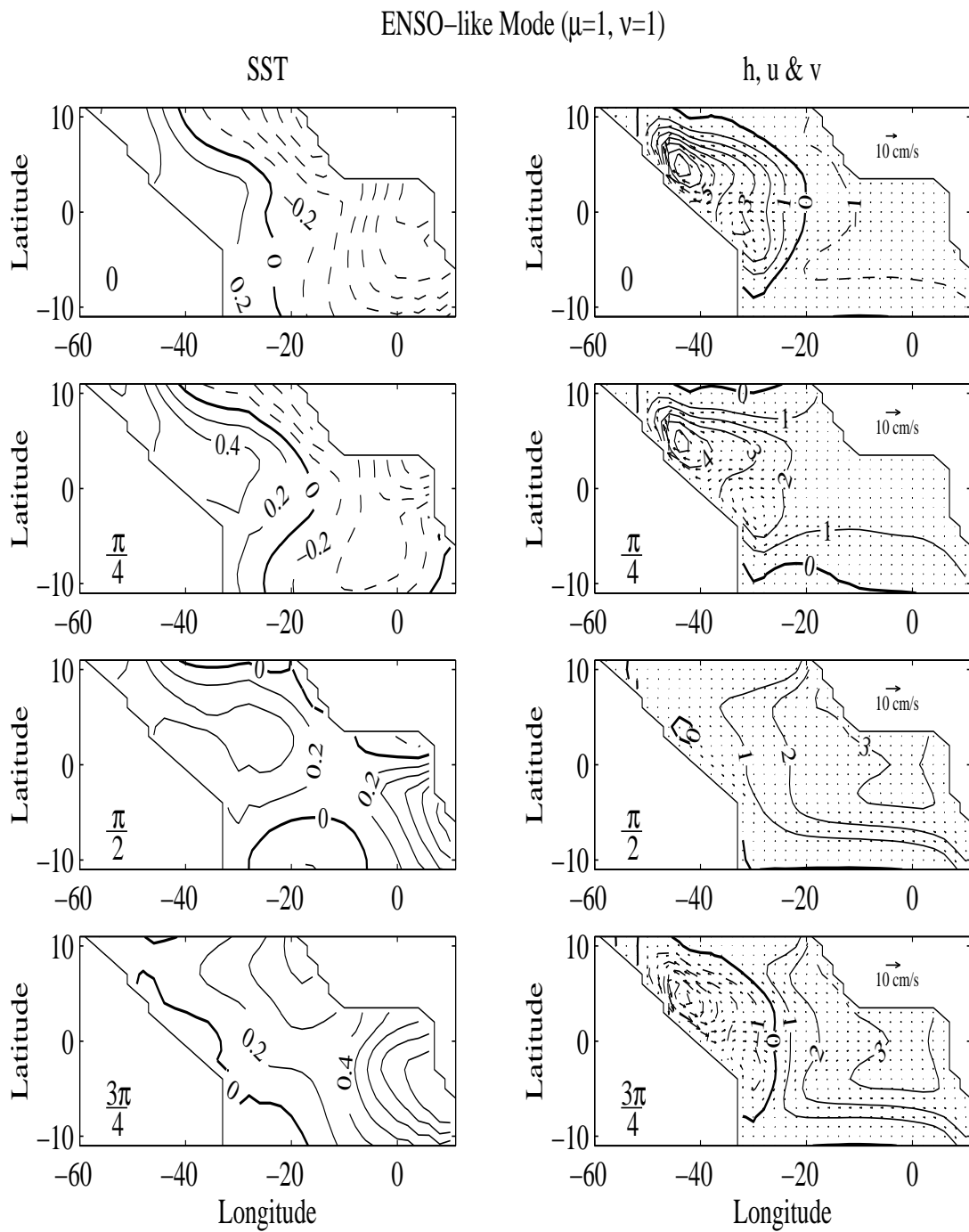


Fig. 25. Mixed equatorial mode for  $\mu = 1, \nu = 1$ . Compare with Fig. 22.

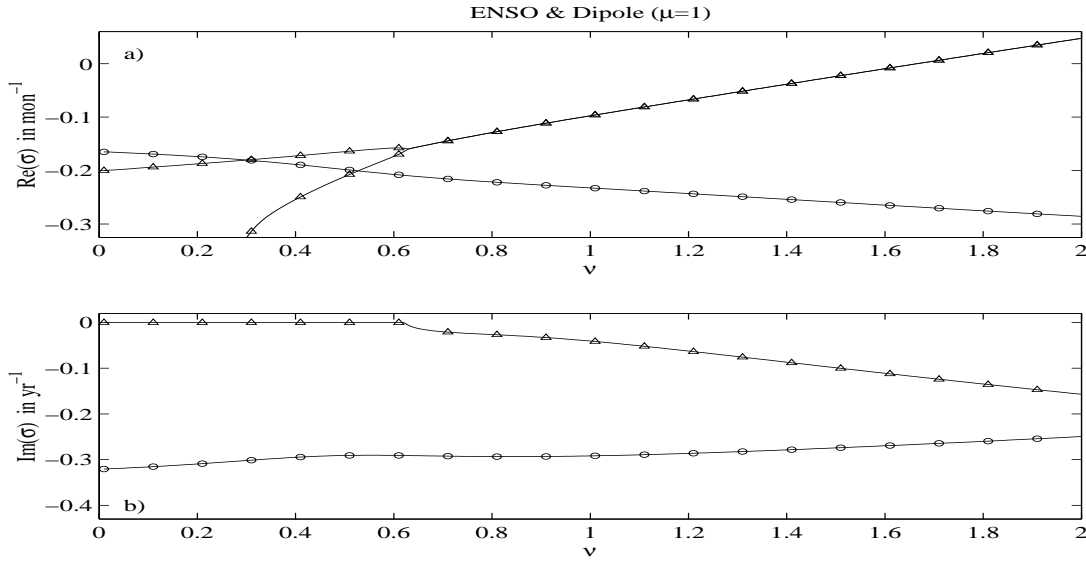


Fig. 26. Eigenvalue of mixed mode for  $\mu = 1$ . Equatorial mode is marked by open circle, meridional mode by up-triangle. A  $2\pi$  factor has been included in  $\text{Im}(\sigma)$ .

suppressed. Furthermore, the southward propagation of the meridional mode is also broken by this barrier of equatorial mode, hence the two stationary modes degenerated from dipole oscillation are farther separated in comparison to the no dynamical coupling case.

In conclusion, the tropical Atlantic contains two sets of coupled modes: the meridional mode and the equatorial mode. The former is caused by thermodynamical feedback, while the latter is due to the positive feedback between winds, SST, and subsurface ocean dynamics. These two types of modes play a dominant role in the coupled system by affecting its evolution and predictability. In the following section, we are going to investigate how the stochastic forcing excites these physical modes.

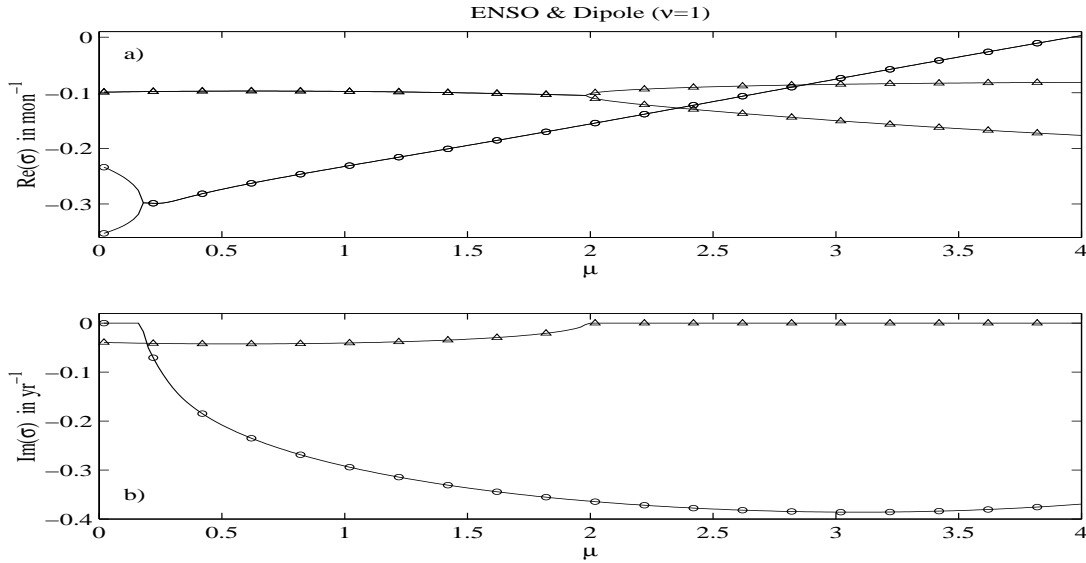


Fig. 27. Eigenvalue of mixed mode for  $\nu = 1$ . Equatorial mode is marked by open circle, meridional mode by up-triangle. A  $2\pi$  factor has been included in  $\text{Im}(\sigma)$ .

#### D. Comments on the debate of Atlantic dipole mode

As mentioned earlier, there has been controversy about the existence of the Atlantic dipole mode in the literature. Our comment on this controversial issue is based on the stochastic climate model of TAV (4.6). Fig. 28 shows the EOFs and the correlation of tropical Atlantic SST anomaly simulated by the ICM under realistic stochastic forcing. The first EOF exhibits a dipole-like pattern with stronger center of action in the south, which explains about 29% of the total variance. The second EOF (21%) has a strong action in the east equatorial ocean which resembles the equatorial mode. The de-correlation time of north tropical Atlantic (NTA) and south tropical Atlantic (STA) are about the same, 6 months. Cross-correlation shows that variability in NTA leads that of STA, which is consistent with the southward propagation of the meridional mode in our ICM. We also note that the overall correlation between NTA

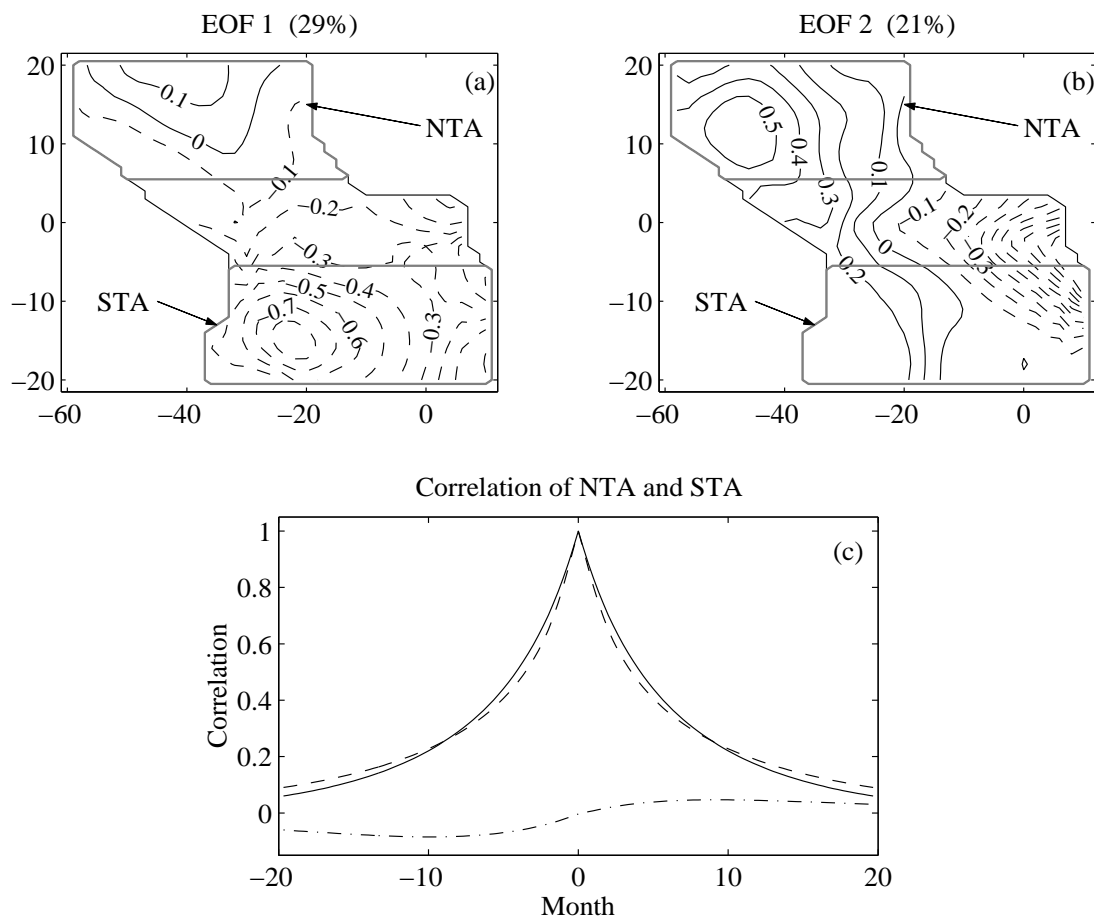


Fig. 28. EOFs and correlation of simulated tropical Atlantic variability ( $\mu = 1$ ,  $\nu = 1$ ). (a) First EOF; (b) second EOF of SST anomalies in  $^{\circ}\text{C}$ . Contour interval is 0.1; negative contours are dashed. (c) Spatial-averaged auto-correlation in north tropical Atlantic (NTA,  $5^{\circ}\text{N} - 20^{\circ}\text{N}$ ), solid line; south tropical Atlantic (STA,  $5^{\circ}\text{S} - 20^{\circ}\text{S}$ ), dashed line; and cross-correlation function between them, dot-dashed line. Positive lag indicates NTA leads STA.

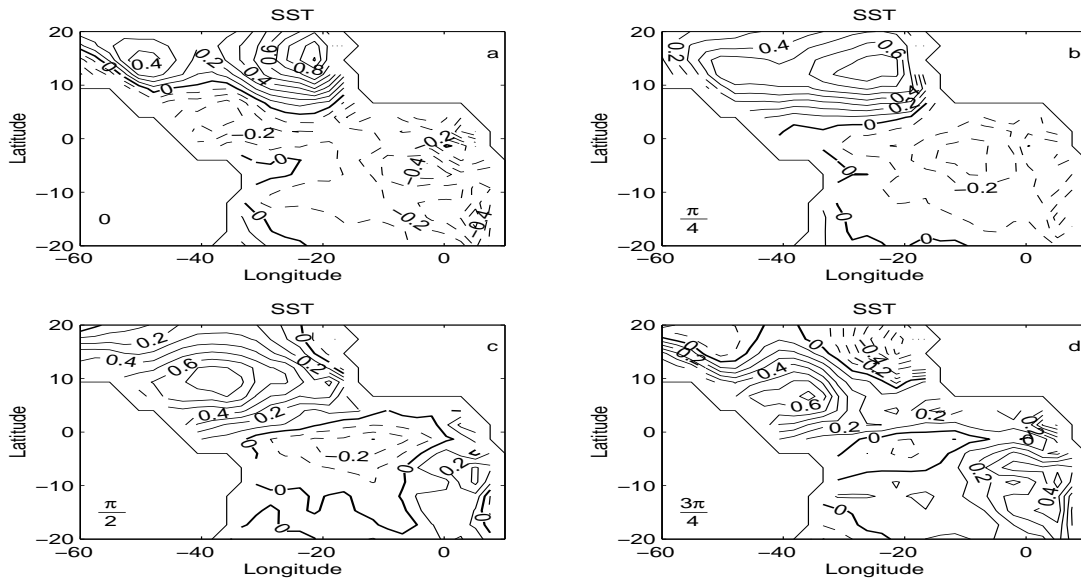


Fig. 29. Thermodynamical coupled mode in CCM3 run with slab ocean.

and STA is very low ( $< 0.07$ ), which is statistically insignificant in light of the local persistence and consistent with the observational analysis. Overall, the ICM does reproduce the key features of TAV found by other researchers (Carton et al., 1996; Nobre and Shukla, 1996; Enfield and Mayer, 1997; Ruiz-Barradas et al., 2000; Sutton et al., 2000). From the stability analysis, however, we know that there exist a dipole-like meridional mode and an ENSO-like equatorial mode in the system. The EOFs of TAV shown in Fig. 28 capture some characteristics of the true coupled modes. Therefore, the absence of a clear dipole pattern and of a significant correlation between NTA and STA do not prove that a dipole-like coupled mode does not exist. More importantly, these statistical analyses do not shed light on the physical processes of air-sea feedback in the tropical Atlantic.

The second comment we would like to make concerns the issue of whether the dipole-like mode is generated by pure thermodynamical feedback. The meridional



mode in our ICM (4.6) is a direct result of the positive thermodynamical feedback identified by the SVD analysis of COADS observations. One potential problem is that the existence of this coupled mode can be due to the artifact of statistics. To address this issue, we turn to an AGCM experiment, in which the NCAR Community Climate Model version 3 (CCM3; Kiehl et al., 1998) is coupled to a slab ocean model, hereafter CCM3-MXL. The ocean mixed layer temperature  $T$  anomaly is simply calculated via the equation

$$\rho_o C_o h_o \frac{dT}{dt} = Q$$

where  $\rho_o$  is the density of ocean water,  $C_o$  is its heat capacity,  $h_o$  is the annual mean mixed layer depth derived from Levitus (1982), and  $Q$  is the net anomalous atmosphere to ocean heat flux. Obviously, the only possible feedback in such a coupled model is through local thermodynamical processes: atmosphere drives ocean via  $Q$  and causes SST changes, which in turn affects atmosphere circulation above, and hence the heat flux down to the ocean.

To test this idea, we applied the same SVD analysis (Section B.1.a) to a 100-year T42 CCM3-MXL run. Fig. 29 shows the dominant coupled mode constructed by using the first 10 singular vectors. It depicts a 4-year south-westward propagating oscillation with large loading in the northern Hemisphere. Such movement has also been noticed by Mehta (1998) and Chang et al. (2001). Comparing it with the SVD mode from observations (Fig. 21), we find the mode from CCM3-MXL has a much shorter period, which may reflect the difference of ocean dynamics in the two data sets. However, the main point here is that pure thermodynamical feedback itself can sustain a low-frequency oscillation, which can not be explained by the simple stochastic climate model (Hasselmann, 1976).

In principle, the wind-evaporation-SST (WES) feedback is responsible for the

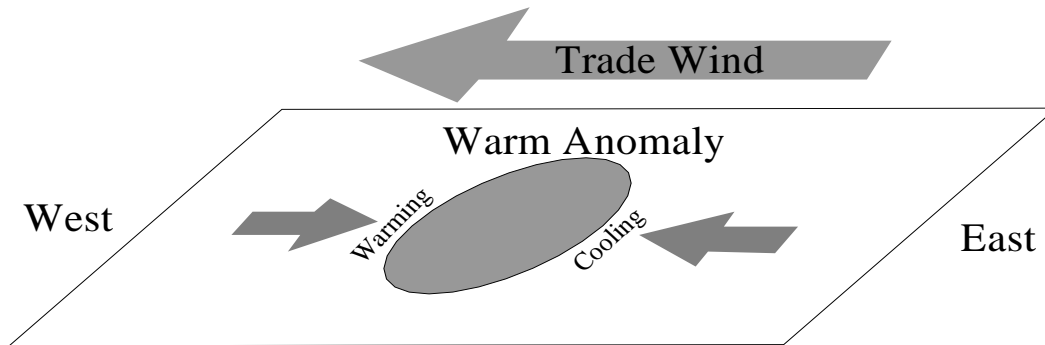


Fig. 30. Cartoon of thermodynamical feedback in tropics. Trade winds (bigger arrow) blow from east to west, while anomalous winds (smaller arrows) cause warming and cooling on the west and east side of SST patch.

growth of the above unstable mode (Chang et al., 1997; Xie, 1999). To stabilize the oscillation, both authors argued ocean dynamics, like the mean current, provide the necessary negative feedback. Thus, traditional WES hypothesis does not explain the westward propagation seen in Fig. 29. However, Zhou and Carton (1998) found WES process alone can produce such a propagating SST mode, at least in their simple and intermediate model. The basic idea is captured in Fig. 30. A patch of warmer SST in the tropical ocean, via pressure gradient, causes an anomalous westerly to the west and an anomalous easterly to the east. Taking mean trade winds into consideration, the west side of the SST patch experiences weaker winds and less evaporation, and the east side has stronger winds and more evaporation. Therefore, the SST is bounded to the west by anomalous warming and to the east by anomalous cooling. Such configuration acts to move the original SST anomaly westward, which seems responsible for the propagation in Fig. 29. Due to the large thermal inertia of an oceanic mixed layer, this thermodynamic process takes a longer time (years) to adjust in contrast to equatorial wave dynamics.

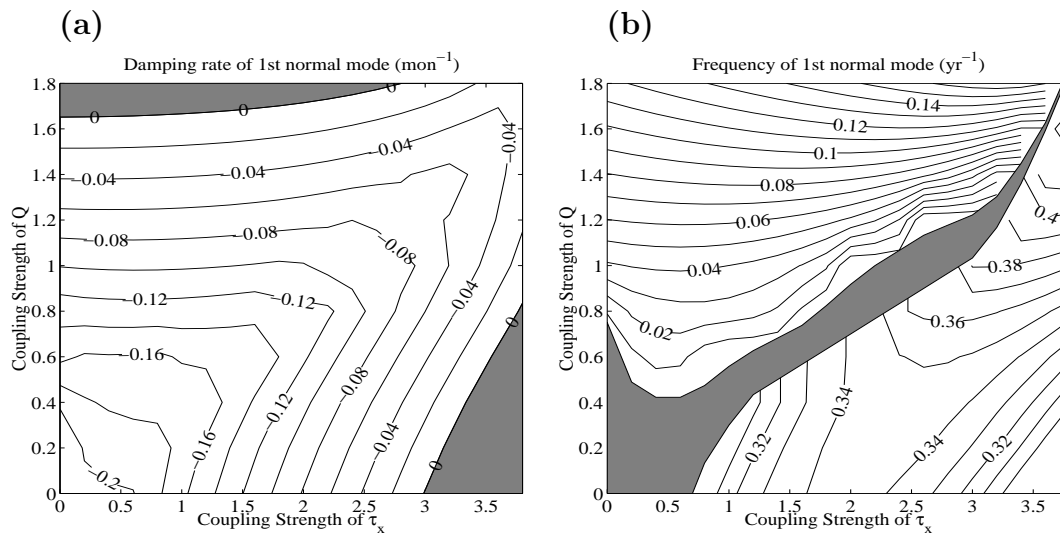


Fig. 31. Eigenvalue of first normal mode as a function of coupling strength: (a) Real part is the damping rate; (b) imaginary part is the frequency. Shading area in (a) delimits the unstable regime and in (b) depicts the no oscillation (zero-frequency) regime.

#### E. An exploration of coupling parameter space

It becomes clear from the analysis in Section C that the behavior of the coupled modes depends heavily on the coupling strength, which itself varies with the mean states (Zebiak and Cane, 1987; Zebiak, 1993; Chang et al., 1997; Fedorov and Philander, 2001). An exploration of coupling parameter space can tell us how the tropical Atlantic atmosphere-ocean coupled mode responds to changes in the strength of dynamical feedback and thermodynamical feedback.

Fig. 31 shows the frequencies and damping rates of the leading coupled modes as a function of coupling strength  $\mu$  and  $\nu$  while the other parameters are kept constant. As expected, strong coupling usually leads to weak damping and eventually the system becomes unstable (shading area in Fig. 31a). However, such transition is not of special interest here because the TAV is regarded as stable. More useful information can be extracted by dividing the parameter space into three regimes ac-

ording the oscillating period of the leading mode (Fig. 31b): 1) the thermodynamic regime where leading mode is decadal oscillation, 2) the dynamic regime where leading mode is interannual oscillation, and 3) the overlay regime where leading mode is non-oscillating. In the thermodynamic regime, both the period and damping rate of leading mode are primarily determined by strength of heat flux coupling, while the effect of dynamical feedback is of secondary importance. In the dynamic regime, although the damping rate is largely defined by winds stress coupling, the destructive effect of heat flux coupling is not negligible (see also Fig. 26). Furthermore, the oscillating period of the equatorial mode remains to be around 3 years with little changes. This reflects a long-known fact: the period of equatorial mode is not determined by any single factor, but it is a result of balancing various processes, such as thermocline depth, mean currents, SST, and winds (Cane and Zebiak, 1985; Zebiak and Cane, 1987; Neelin et al., 1998).

When neither feedback dominates, from Figs. 26 and 27 we know 2-degeneracy usually happens to the meridional mode, which results in two nonoscillatory modes. Perhaps the most interesting regime is where thermodynamical feedback and dynamical feedback have equal strength. What happens in this regime, we think, is that the equatorial mode induces a negative heat flux feedback near the equator, thus it weakens the positive thermodynamical feedback associated with the meridional mode. As a result, the equatorial mode loses its oscillatory characteristics and becomes a stationary mode. Further investigation is needed to find the mechanism for this interaction.

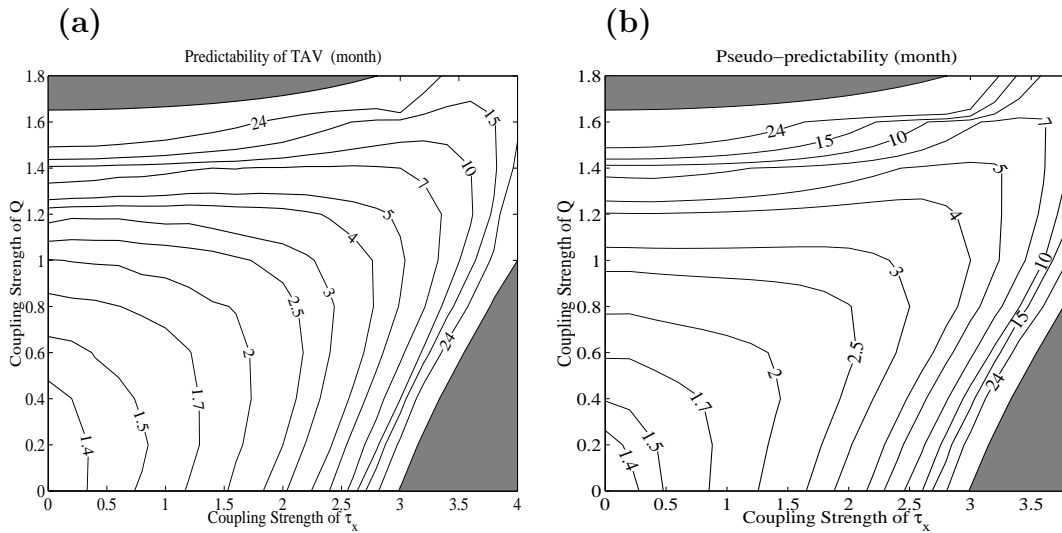


Fig. 32. Predictability of tropical Atlantic SST as a function of  $\mu$  and  $\nu$ : (a) Domain-averaged measure; (b) pseudo-predictability based on the damping rates of first four normal modes. Shading area delimits the unstable regime. Predictability is measured by the time  $\tau_m$  when  $\epsilon(\tau_m) = 0.5$ , i.e. error and signal have equal variance.

## F. Predictability

Finally, we investigate the predictability of TAV within the framework of the ICM. Using normalized error variance as the predictability measure, we take a systematic view of the predictable dynamics of tropical Atlantic SST. Following the previous discussion, we should take  $\epsilon \leq 0.5$  as useful forecast skill. The leading time  $\tau_m$  of  $\epsilon(\tau_m) = 0.5$  will be the limit of predictability.

### 1. Global measure

Fig. 32a shows the predictability of the tropical Atlantic SST as a function of coupling strength  $\mu$  and  $\nu$ . In comparison with Fig. 31, one immediately recognizes the striking similarity between the patterns of damping rate and predictability. However, only for sufficiently strong coupling, can the predictability of tropical Atlantic be

accurately inferred from the damping rate of the first normal mode,  $\tau_m = \frac{-\ln 2}{2\text{Re}(\sigma)}$ . This is because in the strong coupled regime, the first normal mode is so much dominant that itself determines the time evolution of the coupled system. In the weak coupled regime (low-left corner in Fig. 31a), the decay rate is mainly determined by the damping term in Eq (4.1); and the predictability is primarily defined by the special setting of stochastic forcing. If the random forcing were spatially uncorrelated, then the useful prediction skill would be very short. Between the two extremes lies the area where both deterministic dynamics and stochastic forcing are important in shaping the predictability.

A general finding from Fig. 32a is that strong coupling makes TAV more predictable. There are also some additional interesting features. In the thermodynamic regime, the predictability is determined by heat flux–SST coupling with little influence from wind stress feedback. In the dynamic regime, the predictability is primarily defined by feedback between wind stress and SST, although some contribution from heat flux feedback is also visible. In the regime where both thermodynamical/dynamical feedback are strong, we see the mutual-cancellation of wind stress and heat flux feedback in terms of predictability. For a realistic coupling strength, the TAV is predictable for up to 2 months. The sharp contrast between the predictability (Fig. 32a) and the period (Fig. 31b), both in terms of times scale and space pattern, echos one of the main points from Chapter II and Chapter III, i.e. the period of oscillation has little to do with the predictability. In fact, the existence of oscillation may have no effect at all on the domain-averaged forecast skill (see Chapter III).

For the tropical Atlantic, one imperative question is whether we can get reasonable estimates of the predictability given the information of only leading normal modes. For normal system and unitary forcing, we have a definitive answer which is given by Eq. (2.32). In analogy, we may define the pseudo-predictability measure of

TAV based only on the damping rates of its first four normal modes. Fig. 32b depicts such a measure as a function of coupling strength. Note for most of the parameter space, the first four normal modes (oscillation counts two) represent the meridional mode and the equatorial mode. Not surprisingly, the measure from leading normal modes usually overestimates the predictability of TAV. Given the fact that TAV is nonnormal and the stochastic forcing is spatially coherent, the surprising result is the overall consistency between Fig. 31a and b. This means much of the predictable dynamics of tropical Atlantic is well captured by the meridional mode and the equatorial mode. What matters is not the oscillations themselves but their stability, which is controlled by positive air-sea feedback among other processes.

## 2. Local measure

Although the domain-averaged error variance measure gives a rather dismal result about the predictability of tropical Atlantic SST, some patterns may exist that are more predictable in certain regions. In other words, the high predictability could be localized to only a few special regions in the tropical Atlantic. To identify these special patterns, we apply the predictable component analysis developed in Chapter II to the ICM (4.6) for different coupling strength. Fig. 33 shows the leading time at which the most predictable pattern has a normalized error variance of  $\varepsilon = 0.5$ . In comparison with the global measure, there is a substantial increase in the skill. For the example of  $\mu = 1$  and  $\nu = 1$ , the predictability limit of the most predictable pattern is 8 months, while it is 2 months for the global SST. Even in the absence of coupling, the TAV has a component that possesses 5~6 months predictability. These findings prove to be very useful in defining the objective of climate forecast: the basin-average SST does not have much predictability skill beyond 2 months, but some specific SST features can be predicted for almost 1 year in advance.

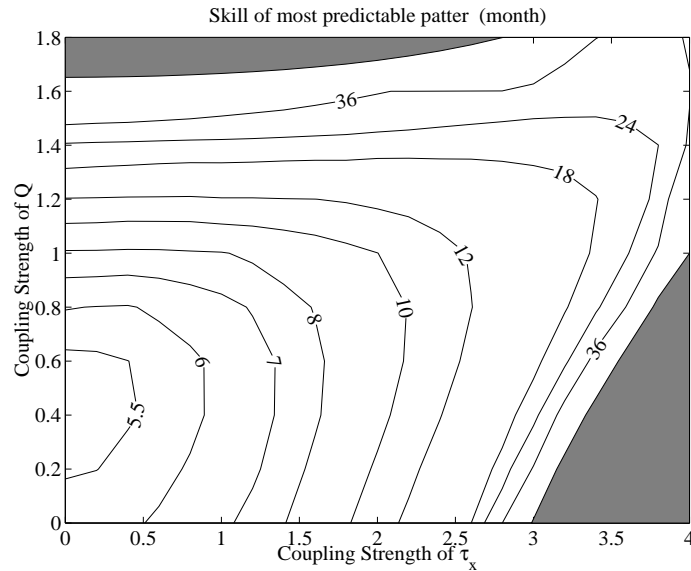


Fig. 33. Skill of most predictable pattern as function of coupling strength. The lead time is given by  $\varepsilon(\tau_m) = 0.5$

Fig. 34 and Fig. 35 show the most predictable patterns for realistic coupling ( $\mu = 1, \nu = 1$ ) and strong dynamical coupling ( $\mu = 2, \nu = 0.4$ ), respectively. These two cases have similar predictability and are chosen to represent the meridional-mode dominate versus equatorial-mode dominate regimes. For very short lead times, the predictable variance is confined to the eastern equatorial Atlantic with a maximum along south Africa coast. This initial similarity is not a surprising result because the stochastic forcing remains the same in both cases, and the predictable component at short lead times is closely related to the forcing pattern. This can be rigorously



demonstrated by the following mathematical argument. Assuming  $\tau$  small, we have

$$\begin{aligned}
\mathbf{C}_\tau &= e^{\mathbf{A}\tau} \mathbf{C} e^{\mathbf{A}^T \tau} \\
&= (\mathbf{I} + \mathbf{A}\tau + \dots) \mathbf{C} (\mathbf{I} + \mathbf{A}^T \tau + \dots)^T \\
&\approx \mathbf{C} + (\mathbf{A}\mathbf{C} + \mathbf{C}\mathbf{A}^T) \tau \\
&= \mathbf{C} - \Sigma \tau
\end{aligned} \tag{4.15}$$

where Lyapunov equation (2.9) is used, and the covariance of signal  $\mathbf{C}_\tau$  is defined in (2.24). Using definition (2.36), the predictable component is found through an equivalent eigenvalue problem

$$\Sigma \mathbf{u} = \gamma \mathbf{C} \mathbf{u}.$$

If the coupling, hence nonnormality, is small, then the predictable component will be largely determined by the forcing pattern. We suspect this forcing at the equator comes from the Pacific as suggested by others (Zebiak, 1993; Ruiz-Barradas et al., 2000). For longer lead times, the most predictable pattern resembles the first normal mode. In the thermodynamic regime, this would be a dipole-like pattern. In the dynamic regime, this is similar to the ENSO-like equatorial mode. Between these two lead-time limits, the most predictable pattern exhibits a mixed character. For example, in the dynamic regime, a signal begins to develop along the coast of south Africa, and a large structure of signal off the north Brazil coast extrudes eastward along the equator. At the same time, there is a wide center-of-action at  $10^\circ\text{S}$ , which gradually diminishes away as lead time increases. Comparing Fig. 35 with Fig. 25, we see a similar behavior of the growth, maturity, and decay of equatorial signal with comparable timescale. On the contrary, due to its decadal nature, the meridional mode (Fig. 24) exhibits less dramatic change within the period of our interest ( $\sim 1$  year). Thus, in the thermodynamic regime the predictable component behaves more

like a standing pattern.

With above results, we conclude that the most predictable pattern in the tropical Atlantic generally can be thought of as a superposition of the equatorial mode and the meridional mode with different phases.

## G. Summary

Tropical Atlantic variability is studied using a linear stochastic climate model. The deterministic components, obtained by linearizing an intermediate coupled model (ICM), include dynamics of thermocline governed by the linear shallow water equation, thermodynamics and Ekman dynamics of the mixed layer, plus the positive feedbacks of wind stress–SST and heat flux–SST. The random component is introduced through the atmospheric stochastic forcing with fixed spatial pattern estimated from observations. In this model, the atmosphere is statistically represented by two parts: one that is tightly related to local SST and represents air-sea coupling, one that is independent of tropical Atlantic SST and denotes as stochastic forcing. Within such framework, the influence of remote forcing like ENSO on TAV can be modeled either through affecting coupling strength and structure or by directly changing the atmosphere internal variability.

For realistic coupling strength, the linear ICM contains two leading coupled modes: one is decadal oscillation with meridional structure in the southern and northern tropical Atlantic, and the other is interannual oscillation with zonal structure along the equator. The thermodynamical feedbacks between cross-equatorial winds, heat flux, and SST are responsible for the meridional mode, while the dynamical feedback between SST, zonal winds, thermocline depth, and upwelling are essential to the equatorial mode. Consistent with other studies of TAV, we identify the former as the

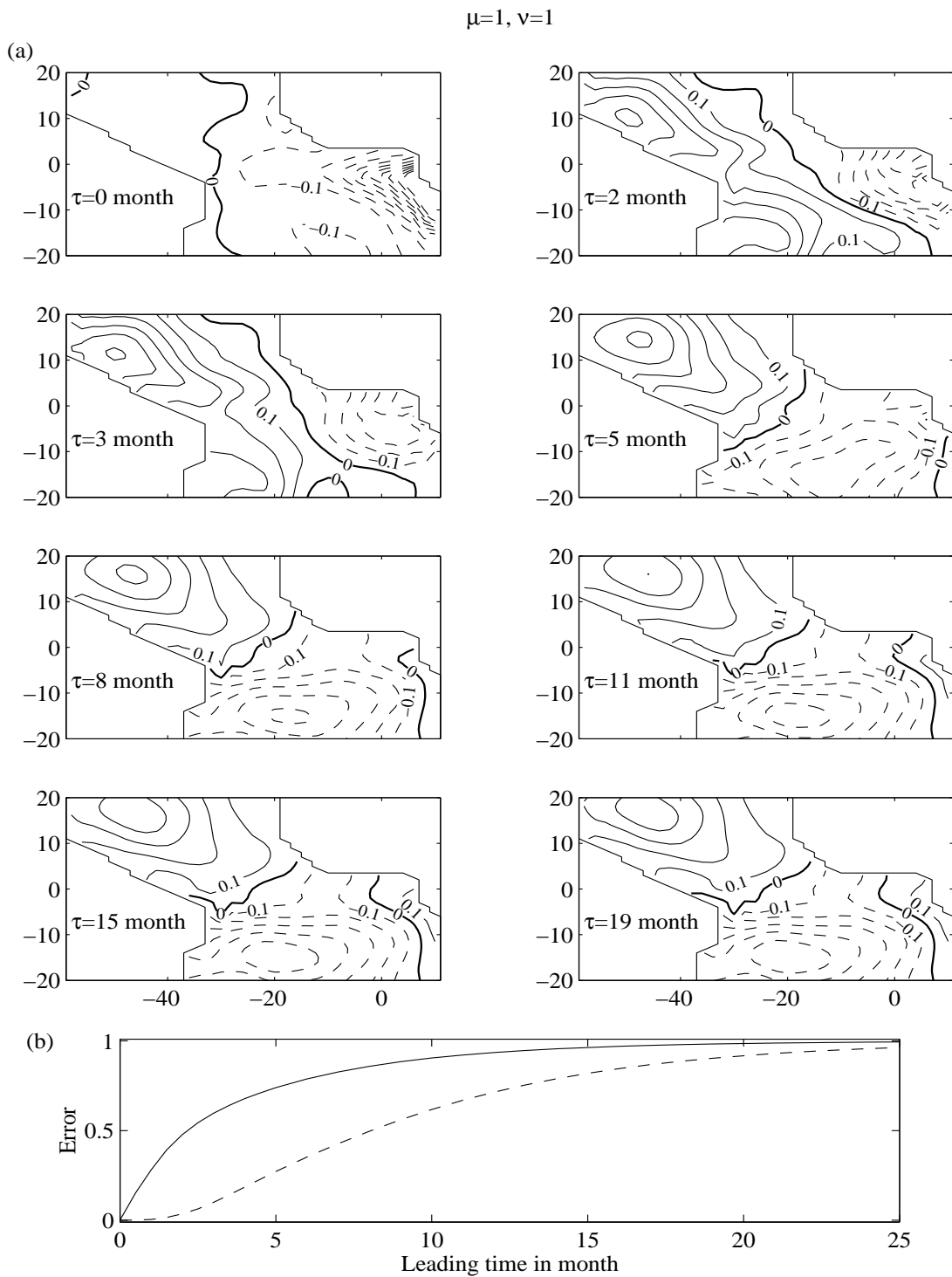


Fig. 34. Most predictable pattern for standard coupling ( $\mu = 1$ ,  $\nu = 1$ ). a) The evolution; b) the skill (dashed line) along with domain-averaged predictability (solid line).

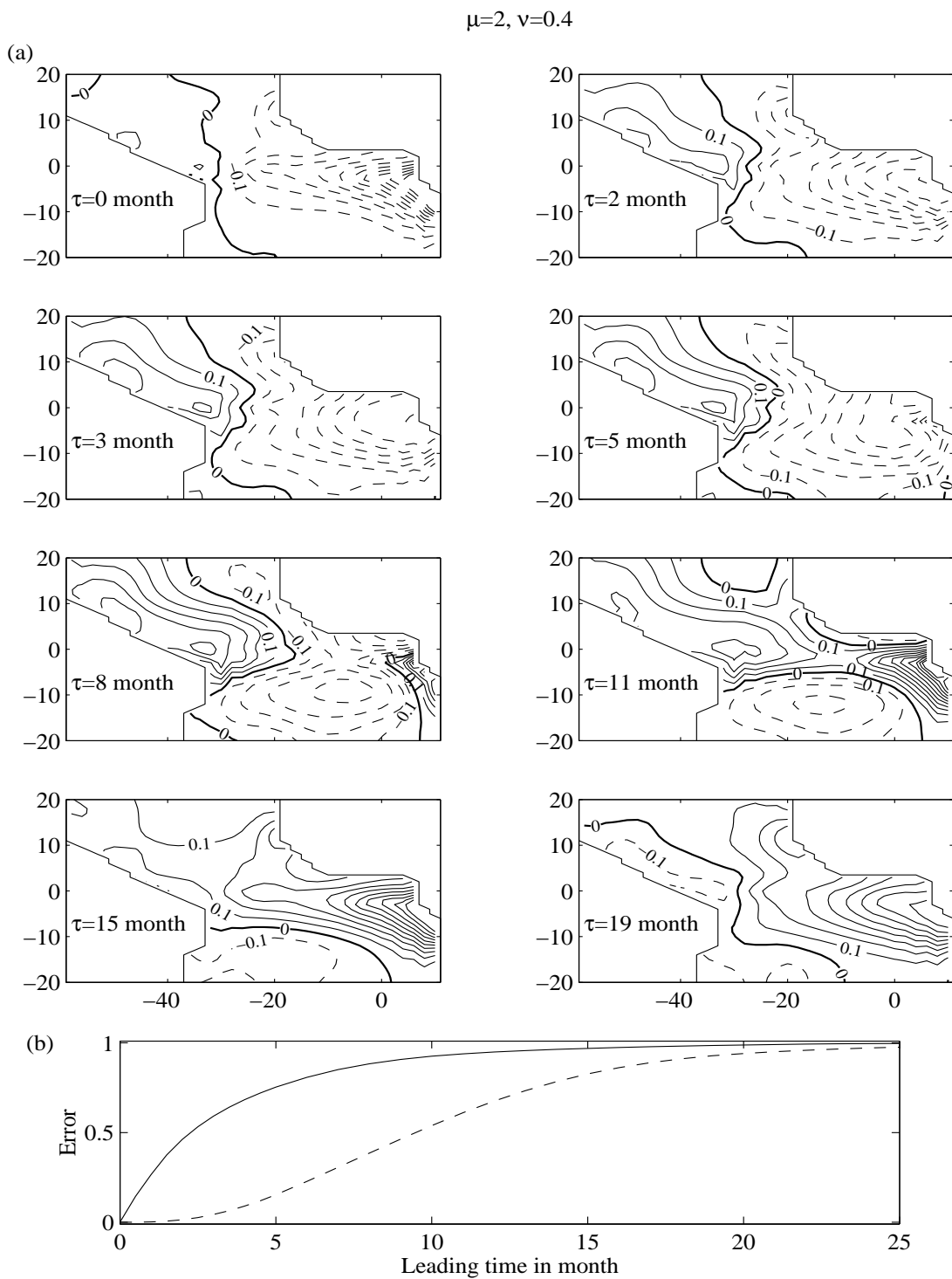


Fig. 35. Most predictable pattern for strong wind stress coupling ( $\mu = 2$ ,  $\nu = 0.4$ ).  
 a) The evolution; b) the skill (dashed line) along with domain-averaged predictability (solid line).

meridional mode and the latter as the Atlantic equatorial mode. The sensitivity of the meridional mode to coupling strength in our study sheds light on the debate on the Atlantic Dipole: it is close to a bifurcation point. If for some reason the thermodynamical coupling is weakened or the dynamical coupling is strengthened, the meridional mode goes through the 2-degeneracy process, in which it first loses its oscillatory nature and then its dipole character. When both coupling strengths are close to zero, neither meridional nor equatorial mode exists. In this regime, the ocean is dominated by free SST modes and basin modes, and the TAV is largely a passive response to atmospheric forcing, local and remote.

With coupling and stochastic forcing derived from observations, our model reproduces the TAV fairly well. The first two EOFs explain 50% of the total variance with Dipole and equatorial feature embodied. Therefore, it is possible in this case to reconstruct the physical modes of tropical Atlantic climate system based on the information of leading EOFs. Conventional correlation analysis is also carried out to illustrate the connection between the northern and southern tropical Atlantic. Despite the distinct dipole feature in physical and EOF modes, we found NTA and STA are not significantly correlated (cross-correlation 0.07). In our model, this is caused by the independence of forcing in NTA and STA. In reality, identifying the sources of forcing for the tropical Atlantic is a challenge.

With the tools developed in Chapter II, we further analyzed the predictable dynamics in the tropical Atlantic sector. In general, the tropical Atlantic SST only has 2 month predictability, which is considerably shorter than that of the tropical Pacific. This difference in predictability reflects the difference in dynamics. The tropical Pacific is dominated by ENSO which lies near the unstable regime. Hence, it behaves more like a self-sustained oscillation with less energy input from stochastic forcing. In contrast, the leading normal modes in the tropical Atlantic are highly damped,

and a large portion of the variability is associated with the midlatitude atmospheric internal variability that is essentially unpredictable. Because of the active role of the ocean in our model, however, there are certain SST features which can be predicted up to 8 months in advance. Once again, these features resemble the leading normal modes, i.e. the meridional anomaly at  $10^{\circ}\text{N}$  and  $10^{\circ}\text{S}$  and the zonal anomaly in east equatorial region. In fact, the predictability information of TAV can be roughly estimated just based on the damping rate of the meridional and equatorial mode.

In conclusion, we demonstrated that much of variability and predictability of tropical Atlantic are captured by two modes: meridional and equatorial. Of course, this does not say that atmospheric forcing from ENSO and NAO are negligible. On the contrary, it is this forcing that excites the first two leading normal modes of the tropical Atlantic and make them visible in TAV. In other words, the stochastic resonance discussed in Chapter III is the driving mechanism for what we saw about tropical Atlantic variability. Once again, how this occurs is pending on further investigation.

## CHAPTER V

## CONCLUSION AND FUTURE PROJECTS

## A. What's been done

In Chapter II, we constructed a framework to systematically analyze the variability and predictability of a linear, time-invariant, stochastic model. We found that the traditional EOF analysis can only be used under specific circumstances to reveal the underlying physical modes of the system. Usually, the final response is shaped by both deterministic dynamics and the structure of stochastic forcing, which is expressed as a fluctuation-dissipation relation. As to the predictability study, the use of singular vector and stochastic optimal analyses have similar problems. So, the concept of predictable pattern and a new set of optimal forcing are introduced to reconcile this. We have also shown that, as far as prediction and predictability are concerned, modal reduction performs poorly in reproducing the characteristics of the original full-order system. While the balanced truncation is the best choice of model reduction method, EOF reduction is a competitive one because of its easy use in practice. In many cases, the reduced-order model will overestimate the predictability of a system, which may contribute to an optimistic view of climate prediction. Finally, the various upper and lower bounds given in Chapter II illustrate the complicated role of nonnormality, which can either greatly enhance or reduce predictability in comparison to its normal counterpart.

In Chapter III, we considered the effect of mean ocean currents on the predictability of SST anomaly by using a stochastic advective ocean mixed-layer model. By solving the 1D model analytically, we found that advection does not change the predictability of SST when averaged over the ocean basin. In fact, the damping

rate, due to atmospheric heat flux and subsurface entrainment, is the controlling factor. Through predictable component analysis, we discovered that the mean advection transfers predictable variance downstream and causes certain areas to be more predictable than others. Using realistic parameters, the SST of the North Atlantic Ocean was modeled in similar way. We found that the overall predictability of SST anomalies is limited to 1–2 months, while the predictability over the western boundary region is about 5 months due to the strong influence of the ocean currents. Based on the magnitudes of the estimated damping rate and observed currents, we conclude that midlatitude climate variability essentially follows Hasselmann’s (1976) model even with the effect of ocean advection taken into account.

In Chapter IV, we addressed the issues central to tropical Atlantic variability with a linear intermediate coupled model. The ocean-atmosphere interactions in the Tropics give rise mainly to two types of modes: a decadal meridional dipole-SST mode due to WES feedback and an interannual equatorial mode in which SST-drive wind anomalies cause vertical displacements of the thermocline which in turn feed back to initial SST anomaly. When driven by observed stochastic weather forcing, variability of the North and South tropical Atlantic are not significantly correlated despite the existence of the physical dipole-mode. And the first two leading EOFs capture the main features of the two coupled modes. Another striking finding is that depending on the coupling strength, the meridional SST-mode can be a decadal oscillation with a dipole, two damped modes with asymmetric off-equator structures, and a century-long monopole oscillation. For realistic coupling strength, the tropical Atlantic variability on average has a 2 month predictability skill, whereas an 8 month skill is achievable if only the most predictable pattern is of interest. The most serious limitation of our linear intermediate model is the purely statistical nature of the atmosphere feedback, which does not allow a thorough understanding of processes



generating the dipole-mode. An intermediate dynamical atmosphere model may be used to solve this problem.

## B. What's ahead

1. Most climate phenomena are seasonal-dependent. For example, El Niño events tend to mature toward the end of the year, NAO is stronger during winter season, ITCZ locates in summer-hemisphere, etc. Therefore, as a logical next step the linear stochastic framework needs to be extended to a system with periodic dynamics

$$\frac{d\mathbf{x}}{dt} = \mathbf{A}(t)\mathbf{x} + \mathbf{F}(t)\boldsymbol{\xi} \quad (5.1)$$

where  $\mathbf{A}(t+T) = \mathbf{A}(t)$  and  $\mathbf{F}(t+T) = \mathbf{F}(t)$  are periodic functions in time,  $\mathbf{x}$  and  $\boldsymbol{\xi}$  are respectively the state variable and the white noise forcing. According to Floquet's theorem, the stability of a periodic system (5.1) is determined by the fundamental matrix

$$\Phi = \exp\left(\int_0^T \mathbf{A}(t)dt\right).$$

If all the eigenvalues of  $\Phi$  are within modulus less than one, then (5.1) is asymptotically stable. In other words, let  $\bar{\mathbf{A}}$  be the annual mean of the climatology  $\mathbf{A}(t)$

$$\bar{\mathbf{A}} = \frac{1}{T} \int_0^T \mathbf{A}(t)dt,$$

then the stability of  $\bar{\mathbf{A}}$  determines the stability of (5.1). This implies that the results from this dissertation basically hold even if the seasonal cycle were considered. Including seasonality, however, does introduce some new properties. For instance, the system can be stable (unstable) while  $\mathbf{A}(t)$  is unstable (stable) at any moment. Physically, the system may have an unstable mode every month and still produce a stationary response.

Farrell and Ioannou (1996b) have already discussed the generalized stability theory of a nonautonomous system, and Blumenthal (1991) and Thompson and Battisti (2000, 2001) have applied the Floquet analysis on ENSO. However, a framework like the one in Chapter II is yet to be established generally.

2. In midlatitude, the role of the ocean is more than just the influence of its mean circulation, and air-sea interactions may not be just negative local feedback either. This leads to a number of hypotheses on the mechanisms of midlatitude decadal variability, in addition to the advective resonance theory by Saravanan and McWilliams (1998). For example, using a simple midlatitude ocean-atmosphere model, Weng and Neelin (1999) and Neelin and Weng (1999) demonstrated that positive coupling can create an oscillatory interdecadal mode that involves westward Rossby wave propagation in the ocean and eastward atmospheric feedback in response to SST anomalies. Such a mode would be unstable for large coupling strength. Similarly, Goodman and Marshall (1999) formulated another analytical model of the middle-latitude atmosphere and ocean, and found decadal coupled modes that could be unstable for barotropic atmospheric feedback. By analyzing observations and output from GCM, Latif and Barnett (1994, 1996) identified active ocean-atmosphere interactions over the North Pacific and concluded that year-long climate forecasting is possible.

In the future, the question I would like to address is how these various mechanisms affect the predictability of SST for a realistic parameter range. Throughout this dissertation it has been demonstrated that existence of a decadal mode has little effect on predictability. As far as climate prediction is concerned, the lesson is that we should look for processes contributing to the persistence of SST instead of potential decadal modes.

3. In Chapter IV, we assume the primary influence from ENSO to be white noise, which is not true even in a moderate sense. If we separate the atmospheric forcing of tropical Atlantic into two parts, ENSO and NAO, then the governing equation can be written as

$$\frac{d\mathbf{x}_1}{dt} = \mathbf{A}_1\mathbf{x}_1 + \mathbf{f} + \boldsymbol{\zeta}_1 \quad (5.2)$$

where  $\mathbf{x}_1$  represents TAV,  $\mathbf{f}$  denotes impacts from ENSO,  $\boldsymbol{\zeta}_1$  is the atmospheric internal variability from NAO, and operator  $\mathbf{A}_1$  includes local air-sea feedback and ocean dynamics. Let  $\mathbf{x}_2$  be the ENSO variability of tropical Pacific, then  $\mathbf{f} = \mathbf{B}\mathbf{x}_2$  via atmosphere bridge  $\mathbf{B}$  from Pacific to Atlantic. Similarly, ENSO dynamics is described by

$$\frac{d\mathbf{x}_2}{dt} = \mathbf{A}_2\mathbf{x}_2 + \mathbf{g} + \boldsymbol{\zeta}_2 \quad (5.3)$$

where  $\mathbf{g}$  represents the influence from other oceans, which is set to zero in traditional ENSO theory. For the sake of completeness, let  $\mathbf{g} = \mathbf{L}\mathbf{x}_1$  be the Atlantic-to-Pacific bridge, then we have a coupled model of two tropical oceans and one atmosphere

$$\frac{d\mathbf{x}}{dt} = \mathbf{A}\mathbf{x} + \boldsymbol{\zeta} \quad (5.4)$$

where

$$\mathbf{x} = \begin{pmatrix} \mathbf{x}_1 \\ \mathbf{x}_2 \end{pmatrix}, \quad \mathbf{A} = \begin{pmatrix} \mathbf{A}_1 & \mathbf{B} \\ \mathbf{L} & \mathbf{A}_2 \end{pmatrix}, \quad \text{and } \boldsymbol{\zeta} = \begin{pmatrix} \boldsymbol{\zeta}_1 \\ \boldsymbol{\zeta}_2 \end{pmatrix} \quad (5.5)$$

Despite its linear nature, we believe the global coupled model (5.5) is able to capture the essential physics of tropical climate. Once the model is formulated, many interesting questions can be answered. What are the influences of other oceans on the ENSO cycle, negligible or substantial? If the dipole mode of TAV is triggered by ENSO, then can we view both as two components of one global

coupled mode? How about the Indian Ocean dipole mode? In terms of predictability and variability, what are the roles of atmospheric internal variability at a global level, and regional level? And many more.

## REFERENCES

- Achatz, U., and G. Branstator, 1999: A two-layer model with empirical linear corrections and reduced order for studies of internal climate variability. *J. Atmos. Sci.*, **56**, 3140–3160.
- Achatz, U., and G. Schmitz, 1997: On the closure problem in the reduction of complex atmospheric models by PIPs and EOFs: A comparison for the case of a two-layer model with zonally symmetric forcing. *J. Atmos. Sci.*, **54**, 2452–2474.
- Alexander, M. A., I. Bladé, M. Newman, J.R. Lanzante, N.C. Lau, and J.D. Scott, 2002: The atmospheric bridge: The influence of ENSO teleconnections on air-sea interaction over the global oceans. *J. Climate*, **15**, 2205–2231.
- Alexander, M. A., C. Deser, and M. S. Timlin, 1999: The reemergence of SST anomalies in the north Pacific Ocean. *J. Climate*, **12**, 2419–2433.
- Alexander, M. A., and C. Penland, 1996: Variability in a mixed layer ocean model driven by stochastic atmospheric forcing. *J. Climate*, **9**, 2424–2442.
- Anderson, E., Z. Bai, C. Bischof, S. Blackford, J. Demmel, J. Dongarra, J. Du Croz, A. Greenbaum, S. Hammarling, A. McKenney, and D. Sorensen, 2000: *LAPACK Users' Guide*. 3rd ed., SIAM, 407 pp.
- Antoulas, A. C., and D. C. Sorensen, 2001: Approximation of large-scale dynamical systems: An overview. Tech. rep., Department of Electrical and Computer Engineering, Rice University, Houston, TX, 22 pp.
- Baquero-Bernal, A., M. Latif, and S. Legutke, 2002: On dipolelike variability of sea surface temperature in the tropical Indian ocean. *J. Climate*, **15**, 1358–1368.
- Barsugli, J. J., and D. S. Battisti, 1998: The basic effects of atmosphere-ocean thermal coupling on midlatitude variability. *J. Atmos. Sci.*, **55**, 477–493.
- Battisti, D. S., 1988: The dynamics and thermodynamics of a warming event in a coupled tropical atmosphere/ocean model. *J. Atmos. Sci.*, **45**, 2889–2919.
- Battisti, D. S., and A. C. Hirst, 1989: Interannual variability in the tropical atmosphere-ocean system: Influence of the basic state, ocean geometry, and nonlinearity. *J. Atmos. Sci.*, **46**, 1687–1712.
- Benner, P., V. Mehrmann, V. Sima, S. Van Huffel, and A. Varga, 1999: SLICOT - A subroutine library in systems and control theory. *Applied and Computational Control, Signals and Circuits*, B. N. Datta, Ed., Springer Verlag, 499–539.

- Bjerknes, J., 1969: Atmospheric teleconnections from the equatorial Pacific. *Mon. Weather. Rev.*, **97**, 163–172.
- Bladé, I., 1997: The influence of midlatitude ocean-atmosphere coupling on the low-frequency variability of a GCM. Part I: No tropical forcing. *J. Climate*, **10**, 2087–2106.
- Blumenthal, M. B., 1991: Predictability of a coupled ocean-atmosphere model. *J. Climate*, **4**, 766–784.
- Bretherton, C. S., and D. S. Battisti, 2000: An interpretation of the results from atmospheric general circulation models forced by the time history of the observed sea surface temperature distribution. *Geophys. Res. Lett.*, **27**, 767–770.
- Bretherton, C. S., C. Smith, and J. M. Wallace, 1992: An intercomparison of methods for finding coupled patterns in climate data. *J. Climate*, **5**, 541–560.
- Cane, M. A., and D. W. Moore, 1981: A note on low-frequency equatorial basin modes. *J. Phys. Ocean.*, **11**, 1578–1584.
- Cane, M. A., and S. E. Zebiak, 1985: A theory for El Niño and the Southern Oscillation. *Science*, **228**, 1084–1087.
- Carton, J. A., X. Cao, B. S. Giese, and A. M. Da Silva, 1996: Decadal and interannual SST variability in the tropical Atlantic ocean. *J. Phys. Oceanogr.*, **26**, 1165–1175.
- Cayan, D. R., 1992: Latent and sensible heat flux anomalies over the northern oceans: Driving the sea surface temperature. *J. Phys. Oceanogr.*, **22**, 859–881.
- Chang, P., 1994: A study of the seasonal cycle of sea surface temperature in the tropical Pacific Ocean using reduced gravity models. *J. Geophys. Res.*, **99**, 7725–7741.
- Chang, P., L. Ji, and H. Li, 1997: A decadal climate variation in the tropical Atlantic Ocean from thermodynamic air-sea interactions. *Nature*, **385**, 516–518.
- Chang, P., L. Ji, H. Li, and M. Flügel, 1996: Chaotic dynamics versus stochastic processes in El Niño-Southern Oscillation in coupled ocean-atmosphere models. *Physica D*, **98**, 301–320.
- Chang, P., L. Ji, and R. Saravanan, 2001: A hybrid coupled model study of tropical Atlantic variability. *J. Climate*, **14**, 361–390.
- Chang, P., R. Saravanan, T. DelSole, and F. Wang, 2003a: Predictability of linear coupled systems. Part I: Theoretical analysis. *J. Climate*, accepted.

Chang, P., R. Saravanan, L. Ji, and G. C. Hegerl, 2000: The effect of local sea surface temperatures on atmospheric circulation over the tropical Atlantic sector. *J. Climate*, **13**, 2195–2216.

Chang, P., R. Saravanan, F. Wang, and L. Ji, 2003b: Predictability of linear coupled systems. Part II: An application to a simple model of tropical Atlantic variability. *J. Climate*, accepted.

Chiang, J. C. H., Y. Kushnir, and A. Giannini, 2002: Deconstructing Atlantic Intertropical Convergence Zone variability: Influence of the local cross-equatorial sea surface temperature gradient and remote forcing from the eastern equatorial Pacific. *J. Geophys. Res.*, **107**, art. no. 4004.

Chiang, J. C. H., and A. H. Sobel, 2002: Tropical tropospheric temperature variations caused by ENSO and their influence on the remote tropical climate. *J. Climate*, **15**, 2616–2631.

Christoph, M., U. Ulbrich, J. M. Oberhuber, and E. Roeckner, 2000: The role of ocean dynamics of low-frequency fluctuations of the NAO in a coupled ocean-atmosphere GCM. *J. Climate*, **13**, 2536–2549.

Chung, C., S. Nigam, and J. Carton, 2002: SST-force surface wind variability in the tropical Atlantic: An empirical model. *J. Geophys. Res.*, **107**, art. no. 4244.

Coope, I. D., and P. F. Renaud, 2000: Trace inequalities with applications to orthogonal regression and matrix nearness problems. Tech. rep., Department of Mathematics & Statistics, University of Canterbury, New Zealand, 7 pp.

Cover, T. M., and J. A. Thomas, 1991: *Elements of Information Theory*. Wiley, 542 pp.

Czaja, A., and C. Frankignoul, 2002: Observed impact of Atlantic SST anomalies on the North Atlantic oscillation. *J. Climate*, **15**, 606–623.

Czaja, A., P. Van Der Vaart, and J. Marshall, 2002: A diagnostic study of the role of remote forcing in tropical Atlantic variability. *J. Climate*, **15**, 3280–3290.

D’Andrea, F., and R. Vautard, 2001: Extratropical low-frequency variability as a low dimensional problem. Part I: A simplified model. *Quart. J. Roy. Meteor. Soc.*, **127**, 1357–1375.

da Silva, A., A. C. Young, and S. Levitus, 1994: *Algorithms and Procedures. Vol. 1, Atlas of Surface Marine Data 1994*. NOAA Atlas NESDIS 6, 83 pp.

- DelSole, T., and P. Chang, 2003: Predictable component analysis, canonical correlation analysis, and autoregressive models. *J. Atmos. Sci.*, **60**, 409–416.
- Deser, C., M. A. Alexander, and M. S. Timlin, 2003: Understanding the persistence of sea surface temperature anomalies in midlatitudes. *J. Climate*, **16**, 57–72.
- Diaz, H. F., M. P. Hoerling, and J. K. Eischeid, 2001: ENSO variability, teleconnections and climate change. *Int. J. Climatol.*, **21**, 1845–1862.
- Dijkstra, H. A., and G. Burgers, 2002: Fluid dynamics of El Niño variability. *Annu. Rev. Fluid Mech.*, **34**, 531–558.
- Dommenget, D., and M. Latif, 2000: Interannual to decadal variability in the tropical Atlantic. *J. Climate*, **13**, 777–792.
- , 2002a: Analysis of observed and simulated SST spectra in the midlatitudes. *Climate Dyn.*, **19**, 277–288.
- , 2002b: A cautionary note on the interpretation of EOFs. *J. Climate*, **15**, 216–225.
- Dullerud, G. E., and F. Paganini, 2000: *A Course in Robust Control Theory: A Convex Approach*. Springer-Verlag, 440 pp.
- Eckart, C., and G. Young, 1936: The approximation of one matrix by another of lower rank. *Psychometrika*, **1**, 211–218.
- Enfield, D. B., and D. A. Mayer, 1997: Tropical Atlantic sea surface temperature variability and its relation to El Niño Southern Oscillation. *J. Geophys. Res.*, **102**, 929–945.
- Enfield, D. B., A. M. Mestas-Nuñez, D. A. Mayer, and L. Cid-Serrano, 1999: How ubiquitous is the dipole relationship in tropical Atlantic sea surface temperature. *J. Geophys. Res.*, **104**, 7841–7848.
- Farrell, B. F., and P. J. Ioannou, 1996a: Generalized stability theory. Part I: Autonomous operators. *J. Atmos. Sci.*, **53**, 2025–2040.
- , 1996b: Generalized stability theory. Part II: Non-autonomous operators. *J. Atmos. Sci.*, **53**, 2041–2053.
- , 2001a: Accurate low-dimensional approximation of the linear dynamics of fluid flow. *J. Atmos. Sci.*, **58**, 2771–2789.



- , 2001b: State estimation using a reduced-order Kalman filter. *J. Atmos. Sci.*, **58**, 3666–3680.
- Fedorov, A. V., and S. G. Philander, 2001: A stability analysis of tropical ocean-atmosphere interactions: Briding measurements and theory for El Niño. *J. Climate*, **14**, 3086–3101.
- Flügel, M., P. Chang, and C. Penland, 2003: The role of stochastic forcing in modulating ENSO predictability. *J. Climate*, Submitted.
- Frankignoul, C., 1985: Sea surface temperature anomalies, planetary waves and air-sea feedback in the middle latitudes. *Rev. Geophys.*, **23**, 357–390.
- , 1999: A caution note on the use of statistical atmospheric models in the middle latitudes: Comments on “decadal variability in the north pacific as simulated by a hybrid coupled model”. *J. Climate*, **12**, 1871–1872.
- Frankignoul, C., A. Czaja, and B. L’Heveder, 1998: Air-sea feedback in the north Atlantic and surface boundary conditions for ocean models. *J. Climate*, **11**, 2310–2324.
- Frankignoul, C., and K. Hasselmann, 1977: Stochastic climate models, Part II Application to sea-surface anomalies and thermocline variability. *Tellus*, **29**, 289–305.
- Frankignoul, C., and E. Kestenare, 2002: The surface heat flux feedback. Part I: Estimates from observations in the Atlantic and the North Pacific. *Climate dyn.*, **19**, 633–647.
- Gajić, Z., and M. Qureshi, 1995: *Lyapunov Matrix Equation in System Stability and Control*. Academic Press, 255 pp.
- Galanti, E., and E. Tziperman, 2000: ENSOs phase locking to the seasonal cycle in the fast-SST, fast-Wave, and mixed-mode regimes. *J. Atmos. Sci.*, **57**, 2936–2950.
- Giannini, A., M. A. Cane, and Y. Kushnir, 2001a: Interdecadal Changes in the ENSO Teleconnection to the Caribbean Region and the North Atlantic Oscillation. *J. Climate*, **14**, 2867–2879.
- Giannini, A., J. C. H. Chiang, M. A. Cane, Y. Kushnir, and R. Seager, 2001b: The ENSO teleconnection to the tropical Atlantic Ocean: Contributions of the remote and local SSTs to rainfall variability in the tropical Americas. *J. Climate*, **14**, 4530–4544.

- Goddard, L., S. J. Mason, S. E. Zebiak, C. F. Ropelewski, R. Basher, and M. A. Cane, 2001: Current approaches to seasonal-to-interannual climate predictions. *Int. J. Climatol.*, **21**, 1111–1152.
- Goodman, J., and J. Marshall, 1999: A model of decadal middle-latitude atmosphere-ocean coupled modes. *J. Climate*, **12**, 621–641.
- Graham, R. J., A. D. L. Evans, K. R. Mylne, M. S. J. Harrison, and K. B. Robertson, 2000: An assessment of seasonal predictability using atmospheric general circulation models. *Q. J. Roy. Meteor. Soc.*, **126**, 2211–2240.
- Greatbatch, R.J., 2000: The North Atlantic Oscillation. *Stochastic Environmental Research and Risk Assessment*, **14**, 213–242.
- Häkkinen, S., and K. C. Mo, 2002: The low-frequency variability of the tropical Atlantic ocean. *J. Climate*, **15**, 237–250.
- Hasselmann, K., 1976: Stochastic climate models: Part I. Theory. *Tellus*, **28**, 473–485.
- , 1988: PIPs and POPs: The reduction of complex dynamical systems using principal interaction and oscillation patterns. *J. Geophys. Res.*, **93**, 11 015–11 021.
- Hazeleger, W., and S. S. Drijfhout, 2000: Eddy subduction in a model of the subtropical gyre. *J. Phys. Oceanogr.*, **30**, 677–695.
- Herterich, K., and K. Hasselmann, 1987: Extraction of mixed layer advection velocities, diffusion coefficients, feedback factors and atmospheric forcing parameters from the statistical analysis of North Pacific SST anomaly fields. *J. Phys. Oceanogr.*, **17**, 2145–2156.
- Hoerling, M. P., J. W. Hurrell, and T. Xu, 2001: Tropical origins for recent North Atlantic climate change. *Science*, **292**, 90–92.
- Holmes, P., J. L. Lumley, and G. Berkooz, 1996: *Turbulence, Coherent Structures, Dynamical Systems and Symmetry*. Cambridge University Press, 420 pp.
- Horn, R. A., and C. R. Johnson, 1985: *Matrix Analysis*. Cambridge University Press, 561 pp.
- , 1991: *Topics in Matrix Analysis*. Cambridge University Press, 607 pp.
- Huffel, S.V., and J. Vandewalle, 1991: *The Total Least Squares Problem: Computational Aspects and Analysis*. SIAM, 300 pp.

- Hurrell, J. W., Y. Kushnir, G. Ottersen, and M. Visbeck, Eds., 2003: *The North Atlantic Oscillation: Climate Significance and Environmental Impact*, volume 134 of *Geophysical Monograph Series*. American Geophysical Union, 279 pp.
- Imkeller, P., and J. S. von Storch, 2001: *Stochastic Climate Models*. Birkhäuser Verlag, 398 pp.
- Ioannou, P. J., 1995: Nonnormality increases variance. *J. Atmos. Sci.*, **52**, 1155–1158.
- Jin, F. F., 1997a: An equatorial ocean recharge paradigm for ENSO. Part I: Conceptual model. *J. Atmos. Sci.*, **54**, 811–829.
- , 1997b: An equatorial ocean recharge paradigm for ENSO. Part II: A stripped-down coupled model. *J. Atmos. Sci.*, **54**, 830–847.
- , 2001: Low-frequency modes of tropical ocean dynamics. *J. Climate*, **14**, 3874–3881.
- Jin, F. F., and J. D. Neelin, 1993a: Modes of interannual tropical ocean-atmosphere interaction—a unified view. Part I: Numerical results. *J. Atmos. Sci.*, **50**, 3477–3503.
- , 1993b: Modes of interannual tropical ocean-atmosphere interaction—a unified view. Part III: Analytical results in fully coupled cases. *J. Atmos. Sci.*, **50**, 3523–3540.
- Jin, F. F., J. D. Neelin, and M. Ghil, 1994: El Niño on the devil’s staircase: Annual subharmonic steps to chaos. *Science*, **264**, 70–72.
- Johnson, S. D., D. S. Battisti, and E. S. Sarachik, 2000: Empirically derived Markov models and prediction of tropical Pacific sea surface temperature anomalies. *J. Climate*, **13**, 3–17.
- Kalnay, E., S. J. Lord, and B. D. McPherson, 1998: Maturity of operational numerical weather prediction: Medium range. *Bull. Amer. Meteor. Soc.*, **79**, 2753–2892.
- Kiehl, J. T., J. J. Hack, G. B. Bonan, B. A. Boville, D. L. Williamson, and P. J. Rasch, 1998: The National Center for Atmospheric Research Community Climate Model: CCM3. *J. Climate*, **11**, 1131–1160.
- Kleeman, R., 1993: On the dependence of hindcast skill on ocean thermodynamics in a coupled ocean-atmosphere model. *J. Climate*, **6**, 2012–2033.

- , 2002: Measuring dynamical prediction utility using relative entropy. *J. Atmos. Sci.*, **59**, 2057–2072.
- Kleeman, R., A. J. Majda, and I. Timofeyev, 2002: Quantifying predictability in a model with statistical features of the atmosphere. *P. Natl. Acad. Sci.*, **99**, 15291–15296.
- Kushnir, Y., W. A. Robinson, I. Bladé, N. M. J. Hall, S. Peng, and R. Sutton, 2002a: Atmospheric GCM response to extratropical SST anomalies: Synthesis and evaluation. *J. Climate*, **15**, 2233–2256.
- Kushnir, Y., R. Seager, J. Miller, and J. C. Chiang, 2002b: A simple coupled model of tropical Atlantic decadal climate variability. *Geophys. Res. Letter*, **29**, doi:10.1029/2002GL015874.
- Kwasniok, F., 1996: The reduction of complex dynamical systems using principal interaction patterns. *Physica D*, **92**, 28–60.
- , 1997: Optimal Galerkin approximations of partial differential equations using principal interaction patterns. *Phys. Rev. E*, **55**, 5365–5375.
- , 2001: Low-dimensional models of the Ginzburg-Landau equation. *SIAM J. Appl. Math.*, **61**, 2063–2079.
- Lall, S., J. E. Marsden, and S. Glavaški, 2002: A subspace approach to balanced truncation for model reduction of nonlinear control systems. *Int. J. Robust and Nonlinear Control*, **12**, 519–535.
- Latif, M., and T. P. Barnett, 1994: Cause of Decadal Climate Variability over the North Pacific and North America. *Science*, **266**, 634–637.
- , 1996: Decadal climate variability over the North Pacific and North America: Dynamics and predictability. *J. Climate*, **9**, 2407–2423.
- Leung, L. Y., and G. R. North, 1990: Information theory and climate prediction. *J. Climate*, **3**, 5–14.
- Levitus, S., 1982: *Climatological Atlas of the World Ocean*. NOAA Prof. Paper 13, 173 pp.
- Lohmann, G., and J. Schneider, 1999: Dynamics and predictability of Stommel’s box model: A phase space perspective with implications for decadal climate variability. *Tellus*, **51**, 326–336.
- Lorenz, E. N., 1963: Deterministic nonperiodic flow. *J. Atmos. Sci.*, **20**, 130–141.

- , 1965: A study of the predictability of a 28-variable atmospheric model. *Tellus*, **17**, 321–333.
- , 1969: The predictability of a flow which possesses many scales of motion. *Tellus*, **21**, 289–307.
- , 1984: Irregularity: A fundamental property of the atmosphere. *Tellus*, **36A**, 98–110.
- , 1993: *The Essence of Chaos*. University of Washington Press, 227 pp.
- Lütkepohl, H., 1993: *Introduction to Multiple Time Series Analysis*. 2nd ed., Springer-Verlag, 545 pp.
- Manabe, S., and R. J. Stouffer, 1996: Low-frequency variability of surface air temperature in a 1000-year integration of a coupled atmosphere-ocean-land surface model. *J. Climate*, **9**, 376–393.
- Marcus, M., and H. Minc, 1992: *A Survey of Matrix Theory and Matrix Inequalities*. reprint ed., Dover, 180 pp.
- Marshall, J., H. Johnson, and J. Goodman, 2001a: A study of the interaction of the North Atlantic Oscillation with ocean circulation. *J. Climate*, **14**, 1399–1421.
- Marshall, J., Y. Kushnir, D. Battisti, P. Chang, A. Czaja, R. Dickson, J. Hurrell, M. McCartney, R. Saravanan, and M. Visbeck, 2001b: North Atlantic climate variability: Phenomena, impacts and mechanisms. *Int. J. Climatol.*, **21**, 1863–1898.
- Marshall, J. C., A. J. G. Nurser, and R. G. Williams, 1993: Inferring the subduction rate and period over the North Atlantic. *J. Phys. Oceanogr.*, **23**, 1315–1329.
- Mehta, V. M., 1998: Variability of the tropical ocean surface temperatures at decadal-multidecadal timescales. Part I: The Atlantic Ocean. *J. Climate*, **11**, 2351–2375.
- Mehta, V. M., and T. Delworth, 1995: Decadal variability of the tropical Atlantic Ocean surface temperature in shipboard measurements and in a global ocean-atmosphere model. *J. Climate*, **8**, 172–190.
- Mirsky, L., 1960: Symmetric gauge functions and unitarily invariant norms. *Quart. J. Math.*, **11**, 50–59.

- Mo, K. C., and S. Häkkinen, 2001: Interannual variability in the tropical Atlantic and linkages to the Pacific. *J. Climate*, **14**, 2740–2762.
- Moore, A. M., and R. Kleeman, 1996: The dynamics of error growth and predictability in a coupled model of ENSO. *J. Climate*, **12**, 1199–1220.
- , 1999: Stochastic forcing of ENSO by the intraseasonal oscillation. *J. Climate*, **12**, 1199–1220.
- Moore, B. C., 1981: Principal component analysis in linear systems: Controllability, observability, and model reduction. *IEEE Trans. Autom. Control*, **AC-26**, 17–32.
- Munk, W. H., 1960: Smoothing and persistence. *J. Meteor.*, **17**, 92–93.
- Neelin, J. D., D. S. Battisti, A. C. Hirst, F.-F. Jin, Y. Wakata, T. Yamagata, and S. E. Zebiak, 1998: ENSO theory. *J. Geophys. Res.*, **103**, 14 261–14 290.
- Neelin, J. D., and F. F. Jin, 1993: Modes of interannual tropical ocean-atmosphere interaction—a unified view. Part II: Analytical results in the weak-coupling limit. *J. Atmos. Sci.*, **50**, 3504–3522.
- Neelin, J. D., and W. Weng, 1999: Analytical prototypes for ocean-atmosphere interaction at midlatitudes. Part I: Coupled feedbacks as a sea temperature dependent stochastic process. *J. Climate*, **12**, 697–721.
- Neumaier, A., and T. Schneider, 2001: Estimation of parameters and eigenmodes of multivariate autoregressive models. *ACM Transactions on Mathematical Software*, **27**, 27–57.
- Nobre, P., and J. Shukla, 1996: Variations of sea surface temperature, wind stress, and rainfall over the tropical Atlantic and South America. *J. Climate*, **10**, 2464–2479.
- Obinata, G., and B. D. O. Anderson, 2000: *Model Reduction for Control System Design*. Springer Verlag, 165 pp.
- Øksendal, B., 2000: *Stochastic Differential Equations: An Introduction With Application*. 5th ed., Springer, 326 pp.
- Ostrovskii, A. G., and L. I. Piterbarg, 2000: Inversion of upper ocean temperature time series for entrainment, advection and diffusivity. *J. Phys. Oceanogr.*, **30**, 201–214.
- Palmer, T. N., 2000: Predicting uncertainty in forecasts of weather and climate. *Rep. Prog. Phys.*, **63**, 71–116.

- Palmer, T. N., R. Gelaro, J. Barkmeijer, and R. Buizza, 1998: Singular vectors, metrics, and adaptive observations. *J. Atmos. Sci.*, **55**, 633–653.
- Patil, D. J., B. R. Hunt, E. Kalnay, J. A. Yorke, and E. Ott, 2001: Local low dimensionality of atmospheric dynamics. *Phys. Rev. Lett.*, **86**, 5878–5881.
- Pedlosky, J., 1987: *Geophysical Fluid Dynamics*. 2nd ed., Springer-Verlag, 710 pp.
- Penland, C., M. Flügel, and P. Chang, 2000: Identification of dynamical regimes in an intermediate coupled ocean-atmosphere model. *J. Climate*, **13**, 2105–2115.
- Penland, C., and M. Ghil, 1993: Forecasting Northern Hemisphere 700-mb geopotential height anomalies using empirical normal modes. *Mon. Wea. Rev.*, **121**, 2355–2372.
- Penland, C., and T. Magorian, 1993: Prediction of Niño 3 sea surface temperatures using linear inverse modeling. *J. Climate*, **6**, 1067–1076.
- Penland, C., and L. Matrosova, 1998: Prediction of Tropical Atlantic sea surface temperature using linear inverse modeling. *J. Climate*, **11**, 483–496.
- , 2001: Expected and actual errors of linear inverse model forecasts. *Mon. Wea. Rev.*, **129**, 1740–1745.
- Penland, C., and P. D. Sardeshmukh, 1995: The optimal growth of tropical sea surface temperature anomalies. *J. Climate*, **8**, 1999–2024.
- Philander, S. G., 1990: *El Niño, La Niña, and the Southern Oscillation*. Academic Press, 293 pp.
- Preisendorfer, R. W., 1988: *Principal Component Analysis in Meteorology and Oceanography*. Elsevier, 425 pp.
- Roulston, M. S., and J. D. Neelin, 2000: The response of an ENSO model to climate noise, weather noise and intraseasonal forcing. *Geophys. Res. Lett.*, **27**, 3723–3726.
- Ruiz-Barradas, A., J. A. Carton, and S. Nigam, 2000: Structure of interannual-to-decadal climate variability in the tropical Atlantic sector. *J. Climate*, **13**, 3285–3297.
- Samuels, B., and M. D. Cox, 1987: *Data Set Atlas for Oceanographic Modeling*, volume 1. Ocean Modeling, 40 pp.

- Saravanan, R., 1998: Atmospheric low-frequency variability and its relationship to midlatitude SST variability: Studies using the NCAR climate system model. *J. Climate*, **11**, 1386–1404.
- Saravanan, R., and P. Chang, 2000: Interaction between tropical Atlantic variability and El Niño-Southern Oscillation. *J. Climate*, **13**, 2177–2194.
- Saravanan, R., and J. C. McWilliams, 1998: Advective ocean-atmosphere interaction: An analytical stochastic model with implications for decadal variability. *J. Climate*, **11**, 165–188.
- Schneider, T., and S. M. Griffies, 1999: A conceptual framework for predictability studies. *J. Climate*, **12**, 3133–3155.
- Scott, R. B., 2003: Predictability of SST in an idealized one-dimensional, coupled atmosphere-ocean climate model with stochastic forcing and advection. *J. Climate*, **16**, 323–335.
- Seager, R., M. B. Blumenthal, and Y. Kushnir, 1995: An advective atmospheric mixed layer model for ocean modeling purposes: Global simulation of surface heat fluxes. *J. Climate*, **8**, 1951–1964.
- Seager, R., Y. Kushnir, P. Chang, N. Naik, J. Miller, and W. Hazeleger, 2001: Looking for the role of the ocean in tropical Atlantic decadal climate variability. *J. Climate*, **14**, 638–655.
- Seager, R., Y. Kushnir, M. Visbeck, N. Naik, J. Miller, G. Krahnemann, and H. Gullen, 2000: Cause of Atlantic ocean climate variability between 1958 and 1998. *J. Climate*, **13**, 2845–2862.
- Seager, R., S. E. Zebiak, and M. A. Cane, 1988: A model of the tropical Pacific sea surface temperature climatology. *J. Geophys. Res.*, **93**, 1265–1280.
- Selten, F. M., 1995: An efficient description of the dynamics of barotropic flow. *J. Atmos. Sci.*, **52**, 915–936.
- , 1997: Baroclinic empirical orthogonal functions as basis functions in an atmospheric model. *J. Atmos. Sci.*, **54**, 2099–2114.
- Servain, J., 1991: Simple climatic indices for the tropical Atlantic Ocean and some applications. *J. Geophys. Res.*, **96**, 15137–15146.
- Servain, J., I. Wainer, H. L. Ayina, and H. Roquet, 2000: The relationship between the simulated climatic variability modes of the tropical Atlantic. *Int. J. Climatology*, **20**, 939–953.



- Shannon, C. E., 1948: A mathematical theory of communication. *Bell Syst. Tech.*, **27**, 379–423, 623–656.
- Solomon, A., J. P. McCreary, R. Kleeman, and B. A. Klinger, 2003: Interannual and decadal variability in an intermediate coupled model of the Pacific Region. *J. Climate*, **16**, 383–405.
- Suarez, M. J., and P. S. Schopf, 1988: A delayed action oscillator for ENSO. *J. Atmos. Sci.*, **45**, 3283–3287.
- Sutton, R. T., and M. R. Allen, 1997: Decadal predictability of North Atlantic sea surface temperature and climate. *Nature*, **388**, 563–567.
- Sutton, R. T., S. P. Jewson, and D. P. Rowell, 2000: The elements of climate variability in the tropical Atlantic region. *J. Climate*, **13**, 3261–3284.
- Syu, H. H., and J. D. Neelin, 1995: Seasonal and interannual variability in a hybrid coupled GCM. *J. Climate*, **8**, 2121–2143.
- Tanimoto, Y., and S. P. Xie, 2002: Inter-hemispheric decadal variations in SST, surface wind, heat flux and cloud cover over the Atlantic Ocean. *J. Meteor. Soc. Japan*, **80**, 1199–1219.
- Thompson, C. J., and D. S. Battisti, 2000: A linear stochastic dynamical model of ENSO. Part I: Model development. *J. Climate*, **13**, 2818–2832.
- , 2001: A linear stochastic dynamical model of ENSO. Part II: Analysis. *J. Climate*, **14**, 445–466.
- Timmermann, A., H. U. Voss, and R. Pasmanter, 2001: Empirical dynamical system modeling of ENSO using nonlinear inverse techniques. *J. Phys. Oceanogr.*, **31**, 1579–1598.
- Tippett, M. K., and P. Chang, 2003: Some theoretical considerations on predictability of linear stochastic dynamics. *Tellus*.
- Toure, Y. M., Rajagopalan B, and Kushnir Y, 1999: Dominant patterns of climate variability in the Atlantic Ocean during the last 136 years. *J. Climate*, **12**, 2285–2299.
- Trefethen, L. N., 1992: Pseudospectra of matrices. *Numerical Analysis 1991*, G. D. F. and G. A. Watson, Eds., Longman Scientific and Technical, Harlow, Essex, UK, 234–266.
- , 1997: Pseudospectra of linear operators. *SIAM Rev.*, **39**, 383–406.

- , 1999: Computation of Pseudospectra. *Acta Numerica*, **8**, 300–330.
- Trefethen, L. N., A. E. Trefethen, S. C. Reddy, and T. A. Driscoll, 1993: Hydrodynamic stability without eigenvalues. *Science*, **261**, 578–584.
- Tziperman, E., M. A. Cane, and S. E. Zebiak, 1995: Irregularity and locking to the seasonal cycle in an ENSO prediction model as explained by the quasi-periodicity route to chaos. *J. Atmos. Sci.*, **50**, 293–306.
- Tziperman, E., L. Stone, S. E. Zebiak, and H. Jarosh, 1994: El Niño chaos: Overlapping of resonances between the seasonal cycle and the Pacific ocean-atmosphere oscillator. *Science*, **264**, 72–74.
- Wallace, J. M., C. Smith, and Q. Jiang, 1990: Spatial patterns of atmosphere-ocean interaction in the northern winter. *J. Climate*, **3**, 990–998.
- Wang, B., T. Li, and P. Chang, 1995: An intermediate model of the tropical Pacific Ocean. *J. Phys. Oceanogr.*, **25**, 1599–1616.
- Wang, R., 2001: Prediction of seasonal climate in a low-dimensional phase space derived from the observed SST forcing. *J. Climate*, **14**, 77–97.
- Watanabe, M., and M. Kimoto, 2000: On the persistence of decadal SST anomalies in the North Atlantic. *J. Climate*, **13**, 3017–3028.
- Weng, W., and J. D. Neelin, 1999: Analytical prototypes for ocean-atmosphere interaction at midlatitudes. Part II: Mechanisms for coupled gyre modes. *J. Climate*, **12**, 2757–2774.
- Winkler, C. R., M. Newman, and R. D. Sardeshmukh, 2001: A linear model of wintertime low-frequency variability. Part I: Formulation and forecast skill. *J. Climate*, **14**, 4474–4494.
- Xie, S. P., 1999: A dynamic ocean-atmosphere model of the tropical Atlantic decadal variability. *J. Climate*, **12**, 64–70.
- Xue, Y., M. A. Cane, S. E. Zebiak, and M. B. Blumenthal, 1994: On the prediction of ENSO: A study with a low-order Markov model. *Tellus*, **46A**, 512–528.
- Zebiak, S., 1993: Air-sea interaction in the equatorial Atlantic region. *J. Climate*, **6**, 1567–1586.
- Zebiak, S. E., and M. A. Cane, 1987: A model El Niño—Southern Oscillation. *Mon. Wea. Rev.*, **115**, 2262–2278.

Zhang, Y., and I. M. Held, 1999: A linear stochastic model of a GCM's mid-latitude storm tracks. *J. Atmos. Sci.*, **56**, 3416–3435.

Zhou, Z., and J. A. Carton, 1998: Latent heat flux and interannual variability of the coupled atmosphere-ocean system. *J. Atmos. Sci.*, **55**, 494–501.

## APPENDIX A

## STOCHASTIC FORCING IS RED NOISE

Consider a 1-D red noise forced process

$$\frac{dx}{dt} = ax + \eta, \quad (\text{A.1})$$

where  $x$  is a scalar-valued function (for example salinity at a fixed point) and

$$E[\eta(t)] = 0 \quad \text{and} \quad E[\eta(t)\eta(s)] = \frac{\sigma^2}{2\alpha} e^{-\alpha(t-s)}. \quad (\text{A.2})$$

With little modification, the linear stochastic framework in Chapter 2 can be applied to this case too:<sup>1</sup>

The solution of Eq. (A.1) under initial condition  $x_{t_0}$  is

$$x_{(t+t_0)} = x_{(t_0)} e^{a(t-t_0)} + \int_{t_0}^t e^{a(t-s)} \eta(s) ds. \quad (\text{A.3})$$

Assuming system stable ( $a < 0$ ),  $x$  describe a real stationary process with mean  $E[x] = 0$  and correlation

$$\begin{aligned} c(\tau) &= E[x_{(t)} x_{(t+\tau)}] \\ &= E \left[ \int_{-\infty}^t e^{a(t-s_1)} \eta_{(s_1)} ds_1 \int_{-\infty}^{t+\tau} e^{a(t+\tau-s_2)} \eta_{(s_2)} ds_2 \right] \\ &= e^{a(2t+\tau)} \int_{-\infty}^t \int_{-\infty}^{t+\tau} e^{-a(s_1+s_2)} E[\eta_{(s_1)} \eta_{(s_2)}] ds_1 ds_2 \\ &\text{using (A.2)} \quad = \frac{\sigma^2}{2\alpha} e^{a(2t+\tau)} \int_{-\infty}^t \int_{-\infty}^{t+\tau} e^{-a(s_1+s_2)} e^{-\alpha|s_1-s_2|} ds_1 ds_2 \\ &= \frac{\sigma^2}{2(a+\alpha)(a-\alpha)} \left( \frac{e^{-\alpha\tau}}{\alpha} + \frac{e^{a\tau}}{a} \right) > 0. \end{aligned} \quad (\text{A.4})$$

---

<sup>1</sup>This is a question asked by Dr. Panetta during the preliminary examination. Listed is my answer.

Some interesting limits

$$E[x(t)x_{(t+\tau)}] = \begin{cases} \frac{\sigma^2}{-2a\alpha^2} e^{a\tau} & \alpha \gg -a \\ \frac{\sigma^2}{4\alpha^2} e^{-\alpha\tau} \left(\tau + \frac{1}{\alpha}\right) & \alpha = -a \\ \frac{\sigma^2}{2\alpha a^2} e^{-\alpha\tau} & \alpha \ll -a \end{cases}, \quad (\text{A.5})$$

where  $\alpha \gg -a$  is a slow system perturbed by fast forcing — white noise limit;  $\alpha \ll -a$  is the case that system instantaneously responds to a slow-forcing;  $\alpha = -a$  is the intermediate case.

If the same prediction scheme were used

$$\hat{x}_{(t+t_0)} = x_{(t_0)} e^{a(t-t_0)}, \quad (\text{A.6})$$

from Eq. (A.3) we know the prediction error would be

$$\begin{aligned} \epsilon_{(t,t_0)}^2 &= \epsilon_{(\tau)}^2 \\ &= E \left[ \int_{t_0}^t e^{a(t-s_1)} \eta_{(s_1)} ds_1 \int_{t_0}^t e^{a(t-s_2)} \eta_{(s_2)} ds_2 \right] \\ &= \frac{\sigma^2}{2\alpha} e^{2at} \int_{t_0}^t \int_{t_0}^t e^{-a(s_1+s_2)} e^{-\alpha|s_1-s_2|} ds_1 ds_2 \\ &= \frac{\sigma^2}{2(a+\alpha)(a-\alpha)} \left[ \frac{1-e^{2a\tau}}{a} + \frac{1-2e^{(a-\alpha)\tau} + e^{2a\tau}}{\alpha} \right] > 0, \end{aligned} \quad (\text{A.7})$$

where  $\tau = t - t_0$  is the leading time. When normalized by the variance, it measures the skill of such prediction  $\hat{x}_{(\tau)}$

$$\begin{aligned} \rho_{(\tau)} &= \frac{\epsilon_{\tau}^2}{c_0} \\ &= 1 - \frac{\frac{e^{2a\tau}}{a} + \frac{2e^{(a-\alpha)\tau} - e^{2a\tau}}{\alpha}}{\frac{1}{a} + \frac{1}{\alpha}}. \end{aligned} \quad (\text{A.8})$$

Again, three limits exist

$$\rho(\tau) = \begin{cases} (1 - e^{a\tau})^2 & \alpha \ll -a \\ 1 - (1 - 2a\tau)e^{2a\tau} & \alpha = -a \\ 1 - e^{2a\tau} & \alpha \gg -a \end{cases} . \quad (\text{A.9})$$

However, prediction given by (A.6) is not optimal in the sense that a better prediction skill may be achievable. The problem or the advantage is the red noised forcing assumption. Therefore, the Markov property does not apply here,

$$E[x_{(\tau+t_0)}|x_{t_0}, x_{t_1}, x_{t_2}, \dots, x_{t_n}] \neq E[x_{(\tau+t_0)}|x_{t_0}] \neq \hat{x}_{(t_0+\tau)} \quad (\text{A.10})$$

where  $t_0 > t_1 > t_2 > \dots > t_n$  and  $\tau > 0$ . In fact, from left to right, the prediction is getting worse. The reason is that forcing is correlated, so the information from the past can be used to improve the prediction of the future. Of course, in order to utilize such resource, we need more than just the first two moments of  $\eta$ .

Although mathematically problematic, in practice it is reasonable to assume the red noise (A.2) is generated by white noise, s.t.

$$\frac{d\eta}{dt} = -\alpha\eta + \xi \quad (\text{A.11})$$

where  $E[\xi(t)] = 0$  and  $E[\xi(t)\xi(s)] = \sigma^2\delta(t - s)$ . Then, (A.1) and (A.11) form a two-dimensional model just as in my proposal

$$\frac{d\boldsymbol{\theta}}{dt} = \mathbf{A}\boldsymbol{\theta} + \boldsymbol{\zeta} \quad (\text{A.12})$$

where

$$\boldsymbol{\theta} = \begin{pmatrix} x \\ \eta \end{pmatrix}; \quad \mathbf{A} = \begin{pmatrix} a & 1 \\ 0 & -\alpha \end{pmatrix}; \quad \boldsymbol{\zeta} = \begin{pmatrix} 0 \\ \xi \end{pmatrix}.$$

The optimal prediction of (A.12) is

$$\hat{\boldsymbol{\theta}} = e^{\mathbf{A}\tau}\boldsymbol{\theta}_0 = \begin{pmatrix} e^{a\tau}x_0 + \frac{e^{a\tau}-e^{-\alpha\tau}}{a+\alpha}\eta_0 \\ e^{-\alpha\tau}\eta_0 \end{pmatrix}. \quad (\text{A.13})$$

The covariance

$$\begin{aligned} \mathbf{C}_0 &= E[\boldsymbol{\theta}_{t_0} \boldsymbol{\theta}_{t_0}^T] \\ &= \frac{\sigma^2}{2\alpha} \begin{pmatrix} \frac{1}{a(a-\alpha)} & \frac{1}{\alpha-a} \\ \frac{1}{\alpha-a} & 1 \end{pmatrix}. \end{aligned} \quad (\text{A.14})$$

And the lagged covariance matrix

$$\begin{aligned} \mathbf{C}_\tau &= E[\boldsymbol{\theta}_{(t_0)} \boldsymbol{\theta}_{(t_0+\tau)}^T] \\ &= e^{\mathbf{A}\tau} \mathbf{C}_0 e^{\mathbf{A}^T \tau} \\ &= \frac{\sigma^2}{2\alpha} \begin{pmatrix} \frac{a\alpha(e^{a\tau}-e^{-\alpha\tau})^2 - (ae^{-\alpha\tau} + \alpha e^{a\tau})^2}{a(\alpha-a)(a+\alpha)^2} & \frac{(a-\alpha)e^{-2\alpha\tau} + 2\alpha e^{(a-\alpha)\tau}}{(\alpha+a)(\alpha-a)} \\ \frac{(a-\alpha)e^{-2\alpha\tau} + 2\alpha e^{(a-\alpha)\tau}}{(\alpha+a)(\alpha-a)} & e^{-2\alpha\tau} \end{pmatrix}. \end{aligned} \quad (\text{A.15})$$

As usual, the predictability of  $\eta$  is

$$\gamma_\eta = \frac{\mathbf{C}_\tau(2,2)}{\mathbf{C}_0(2,2)} = e^{-2\alpha\tau}. \quad (\text{A.16})$$

And the predictability of  $x$  can be defined as following

$$\begin{aligned} \gamma_x &= \frac{\mathbf{C}_\tau(1,1)}{\mathbf{C}_0(1,1)} \\ &= \frac{(ae^{-\alpha\tau} + \alpha e^{a\tau})^2 - a\alpha(e^{a\tau} - e^{-\alpha\tau})^2}{(a+\alpha)^2}. \end{aligned} \quad (\text{A.17})$$

Comparison between (A.8) and (A.17) shows that

$$\rho(\tau) > 1 - \gamma_x(\tau).$$

This means the prediction error of (A.13) is smaller than that of (A.6). Actually, prediction (A.13) is the best, and that is why we define its skill as predictability.

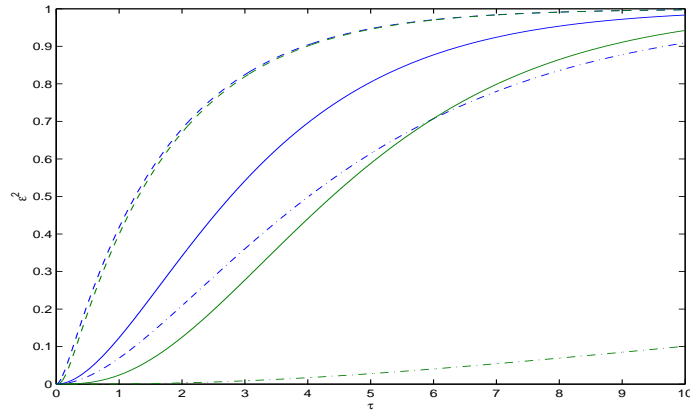


Fig. 36. Normalized error variance of different prediction schemes ( $a = -0.3$ ): Green line, “red prediction”  $1 - \gamma_\tau$ ; blue line, “white prediction”  $\rho_\tau$ . Dashed line,  $b = 10$ ; solid line,  $b = 0.31$ ; dash-dotted line,  $b = 0.01$

Once again, three limits exist for  $\gamma_x$ :

$$\gamma_x = \begin{cases} e^{-2\alpha\tau} & \alpha \ll -a \\ (1 - 2a\tau + a^2\tau^2)e^{2a\tau} & \alpha = -a \\ e^{2a\tau} & \alpha \gg -a \end{cases} \quad (\text{A.18})$$

The biggest difference occurs at  $\alpha \ll -a$  case. This tells us that if forcing were red in comparison with the response time scale of system, then a model based on white noise assumption will lose most of its predictability. Fig. 36 shows the performance of various predictions defined above.

Finally, a mean measure of the prediction of  $x$  and  $\eta$  may be defined in term of the variance

$$\gamma(\tau) = \frac{\text{tr}\{\mathbf{C}_\tau\}}{\text{tr}\{\mathbf{C}\}}, \quad (\text{A.19})$$

which is exactly what has been used in this thesis. However, it is not of great interest here.



## APPENDIX B

## ABBREVIATIONS USED IN THIS DISSERTATION

1D	one-dimensional	NEV	normalized error variance
2D	two-dimensional	NSV	normalized signal variance
AGCM	atmosphere GCM	NTA	north tropical Atlantic
AO	Arctic Oscillation	OGCM	ocean GCM
AR	autoregressive	PC	principal component
BT	balanced truncation	PDO	Pacific decadal oscillation
CCM3	Community Climate Model version 3	PIP	principal interaction pattern
CGCM	coupled GCM	PNA	Pacific North American
COADS	Comprehensive Ocean-Atmosphere Data Set	POP	principal oscillation pattern
ENSO	El Niño–Southern Oscillation	PP	predictive power
EOF	empirical orthogonal function	PPL	predictive power loss
FOM	full order model	PrCA	predictable component analysis
GB	gigabyte	RHS	right hand side
GCM	general circulation model	ROM	reduced order model
G.M.	geometric mean	SNR	signal-to-noise ratio
H.M.	harmonic mean	SO	stochastic optimal
ICM	intermediate coupled model	SSP	stability+SO+PrC
ITCZ	intertropical convergence zone	SST	sea surface temperature
LIM	linear inverse modeling	STA	south tropical Atlantic
LTI	linear time-invariant	SV	singular vector
MPP	most predictable pattern	SVD	singular value decomposition
MXL	mixed layer	TAV	tropical Atlantic variability
NAO	North Atlantic Oscillation	WES	wind-evaporation-SST
NCAR	National Center for Atmospheric Research	w.r.t.	with respect to

## VITA

Faming Wang was born in Weifang, China on October 25, 1972 to Tingfang Liu and Jingwu Wang. He received his B.S. degree in physics from Shandong University in 1994, and his M.S. degree in remote sensing from the First Institute of Oceanography in 1997. After one year of work on seawater optics and ocean color remote sensing, he went to Texas A&M University to pursue his Ph.D. degree in oceanography, with a special interest in climatology. He received his Ph.D. in August, 2003.

Permanent Address: Zaolin, Kaiyuan, Hanting, Weifang, China, 261105.

The typist for this thesis was Faming Wang.